AN EXPERIMENTAL STUDY OF THE EFFECT OF PRESSURE ON THE FORMATION OF CHROMITE DEPOSITS

by

Natashia A. Drage

Submitted in partial fulfilment of the requirements
for the degree of Master of Science

at

Dalhousie University
Halifax, Nova Scotia
June 2022

TABLE OF CONTENTS

LIST OF TABLES

LIST OF FIGURES

ABSTRACT

Despite extensive research on the Bushveld Complex chromitites, the mechanism(s) that form such anomalous chromite segregations remains uncertain. Recent work applying the MELTS thermodynamic model proposed that reduction of pressure upon magma ascent shifts silicate-in temperatures to lower values, such that chromite is the sole liquidus phase, resulting in formation of massive chromitites in the Bushveld. This project evaluates this hypothesis by determining the effect of pressure on chromite crystallization through laboratory phase equilibrium experiments done at 0.1 MPa, 0.5 GPa, and 1 GPa, employing two bulk compositions. The first corresponds to the widely accepted parental magma of Bushveld chromitites, termed B1, and the second is the same used in the MELTS modelling study, which contrasts with B1 most significantly in Al_2O_3 (17.4 wt% vs 11.8 wt% in B1), MgO (6.7 wt% vs 11.9 wt% in B1), and Cr (~680 µg/g vs ~1000 µg/g in B1) contents. Experiments were done by equilibrating compositions at 0.1 MPa in a gas mixing furnace from 1170-1300°C and at 0.5 GPa and 1 GPa in a piston-cylinder from 1230-1530°C, with fO_2 corresponding to the fayalite-magnetite-quartz buffer and graphite-carbon dioxide buffer. Results show that the B1 magma reproduces phase equilibria and mineral compositions observed in the Bushveld whereas mineral compositions produced by the melt composition used in the MELTS modelling study are too Al-rich, excluding it as possible parental magma. Results show no significant change in Cr content of the melt at chromite saturation with pressure at constant relative fO_2 and that orthopyroxene-in temperatures decrease with falling pressure. Therefore, a low-pressure interval of chromite-alone crystallization is plausible. However, results show that significant volumes of unusually Cr-enriched B1 magma would be required to produce the chromitites observed in the Bushveld by the pressure reduction mechanism.

LIST OF ABBREVIATIONS AND SYMBOLS USED

a - Activity
γ - Activity coefficient
BSE - Backscatter electron images
BVC - Bushveld Complex
CCCS - Chromium content at chromite saturation
CCO - Graphite-carbon dioxide buffer
cpx - Clinopyroxene
chr - Chromite
CZ - Critical Zone
D - Distribution Constant
EPMA - Electron probe micro-analyzer
FeO_T - All Fe expressed as FeO
FMQ - Fayalite-magnetite-quartz buffer
fO_2 - Oxygen fugacity
ΔG^o - Change in standard state Gibbs free energy
Ga - Giga-annum
GPa - Gigapascal
IW - Iron-wustite buffer
K - Kelvin
K_D - Distribution coefficient
K_{eq} - Equilibrium constant
LA-ICP-MS - Laser ablation inductively coupled plasma mass spectrometry
LCZ - Lower Critical Zone
LG - Lower Group chromitites
liq - Liquid
LZ - Lower Zone
MG - Middle Group chromitites
MPa - Megapascal
MZ - Main Zone
NNO - Nickel-nickel oxide buffer
opx - Orthopyroxene
pl - Plagioclase
px - Pyroxene
R - Gas constant
T - Temperature
UCZ - Upper Critical Zone
UG - Upper Group chromitites
UZ - Upper Zone
wt % - Weight percent
WM - Wustite-magnetite buffer
X - Mole fraction

ACKNOWLEDGMENTS

I am grateful for the opportunity to have worked on this project under the supervision of Dr. James Brenan. I thank James for always making time for my endless questions and for his continued guidance and support. I would also like to thank the other members of my supervisory committee, Dr. Yana Fedortchouk and Dr. Djordje Grujic for their guidance and advice throughout this project. I thank Dan MacDonald for his help on the EPMA and Erin Keltie for her help on the ICP-MS.

I acknowledge funding for this research provided by a Geological Society of America Research Grant, the Society of Economic Geologists Graduate Student Fellowship program, the NSERC program, the Nova Scotia Graduate Scholarship program, and the Killam Predoctoral Scholarship program.

Finally, I would like to thank my family and friends for helping me navigate grad school during a pandemic and my lovely little pup, Rufus, for keeping my feet warm while I wrote this thesis. I am grateful for the support from my fellow lab members: Pēteris, Kathleen, Kate, and finally Bryan - who I owe a special thank you for answering the phone at (almost) any time of day and helping me handle the quirks of the piston-cylinder.

CHAPTER 1: INTRODUCTION

1.1 Chromite

1.1.1 The Mineral

Chromite belongs to the spinel-group of oxide minerals. The spinel mineral structure can be "normal", AB_2O_4, or "inverse", $B(AB)O_4$, in which A is occupied by a divalent cation, Fe^{2+} or Mg^{2+}, and B is occupied by a trivalent cation, Al^{3+}, Cr^{3+}, Fe^{3+} or Ti^{4+}. Chromite is defined as the Cr-bearing compositions in the spinel series, consisting of end members magnesiochromite ($MgCr_2O_4$) and ferrochromite ($FeCr_2O_4$), which exhibit a complete solid solution (Stevens 1944; Haggerty 1976).

1.1.2 Applications

Chromite is the only Cr-bearing ore mineral. The stainless-steel industry is the dominant consumer of Cr because it is an essential component of stainless steel with no available substitute (Schulte *et al*. 2012). As a result, Cr has been listed in the United States and Canada as one of the 35 most strategic and critical materials for which secure and reliable supplies are needed (USGS 2019; NRCan 2019). Many chromite deposits also contain platinum group elements which are used in industrial, medical, and electronic applications, significantly increasing the economic value of the deposit (Schulte *et al.* 2012). Currently, 95% of the world's Cr resources are located in South Africa, India and Kazakhstan (USGS 2019). In 2007, a significant economic chromite deposit was found within the Ring of Fire Intrusive Suite beneath the James Bay Lowlands of Northern Ontario (Brenan *et al.* 2022). With this deposit, Canada has the potential to become one of the five leading Cr producers in the world (NRCan 2019).

1.1.3 Deposit Types

Chromite is typically an accessory mineral (<1 volume %) disseminated in mantle-derived mafic and ultramafic rocks (Barnes 1998). However, occasionally chromite forms massive chromitites (up to 90 vol% chromite) as either layers in layered igneous intrusions, called stratiform deposits, or as pods in ophiolites, called podiform deposits (Stowe 1994; Barnes 1998).

Stratiform chromite deposits, whose origin is a focus of this study, consist of cyclic chromitite layers that appear to extend laterally through an intrusion and range in thickness from less than a centimetre to a few metres (Stowe 1994). The genetic model for most layered igneous bodies is that the igneous "stratigraphy" formed in a magma chamber by successive emplacement of a few to multiple pulses of melt, crystallizing one on top of the other via fractional crystallization. In this view, crystals form layers by settling or *in situ* crystallization on the chamber floor (Wager and Brown 1968; Latypov et al. 2022). An alternative hypothesis is that crystals are mechanically sorted into layers. Sorting could occur from slumping of semi-consolidated cumulates in the chamber; or, during flow of crystal slurries that were injected from a deeper reservoir, potentially from a trans-crustal, interconnected mush-dominated system (Maier *et al*. 2013; Magee *et al*. 2018; Robb and Mungall 2020; Yao *et al*. 2021). Mungall *et al.* (2016) used high-precision radiometric dating of zircon and baddeleyite to show that mafic and ultramafic layers in the South African Bushveld stratiform chromite deposit were not in stratigraphic sequence, suggesting that layers result from emplacement of successive sills. However, conflicting radiometric dates from Zeh *et al.* (2015) show in-sequence crystallization consistent with the classic model of fractional crystallization within a magma chamber. Additionally, Latypov and Chistyakova (2022) argued that out-of-sequence crystallization

is at odds with field observations and the systematic chemical trends observed in the Bushveld. In summary, the origin of igneous layering remains an open and complex question, as some of these ideas do not require mutually exclusivity (for an in-depth review see Smith and Maier 2021).

Complicating the issue, chromite-alone crystallization is not thought to be possible for typical primary melt compositions (Barnes 1998). A normal crystallization sequence from mantle-derived mafic or ultramafic melt is first, olivine or orthopyroxene, followed by olivine or orthopyroxene co-crystallizing with chromite (Barnes 1998; Barnes 1986a). Therefore, despite decades of research, the mechanism(s) that form these anomalous chromite segregations is uncertain (Latypov *et al.* 2018). Hypotheses fall into two general categories: (1) either chromite is physically separated from cotectic minerals through gravitational settling or mechanical sorting (Kruger 2005; Eales 2000), or (2) a change in the system occurs causing suppression of silicate phase(s) and therefore, chromite-alone saturation in the melt. Frequently cited hypotheses for this mechanism include magma contamination or mixing, change in oxygen fugacity (fO_2), addition of fluids, and change in pressure, which is the focus of this study (Irvine 1975; Cameron and Desborough 1969; Nicholson and Mathez 1991; Lipin 1993; Latypov *et al*. 2018). An overview of these hypotheses can be found in Section 1.3. For a more complete review see Maier *et al.* (2013), Cawthorn (2015), Latypov *et al*. (2017), and Smith and Maier (2021).

1.2 The Bushveld Complex: A Stratiform Chromite Deposit

1.2.1 Geology

The South African Bushveld Complex (Figure 1.1) is the world's largest layered igneous intrusion and is host to stratiform chromitites. It contains much of the world's Cr,

platinum group elements, and V resources (Naldrett *et al*. 2009; Zientek *et al*. 2014). The Complex, which has an estimated area of 65 000 km^2 (Eales and Cawthorn 1996), intruded the Transvaal Supergroup sediments and the Archean Kaapvaal Craton around 2.05-2.06 Ga (Walraven *et al.* 1990; Kruger 2005) at shallow crustal levels. Andalusite-bearing metapelitic rocks in the aureole beneath the Complex indicate that it intruded at <0.3 ± 0.05 GPa (Waters and Lovegrove 2002) and potentially as low as 0.06 GPa based on estimates from calcsilicate assemblages in marginal rocks (Wallmach *et al*. 1989). The source of magmatism for this large igneous province is debated. The enormous volume suggests magmatism was plume-driven (Hatton 1995), originating in the lithosphere or asthenosphere, with sutures in the Archean craton acting as a magma pathways through the crust (Smith and Maier 2021 and references therein). Alternate hypotheses suggest plate-driven magmatism such as back-arc rifting (Clarke *et al*. 2009), delamination of the subcontinental lithospheric mantle (Olsson *et al*. 2011), or post-collisional rifting (Silver *et al*. 2004).

The Bushveld Complex, now exposed as multiple lobes (Figure 1.1), consists of: (1) an early stage of mafic sills, (2) felsites of the Rooiberg volcanic group which form the roof of (3) the layered mafic and ultramafic suite called the Rustenburg Layered Suite, and (4) a granophyre and granite suite (Naldrett *et al*. 2012 and references therein). The Rustenburg Layered Suite, commonly described as a flat saucer, is ~ 7-9 km thick and ~ 400 km wide (Von Gruenewaldt *et al*. 1985; Eales and Cawthorn 1996) and formed over a ~0.6-1 Myr period (Zeh *et al*. 2015; Mungall *et al*. 2016). The Rustenburg Layered Suite is divided into five major zones (Figure 1.1): (1) the Marginal Zone, consisting of fine-grained norites that are adjacent to, and emplaced as sills in the local country rock, (2) the Lower Zone (LZ), consisting of dunite, harzburgite, and pyroxenite layers, (3) the

Critical Zone (CZ), consisting of pyroxenite, norite, and anorthosite layers as well as 14 major chromitite horizons (Naldrett *et al*. 2012 and references therein), (4) the Main Zone (MZ), consisting of gabbronorites, and (5) the Upper Zone (UZ), consisting of gabbronorites with magnetite layers (Kruger 2005). The CZ, a focus of this study, is subdivided into the Lower Critical Zone (LCZ) which is dominantly orthopyroxenite with minor olivine-rich layers and the Upper Critical Zone (UCZ) which in addition to orthopyroxenite contains norites and anorthosite layers. The transition between the two is marked by the introduction of cumulus plagioclase (Cawthorn 2015).

1.2.2 Bushveld Chromitites

Chromite layers in the CZ range from ~ 1 dm to 2 m (Maier *et al*. 2013) and are hosted within pyroxenites and anorthosites, in contrast to chromitites in many other layered intrusions which are hosted in olivine-rich layers. The CZ chromitites are divided into three groups: the Lower Group, Middle Group and Upper Group (Figure 1.1) which can be correlated laterally across the Complex, although thickness varies (Cawthorn 2015). Chromite compositions in these layers follow two distinct trends: (1) increasing Cr# [Cr/(Cr+Al)] and increasing Fe# [Fe^{2+}/(Fe^{2+}+Mg)] in response to plagioclase and orthopyroxene fractionation (trend A; Naldrett *et al*. 2009); or, (2) decreasing Cr# and increasing Fe# in response to orthopyroxene fractionation (trend B; Naldrett *et al*. 2009).

Mass balance of Cr in the CZ is enigmatic. Eales (2000) calculated that an ~15 km magma column with ~1000 μg/g Cr, like B1 (see below), would be required to account for the total Cr content incorporated in chromite and pyroxene in the CZ. This volume of magma is not observed in the Bushveld Complex. However, if the Complex represents an open system, the residual magma may have escaped from the chamber vertically or

laterally and solidification products could have been eroded (Cawthorn and Walraven 1998; Cawthorn 2015; Latypov *et al*. 2022). Eales and Costin (2012) suggested that residual magma remained below in a deep-seated chamber (Cole *et al*. 2021) from which a magma with suspended chromite crystals was injected into the shallow level, CZ-forming chamber.

1.2.3 Critical Zone Parent Magmas

Fine-grained rocks and sills at the margins of the complex, characterized by Davies *et al*. (1980), Sharpe (1981), Curl (2001), and Barnes *et al*. (2010), have been proposed as parental magmas to the Rustenburg Layered Suite (Figure 1.1). The compositions identified consist of a siliceous high-Mg basalt, termed B1, and tholeiitic basalts, termed B2 and B3 (Figure 1.2). These magmas are thought to have formed from komatiite mantle melts contaminated with crustal material upon ascent, from melting of metasomatized subcontinental lithospheric mantle, or a combination of the two (Barnes *et al*. 2010 and references therein; Wilson 2012; Maier *et al*. 2013; Maier *et al.* 2016). The B1 composition, with ~ 56 wt % SiO_2, ~ 11.85 MgO wt % (up to 14.5 wt %), ~ 1000 µg/g Cr (up to 1400 µg/g; Maier *et al*. 2013 and references therein; Harmer and Shape 1985), and low water contents (up to ~1 wt%; Boudreau 2002; Mungall 2015; Cawthorn 2015), is thought to be the parent to the LZ and LCZ. This is based on stratigraphic position, whole rock geochemistry, major and trace element chemistry of cumulus and intercumulus minerals in both the LZ and LCZ, thermodynamic modelling and experimental phase equilibrium studies (Davies *et al*. 1980; Godel *et al*. 2011; Barnes *et al*. 2010; Cawthorn and Davies 1983).

A more primitive parental composition has also been proposed for the LZ and LCZ (Wilson 2012; Eales and Costin 2012). Eales and Costin (2012) questioned whether B1, given the high SiO_2 content, would produce the amount of olivine observed in olivine-bearing rocks (harzburgites) of LZ. As a result, a komatiitic parent was suggested in which B1 sills could represent residual magmas, rather than the parent (Yao *et al*. 2021). A komatiitic parent could potentially resolve the Cr mass balance issue because these hotter and more Mg-rich compositions can dissolve more Cr (Murck and Campbell 1986; Barnes 1998; Eales and Costin 2012). At present, a Mg-rich basaltic andesite (15.2 wt% MgO) and komatiite (18.7 wt% MgO) have been identified in chill margins at the base of the LZ (Maier *et al.* 2016) but these compositions do not contain significantly more Cr (1205 µg/g and 1515 µg/g, respectively).

The parent to the UCZ is not as clear. The crystallization sequence can be modelled by B1 and not B2; however, isotopic variations (particularly an increase in initial Sr ratio; Kruger 1994) cannot be reproduced by B1 alone, leading to the suggestion of a magma mix, potentially of B1 and B2 (60:40; Barnes *et al*. 2010).

1.2.4 Oxygen Fugacity Estimates

Estimates for the fO_2 of the Bushveld magmas are consistently near the fayalite-magnetite-quartz buffer (FMQ). Langa *et al.* (2021) investigated $Fe^{3+}/(Fe^{3+}+Fe^{2+})$ ratios of chromite in UCZ chromitites (UG-2) which record an fO_2 of FMQ-1 to FMQ. Barnes *et al*. (2022) employed the V in chromite and melt oxybarometer calibrated by Canil (2002) to estimate fO_2 for UCZ chromitites (UG-2) and found fO_2 to range from FMQ-2 to FMQ-1. In the UZ, ilmenite-magnetite pairs record an fO_2 of FMQ-1 (VanTongeren and Mathez 2012; Bilenker *et al*. 2017). Additionally, the high vanadium concentrations

of magnetite in the UZ constrain fO_2 between ~FMQ and FMQ+1 based on magnetite-melt partitioning experiments by Toplis and Corgne (2002).

1.3 Models for the Bushveld Chromitites

1.3.1 Gravitational Settling

The high density of chromite has led researchers to propose that, in a magma chamber, chromite crystallizes in cotectic proportions with olivine or orthopyroxene but settles first, forming a layer at the bottom of the chamber (Wager and Brown 1968). This process would leave behind a large volume of Cr-depleted magma resulting in a decrease in the Cr/Al ratio of overlying pyroxene (Latypov *et al.* 2017). However, this is not observed in the Bushveld Complex (Mondal and Mathez 2007). Furthermore, this hypothesis does not explain the consistently sharp contacts between chromitites and cumulate rocks (Cawthorn 2015). Gravitational settling would also result in an in-sequence stratigraphy, contrary to the out-of-sequence radiometric dates for the Rustenburg Layered Suite reported by Mungall *et al.* (2016).

1.3.2 Mechanical Sorting

Eales (2000) proposed a model where a magma, separate from the main chamber, crystallizes chromite and orthopyroxene in cotectic proportions and is injected into the main chamber as a crystal slurry. Chromite and orthopyroxene are subsequently mechanically sorted during flow, concentrating chromite, and forming a layer. In this model, the remaining volume of magma escaped vertically as lava flows (Cawthorn and Walraven 1998), laterally as sills (Mungall *et al.* 2016) or remained below, in a deep-seated chamber (Naldrett *et al.* 2012). Mondal and Mathez (2007) supported this

hypothesis by showing that, in the Bushveld Complex, chromite and orthopyroxene in chromitites are texturally and compositionally the same as those in silicate cumulates, suggesting that these minerals crystallized together.

Maier *et al*. (2013) hypothesized that crystal slurries slumped towards the center of the subsiding Rustenburg Layer Suite causing modal layering by kinetic sieving and hydrodynamic sorting. Forien *et al.* (2015) confirmed this by conducting flume tank experiments which showed that slumping of semi-consolidated crystals results in sorting that gives rise to single-phase layering.

1.3.3 Addition of Water

Nicholson and Mathez (1991) suggested that fluids migrating through a magma chamber will initiate melting of cumulate orthopyroxene. Chromium is readily incorporated into orthopyroxene, so melting this mineral will release Cr into the melt. Furthermore, the newly hydrated Cr-rich melt will favour chromite crystallization over other possible phases (Ford *et al.* 1972), causing chromitites to form (Nicholson and Mathez 1991). Recently, experiments by Veksler and Hou (2020) investigated the effect of H_2O on chromite saturation in a B1 composition at 0.3 GPa. The authors found that increasing H_2O contents resulted in no significant change in the Cr content of the melt at chromite saturation (CCCS) but did suppress the crystallization of silicate minerals, causing chromite-alone crystallization. However, it is important to note that fO_2 was not buffered in those experiments, which is known to strongly affect the CCCS (Murck and Campbell 1986; Roeder and Reynolds 1991). Hydrous phases such as phlogopite are indeed observed in the Bushveld suggesting the presence of volatiles (Boudreau 1992). However, Mondal and Mathez (2007) noted that to produce a chromitite, dissolution of

almost 100 times its mass in orthopyroxene would be required, which those authors consider to be geologically unreasonable.

1.3.4 Magma Mixing and Contamination

Contaminating a magma with silica and alkalis can, in theory, produce a chromite-alone saturated melt in the olivine-chromite-silica system. Irvine (1975) suggested that magmas emplaced into felsic country rocks will induce melting and produce a silica and alkali rich melt, providing the appropriate contaminants to crystallize a chromitite layer. However, Irvine (1977) experimentally determined that the addition of alkalis would shift the phase boundaries such that the amount of contamination required to crystallize the volume of chromitite in the Bushveld Complex would be geologically unreasonable.

Alternatively, mixing a primitive melt with an evolved melt can theoretically produce a chromite-alone saturated melt in the olivine-chromite-silica system (Irvine 1975). The system that Irvine (1975) considered, however, lacked Fe, an essential component of chromite, which would likely affect the phase relationships. This mechanism would also suggest that resulting lithologies would shift from more evolved to more primitive. Chemical indicators of evolution, such as Mg/Fe ratios, measured in layers above and below Bushveld chromitites, do not record this expected change (Mondal and Mathez 2007).

1.3.5 Change in fO_2

Cameron and Desborough (1969) hypothesized that a sudden increase fO_2 could cause chromite-alone saturation. This is consistent with experimental studies which show that increasing fO_2 causes the CCCS to decrease, initiating chromite saturation (Murck and

Campbell 1986, Roeder and Reynolds 1991). An increase in fO_2 is possible if a high-fO_2 melt is injected into the magma chamber, similar to the magma mixing hypothesis by Irvine (1977). However, there is no other evidence demonstrating a change in fO_2 in the Bushveld Complex (Mondal and Mathez 2007).

1.3.6 *Change in Pressure*

Lipin (1993) examined existing experimental data showing that the spinel-alone stability field expands with increasing pressure and applied this to chromite crystallization. Lipin (1993) suggested that if a magma body experienced an increase in pressure, the system could fall into the expanded chromite-alone field and crystallize chromite until the pressure dissipates. Possible mechanisms to cause a pressure increase include injection of a CO_2-rich magma, adding a new volume of magma to the chamber, or tectonism causing a change to the shape of the chamber (Lipin 1993; Cameron 1977). However, the experimental data used in the hypothesis described in Lipin (1993) are from Cr- and Fe-free experiments (Sen and Presnall 1984). Since these are essential constituents of the mineral chromite, these experiments are not relevant to chromite crystallization. Additionally, chromite crystallization experiments by Roeder and Reynolds (1991) showed the opposite result, in which the CCCS increases slightly with rising pressure, causing chromite to dissolve.

More recently, Latypov *et al*. (2018) applied the MELTS thermodynamic model to propose that reduction of pressure upon magma ascent shifts the silicate-in temperature to lower values, such that chromite is the sole liquidus phase, resulting in chromite-alone crystallization (Figure 1.3). In this model, magma ascends crystal-free, superheated by at least 10ºC, eroding basal cumulates upon reaching the shallow chamber and creating the

irregular contacts observed in the Bushveld (i.e., potholes and anti-potholes). As the magma cools, chromite-alone crystallizes *in situ* and is later joined by orthopyroxene and plagioclase. To produce a metre-thick chromite layer, a magma column several kilometres thick is required, in which the residual melt flows out of the system.

Latypov *et al*. (2018) initially modelled crystallization of the B2 composition, a proposed parental magma for the UCZ in the Bushveld Complex, at FMQ, from 0.1 to 1 GPa. However, the resultant crystallization sequences do not reproduce the observed mineral chemistry or field observations. To address this, Latypov *et al.* (2018) incrementally altered the B2 composition to produce a crystallization sequence that reflected field observations, and which demonstrated a pressure interval of chromite-alone saturation (Figure 1.3b). This modified B2 composition is compared to those observed in the Bushveld in Figure 1.2. The alkali content of the modified composition is consistent with a tholeiitic composition (Figure 1.2a) whereas the Al_2O_3 content is consistent with a calc-alkaline composition. The high Al_2O_3 content contrasts with the other Bushveld compositions which fall in the tholeiitic and basaltic komatiite fields in Figure 1.2b. This is an important distinction because Al_2O_3 is an important component of chromite and therefore, added Al_2O_3 could enhance the stability field of this mineral compared to more Al_2O_3-poor tholeiitic compositions. However, Latypov *et al*. (2018) do not comment on this, apparently accepting this composition as a preferred parent magma for the UCZ.

The MELTS family software has been shown to reproduce experiments involving spinel poorly and overestimate spinel saturation temperatures by 25-250ºC (Nikolaev *et al.* 2018). Additionally, MELTS does not include Cr in the model for pyroxenes and consequently, by including a Cr_2O_3 component in the melt, MELTS will overestimate the

stability of chromite (Asimow *et al*. 1995). Therefore, it is unclear whether MELTS can accurately model chromite and chromite-alone crystallization.

There are no experimental data available that directly test the effect of pressure on chromite crystallization over the conditions proposed by Latypov *et al.* (2018). As a result, the authors rely on spinel and chromite experimental data from a primitive arc basalt composition which were buffered at significantly higher fO_2 (~FMQ+4.5 to FMQ+6; Stamper *et al.* 2014) than relevant to the Bushveld. The high fO_2 conditions of these experiments would likely overestimate the chromite stability range and their application to the Bushveld should be considered with caution.

1.4 Previous Experimental Work

1.4.1 Phase Equilibrium Experiments

Phase equilibrium studies investigating different estimates of the B1 composition at atmospheric pressure (0.1 MPa) include: Sharpe and Irvine (1983), Barnes (1986a), Cawthorn and Biggar (1993). At FMQ, these studies found olivine to be the silicate liquidus mineral (with olivine-in temperatures ranging from 1275-1300ºC), followed by orthopyroxene (with orthopyroxene-in temperatures ranging from 1210-1270ºC). Some chromite compositional data are provided by Cawthorn and Biggar (1993) but are otherwise limited in these investigations.

Cawthorn and Davies (1983) conducted phase equilibrium experiments using natural samples from Bushveld Complex, of these, 'composition 4' is similar in composition to B1. Experiments were unbuffered with respect to fO_2 and done at 0.15 GPa, 0.3 GPa and 1 GPa. At 0.15 GPa and 0.3 GPa, olivine was the liquidus phase, followed by orthopyroxene. At 1 GPa, olivine was replaced by orthopyroxene on the liquidus. Spinel

was identified in these experiments but neither the Cr content of spinel nor the initial Cr content of the melt are reported in this contribution.

1.4.2 CCCS Experiments

Experimental studies have shown that the CCCS is affected by temperature, fO_2, and melt composition, specifically, Fe, H_2O, and alkali content (Murck and Campbell 1986; Roeder and Reynolds 1991; Mungall and Brenan 2014; Sisson and Grove 1993; Veksler and Hou 2020). Murck and Campbell (1986) investigated the CCCS in experiments done at 0.1 MPa and 1150ºC to 1500ºC on basaltic ('401' basalt) and komatiitic compositions along the FMQ, NNO (nickel-nickel oxide) and IW (iron-wustite) buffers. Roeder and Reynolds (1991) also conducted experiments at 0.1 MPa and 1200ºC to 1400ºC on the '401' basalt over a wide range of log fO_2 values (~ FMQ-5.5 to FMQ+4.5). Barnes (1986a) conducted experiments at 0.1 MPa and 1151ºC to 1334ºC along the FMQ, NNO, IW and WM (wustite-magnetite) buffers using a B1 composition that was mixed with 30% powdered natural orthopyroxene from the Stillwater Complex (Montana, USA). Collectively these studies showed that the CCCS decreases with decreasing fO_2 and falling temperature (Figure 1.4). Decreasing fO_2 results in an increase in the CCCS which is associated with the reduction of Cr^{3+} to Cr^{2+} in the melt. The proportion of Cr^{2+} is the greatest at reducing conditions and diminishes as FMQ is approached (Figure 1.4) and Cr^{3+} becomes predominant (Roeder and Reynolds 1991).

Experiments at 0.1 MPa investigating compositional effects on the CCCS found that increasing alkalis and FeO content of the melt both decrease the CCCS (Murck and Campbell 1986; Mungall and Brenan 2014). As previously mentioned, recent experiments by Veksler and Hou (2020) were conducted at 0.3 GPa, from 1100ºC to 1300ºC, using a

B1 composition and H_2O contents from 0 wt% to 6 wt%. The authors found that changes in H_2O contents did not affect the CCCS, which is consistent with results of magnetite solubility experiments by Sisson and Grove (1993). However, as previously noted, the fO_2 in experiments of Veksler and Hou (2020) was unbuffered.

There has been little work done to show the effect of pressure on chromite crystallization. Sen and Presnall (1984) conducted experiments at 1 GPa involving compositions in the $CaAl_2Si_2O_8$ (anorthite) – Mg_2SiO_4 (forsterite) – SiO_2 (quartz) system and showed that spinel and orthopyroxene stability expands at the expense of olivine with increasing pressure. However, this is a simplified system that does not include the essential components of chromite (i.e., Fe and Cr). This result also conflicts with the experiments of Roeder and Reynolds (1991), who described a slight increase in CCCS with pressure at a constant log fO_2 value and 1300 ºC, from ~1390 µg/g at 0.1 MPa (log fO_2 = -8.47; ~FMQ-1) to ~1720 µg/g at 1 GPa (log fO_2 = -8.37; ~FMQ-1.7).

1.5 Objective

In this thesis, the pressure reduction hypothesis described by Latypov *et al*. (2018) is evaluated by determining the effect of pressure on the CCCS at constant fO_2 relative to the FMQ buffer in laboratory experiments. This thesis also provides phase equilibria and mineral compositional data over a range of pressure for both the composition used in the thermodynamic model by Latypov *et al*. (2018) and the widely accepted proposed parental composition to Bushveld chromitites, B1. Resultant phase equilibria and mineral compositional data are compared to natural data from the Bushveld Complex to test these compositions as viable parent liquids to the CZ chromitites.

CHAPTER 2: METHODS

Experiments were conducted to determine phase equilibrium and chromite solubility at pressures ranging from 0.1 MPa to 1 GPa. Experiments at 0.1 MPa were done using a gas mixing furnace, and a piston-cylinder apparatus was used to generate high pressure conditions for experiments done at 0.5 GPa and 1 GPa.

Oxygen fugacity is known to be the dominant control on chromite solubility. Therefore, buffering fO_2 such that pressure is an isolated variable is a requirement to test the pressure reduction hypothesis and is the most challenging aspect of these experiments. In piston-cylinder assemblies, graphite capsules are commonly used to buffer fO_2 through reactions that involve a C-O gas phase. The resulting fO_2, however, is strongly dependent on pressure (Ulmer and Luth 1991). To buffer fO_2 independently of pressure, Fe-Ir alloy capsules were used (Brenan *et al.* 2012) which maintain the fO_2 at a given value through the equilibrium:

$$Fe_{(alloy)} + \tfrac{1}{2}O_2 \leftrightharpoons FeO_{(melt)}. \quad (2.1)$$

Silicate phase equilibrium were investigated in more detail at high pressures using graphite-lined Pt capsules. The Fe_2O_3 in silicate minerals is negligible and therefore, variation of fO_2 and therefore, Fe_2O_3 content in the melt does not affect their crystallization temperature.

Melt compositions explored in this study include (1) a proposed parental magma composition to the LZ and LCZ of the Bushveld Complex, termed B1, as outlined by Barnes *et al.* (2010) and (2) the composition used to construct the thermodynamic model used in Latypov *et al*. (2018) to support the pressure reduction hypothesis (referred to as Lat hereafter).

2.1 Experimental Methods

2.1.1 *Starting Materials*

The B1 and Lat starting materials were prepared by mixing reagent grade oxides and carbonates which were ground twice under ethanol in an agate mortar. Starting materials were placed in Pt crucibles and calcined in air, at 600°C, in a box furnace for 12 h. Compositions were ground under ethanol again and fused into a glass by melting the material in a Pt crucible for 30 min in air, in a box furnace, at 1500°C, then rapidly quenching in water. Glasses were then ground under ethanol into a fine powder and fused for a second time to ensure homogeneity. Final starting materials were stored in a drying oven at 110°C.

The compositions of the resultant glasses, B1_SM_3 and Lat_SM_3 which contain 859 µg/g and 681 µg/g Cr, respectively, are presented in Table 2.1. The average relative difference in major element composition for B1_SM_3 and values reported for B1 by Barnes *et al*. (2010) is 0.85 wt%. The average relative difference in major element composition for Lat_SM_3 and values reported for Lat by Latypov *et al*. (2018) is 0.61 wt%. Brucite ($Mg(OH)_2$) was added to starting materials which decomposes at run conditions to yield water. The resultant water contents are 0.31 wt% and 0.45 wt% in B1_SM_3 and Lat_SM_3, respectively.

Some experiments failed to crystallize chromite, therefore, additional Cr was added to two batches of B1_SM_3 and Lat_SM_3 to ensure chromite saturation (referred to as the chromite-doped starting material hereafter). To do this, starting materials were doped with synthetic stoichiometric chromite ($FeCr_2O_4$) powder. The resultant total Cr content for the first chromite-doped batch is ~ 4650 µg/g and ~ 4510 µg/g, in B1 and Lat

respectively, and for the second batch is ~ 4440 μg/g and ~ 4100 μg/g, in B1 and Lat respectively.

2.1.2 Gas Mixing Furnace Experiments

Experiments done at 0.1 MPa were conducted in a vertical-tube gas mixing furnace in the Dalhousie Experimental Geochemistry Laboratory. High temperature conditions were generated by six $MoSi_2$ heating elements surrounding the furnace tube. A Type S (Pt-$PtRh_{10}$) thermocouple, calibrated against the melting point of Au, was used to measure temperature inside the furnace. Mass flow controllers regulated the flow of oxidizing (CO_2) and reducing (CO) gases to control the fO_2. Before and after each experiment, fO_2 was measured using a Y-doped zirconia sensor. The sensor generates an electrical potential in response to the differing oxygen concentrations in the furnace and the reference gas (air). The fO_2 was then calculated from the measured electrical potential using the Nernst Equation. The accuracy of the Y-doped zirconia sensor was checked using the (Ni,Mn)O sliding redox sensor method of Taylor *et al*. (1992) and found to be within 0.07 log units of the fO_2 measured by the Y-doped zirconia sensor. Details of the thermodynamic basis and experimental method for the (Ni,Mn)O sliding redox sensor are provided in Appendix A.

Approximately 56 mg of starting material was mixed with polyvinyl alcohol and mounted on a pre-saturated Fe-Ir wire loop. Loops were pre-saturated with Fe to prevent Fe loss from the sample to the Ir wire. To pre-saturate the wire, an aliquot of starting material was melted on the initially pure Ir wire loop at the same conditions as the final experiment. After the pre-saturation step, the glass was dissolved using HF and the wire

was loaded with new starting material for the experiment. Pre-saturated wire loops with B1 and Lat starting material were suspended on a hook fashioned at the end of a high purity silica rod (Figure 2.1a). Experiments were executed by first withdrawing the silica rod to the top of the furnace tube, then sealing the furnace and commencing gas flow. The sample was then lowered into the predetermined hotspot and remained there for the experiment duration. Experiments were terminated by opening the bottom of the furnace and lowering the silica rod through the bottom, quenching samples in air at room temperature.

Run conditions are summarized in Table 2.1. Experiments were of two types: (1) crystallization experiments using glass starting material and (2) melting experiments using crystallized starting material.

Crystallization experiments (Series 1.0 and Series 5.0 in Table 2.1) were done at temperatures between 1170-1340°C for durations of 24-96 h, the majority of which were 48 h. The fO_2 of Series 1.0 experiments corresponds to the Fayalite-Magnetite-Quartz (FMQ) buffer (O'Neill 1987), whereas Series 5.0 were done at FMQ-0.4.

Melting experiments (Series 2.0 in Table 2.1) were done at temperatures of 1200°C and 1280°C for durations of 12-48 h, at ~FMQ. Melting experiments involved an initial crystallization step done by holding the temperature at 1200°C and ~FMQ for 1 h, then lowering the temperature at 10°C/h to 800°C while adjusting CO/CO_2 ratio to maintain the fO_2 at FMQ. Samples were held at 800°C overnight, then the temperature was increased at 90°C/h to the final experiment conditions.

2.1.3 Piston-cylinder Experiments

Experiments done at 0.5 GPa and 1 GPa were conducted using a piston-cylinder apparatus (Boyd and England 1960) in the Dalhousie Experimental Geochemistry Laboratory. Standard 12.70 mm and 19.05 mm diameter solid pressure assemblies were used, which consisted of MgO filler pieces, a graphite furnace sleeve, and either $BaCO_3$ cells for the 12.70 mm assembly or NaCl cells along with a Pyrex sleeve for the 19.05 mm assembly (Figure 2.1b). Thermal mapping experiments of both assembly types were conducted to determine the position and length of the hotspot using the spinel growth method after Watson (2002) (See Appendix B for detailed methods and results). B1 and Lat were run simultaneously in this configuration by positioning capsules in the MgO piece side by side in the predetermined hotspot.

All experiments were cold pressurized to ~0.03 GPa above the desired pressure which was then maintained manually while ramping the temperature at 50°C/min. Pressure was periodically adjusted during the run such that all piston-cylinder experiments were controlled within ± 0.015 GPa of the desired value. A friction correction of +20% was applied to experiments done at 0.5 GPa, determined using the water in albite method (Baker 2004) whereas no correction was required for experiments at 1 GPa, determined using the melting point of NaCl (Bohlen 1984) (See Appendix B for detailed methods). Heat was generated by running an electrical current through the graphite furnace and the temperature was monitored with an alumina-sheathed Type C (WRe_5-WRe_{26}) thermocouple with no pressure correction applied to the emf. To terminate the experiment, the power to the furnace was cut, resulting in a drop to < 300°C in seconds.

Experiments were of two types: (1) Silicate phase equilibrium experiments done using graphite-lined Pt capsules (Series 4.0 in Table 2.1) and (2) CCCS and phase equilibrium experiments done using Fe-Ir capsules (Series 3.0 in Table 2.1).

Graphite liners were fabricated from high-density graphite, which was machined into 2.6 mm x 4 mm capsules with a 1 mm x 2 mm hole for the sample and a 2.6 mm x 1 mm plug-shaped lid. Capsules were cleaned ultrasonically in acetone, then dried for at least 1 h at 200°C, in a box furnace and stored in a drying oven at 110°C. Approximately 2 mg of fully oxidized glass starting material was packed tightly into the graphite capsule which was then inserted into a 3 mm diameter Pt capsule, dried at 110°C for at least 2 h, then welded shut. Welds were tested by submerging the finished capsule in acetone for ~15 minutes. A capsule with the same weight, before and after, indicated a successful weld. Experiments were done using 19.05 mm assemblies, except for run temperatures at and above 1500°C, which were done using 12.70 mm assemblies.

Iron-Ir capsule compositions were calculated based on the equilibrium of FeO in the melt and an fO_2 (Equation 2.1) corresponding to FMQ (O'Neill 1987) at experimental pressure and temperature conditions using thermodynamic data from Holland and Powell (1990) for the pressure term. For the thermodynamic basis of Fe-Ir capsules, see Appendix C. Capsules and lids were fabricated by mixing Fe and Ir metal powders which were pressed in a mold within a thick-walled fused silica tube (ID = 3 mm, OD = 8 mm) and then sintered in a gas mixing furnace overnight at 1400°C and an fO_2 corresponding to FMQ. For samples contained in Fe-Ir capsules, glass starting materials were pre-reduced in the gas mixing furnace to achieve the ~ Fe^{2+}/Fe^{3+} ratio corresponding to the FMQ buffer at experimental conditions. Approximately 1 mg of this pre-reduced starting material was packed tightly into the ~ 1 mm x 1.5 mm hole of the ~ 2.6 mm x 3 mm Fe-Ir

capsule and closed with a ~ 2.6 mm x 1 mm lid, that was pressure welded during the experiment. Packed capsules and solid pressure assemblies were dried at 110°C for at least 2 h prior to the experiment. Experiments using Fe-Ir capsules were done using 19.05 mm assemblies at 1230°C and 1280°C, for 12 h, at both 0.5 GPa and 1 GPa. An initial run at 1 GPa and 1280°C (Exp #: 3.2) did not crystallize chromite, therefore, all subsequent runs in Fe-Ir capsules were conducted using the chromite-doped starting material, to ensure chromite saturation.

2.2 Analytical Methods

Experimental run-products were mounted in 25 mm diameter epoxy pucks which were ground using successively finer SiC grit, then finished with 1 μm and 0.3 μm alumina powder. Phases in run-products were determined on the Electron Probe Micro-Analyzer (EPMA) in the Robert M. MacKay Electron Microprobe Laboratory at Dalhousie University using backscatter electron images and by measuring the major element composition. In effort to capture all crystallizing phases, as many measurements as possible were taken, however, phases present in small amounts could be unknowns. The Cr content of run-product glasses was measured using the Laser-Ablation Inductively Coupled Plasma Mass Spectrometer (LA-ICP-MS) located in the Health and Environments Research Centre Laboratory at Dalhousie University. In some cases, melt pockets in run-products were too small for Cr to be analyzed by the LA-ICP-MS and the EPMA was used instead with higher count times to obtain more precise measurements (Table 2.1).

2.2.1 EPMA

Sample pucks were carbon coated prior to analysis on the EPMA. Silicate glasses were analyzed using a 15 kV accelerating voltage, a 10 nA beam current and a 10 μm defocused beam. Standards for the silicate glass analyses included the basalt USGS standard reference material, BHVO-1 (Si, Ca, Al, Fe, Mg, Na), rutile (Ti), chromite (Cr), sanidine (K), pyrolusite (Mn), and apatite (P). A count time of 20 s was used for all elements except for Cr, which was 40-60 s. Two basalt USGS reference standards, BHVO-1 and BIR-1, were analyzed before and after ~ 30 unknown points to monitor the accuracy and precision of the EPMA measurements. Table D1 summarizes analyses of BHVO and BIR from all analytical sessions and shows that the measured compositions are within the uncertainty range of preferred published values (Jochum *et al.* 2016).

Chromite and silicate minerals were analyzed using a 15 kV accelerating voltage, a 20 nA beam current and a 1 μm spot size. A count time of 20 s was used for all elements. Standards for chromite analyses were chromite (Cr, Fe, Mg, Al), kaersutite (Ca), sanidine (Si), rutile (Ti), and pyrolusite (Mn). Standards for pyroxene analyses were orthopyroxene (Si, Al, Fe, Mg), albite (Na), kaersutite (Ca, Ti), chromite (Cr), sanidine (K), and pyrolusite (Mn). Standards for plagioclase analyses were plagioclase (Si, Al, Ca), albite (Na), kaersutite (Mg), garnet (Fe) sanidine (K), and pyrolusite (Mn).

The Fe-Ir alloy capsule compositions were analyzed using a 20 kV accelerating voltage, a 50 nA beam current and a 1 μm beam size. Count times were 30 s for Fe and 10 s for Ir. Standards for Fe-Ir alloy analyses were pure Fe and pure Ir metal.

Raw count rates were converted to elemental concentrations by measuring standards and using the ZAF (atomic number, absorption, fluorescence) data reduction scheme.

2.2.2 LA-ICP-MS

The LA-ICP-MS ablated samples with a 213 nm frequency quintupled Nd:YAG laser. Ablated material was transported using He carrier gas to a Thermo Scientific iCAP Q quadrupole ICP-MS. Silicate glasses were analyzed using a 10 Hz repetition rate, ~ 5 J/cm^2 fluence and 20-25 μm diameter laser beam. Analyses included 20 s of background collection, followed by 60 s of sample ablation and then 60 s of washout. The following isotopes were measured: ^{53}Cr, ^{52}Cr and ^{43}Ca. The silicate glass standard reference material, NIST-610, was measured twice at the start of every session and again after 18 unknown analyses. Additionally, two basaltic USGS reference standards, BHVO-1 and BIR-1, were measured as unknowns after every 20-40 points to monitor the accuracy and precision of the LA-ICP-MS analyses. Table D1 summarizes the results from BHVO and BIR over all analytical sessions and indicates that measured values are within the uncertainty range of preferred published values (Jochum *et al.* 2016). Data reduction was performed using versions 3.6 and 4.5 of the Iolite Software Package with NIST-610 as the external standard for Cr (408 μg/g, Jochum *et al.* 2011) and Ca as the internal reference element to correct ablation yields. The Ca values for unknowns were measured by the EPMA. The Iolite software corrects for background levels and instrumental drift, and calculates concentrations, detection limits and analytical precision. Reported Cr values in Table 2.1 represent the average concentration determined by both Cr isotopes measured, ^{53}Cr and ^{52}Cr.

CHAPTER 3: RESULTS

3.1 Attainment of Equilibrium

Several methods were employed to evaluate the approach to equilibrium in experiments. Although most experiments were done by crystallizing phases from a glass starting material, additional melting experiments were done at 0.1 MPa in the gas mixing furnace at 1200°C for 48 h and at 1280°C for 12-24 h, in which subsolidus phases were melted by heating crystallized starting material. This style of experiment is considered a reversal by approaching equilibrium from down temperature, bypassing the nucleation step. The average relative difference in composition between crystallization and melting experiments, which are summarized in Table 2.1, is 1.29 % for major elements and 11.34 % for Cr content in the glass. The CCCS for crystallization and melting experiments are plotted as a function of temperature in Figure 3.1 and show overall agreement. Therefore, 48 h was determined to be sufficient to reach equilibrium in CCCS experiments and can be approached in as little as 12 h at 1280°C.

Another method to assess equilibrium is by the partitioning of Fe-Mg between pyroxene and melt, which follows the reaction of:

$$FeO^{px} + MgO^{liq} = FeO^{liq} + MgO^{px}, \quad (3.1)$$

with a resultant distribution coefficient (K_D) of:

$$K_D\ (Fe-Mg)^{px-liq} = \frac{X_{Fe}^{px} X_{Mg}^{liq}}{X_{Mg}^{px} X_{Fe}^{liq}}, \quad (3.2)$$

in which X is the mole fraction. It has been shown that the K_D expressed in this way does not vary significantly with temperature and composition (Bedard 2007; Putirka 2008). Experimental pyroxene compositions and calculated K_D $(Fe\text{-}Mg)^{px\text{-}liq}$ values are provided in Table 3.1.

Based on the analysis of 785 experiments compiled in Rhodes (1979), Putirka (2008) found that K_D $(Fe\text{-}Mg)^{opx\text{-}liq}$ is approximately constant at 0.29 ± 0.06. Bedard (2007) complied experimental and natural data and found K_D $(Fe\text{-}Mg)^{opx\text{-}liq}$ decreases slightly with falling temperature and the MgO content of the melt. Using the functions provided by Bedard (2007), the K_D $(Fe\text{-}Mg)^{opx\text{-}liq}$ values for the temperature range studied are 0.27-0.31, and for the range of MgO in the glass phase of run-products are 0.24-0.31. Figure 3.2a shows the values of K_D $(Fe\text{-}Mg)^{opx\text{-}liq}$ calculated from experiments which lie within the range summarized above, except for Exp# Lat_3.5. This latter experiment contained relatively few melt pockets for measurement (Figure E1v), so it is unclear if the K_D $(Fe\text{-}Mg)^{opx\text{-}liq}$ reflects true disequilibrium or is a measurement artifact.

A value of 0.28 ± 0.08 for K_D $(Fe\text{-}Mg)^{cpx\text{-}liq}$ was established by Putirka (2008) based on a compilation of 1245 experiments. Clinopyroxene-melt pairs from experiments are generally consistent with this result except for Exp# B1_3.8 in which the K_D $(Fe\text{-}Mg)^{cpx\text{-}liq}$ is anomalously high.

Silicate glasses in run-products were traversed on the EPMA and LA-ICP-MS. No compositional gradients were observed for major elements or Cr, indicating homogeneity of the silicate glass. Most silicate minerals show no compositional zoning except for some pyroxenes in CCCS experiments, which results from two causes. The first is the break-down of chromite in experiments done at 0.1 MPa, indicated by Fe and Cr contents increasing from the core to the rim of orthopyroxene crystals (Figure E1e). Chromite inclusions are also commonly observed in the cores of these orthopyroxenes but not in the rims. This observation corresponds to the chromite-pyroxene peritectic reaction shown by Hill and Roeder (1974) and Barnes (1986a). Zoning initially occurs in an experiment done at 1230°C for a duration of 48 h and becomes more prevalent down temperature. A

96 h duration experiment was performed at 1230°C to investigate this reaction. The run-product shows that the reaction proceeds, consisting of significantly more uniform orthopyroxene crystals and fewer chromite crystals (Figure E1g). The second is due to Fe loss from the melt to the Fe-Ir alloy capsule in some CCCS experiments done at 0.5 GPa and 1 GPa. This results in minor zoning of pyroxenes in which Fe decreases from the core to the rim (see Section 3.2.1). No Fe loss was observed in experiments done at 0.1 MPa using Fe-Ir wires.

Overall homogeneity of the glass, reproducible run-products from crystallization and melting experiments, and K_D $(Fe\text{-}Mg)^{px\text{-}liq}$ values consistent with the literature indicate that, for CCCS experiments, durations of 48 h at 0.1 MPa, and 12 h at 0.5 GPa and 1 GPa are sufficient to approach equilibrium. Shorter run durations of 4-12 h were used for the silicate phase equilibrium experiments in graphite-lined Pt capsules done at 0.5 GPa and 1 GPa which are sufficient for this style of experiment given the K_D $(Fe\text{-}Mg)^{px\text{-}liq}$ values and homogeneity of run-product phases.

3.2 Calculation of fO_2 for High Pressure Experiments

3.2.1 Graphite-lined Pt Capsules

In experiments contained in graphite-lined Pt capsules, oxidation of graphite (C) produces CO and CO_2 according to the reactions:

$$C_{(graphite)} + \frac{1}{2}O_2 \leftrightharpoons CO_{(gas)}, \tag{3.3}$$

and

$$CO_{(gas)} + \frac{1}{2}O_2 \leftrightharpoons CO_{2\,(gas)}. \tag{3.4}$$

The reduction of Fe_2O_3 in the melt produces the oxidized carbon species by the following reactions:

$$C_{(graphite)} + Fe_2O_{3\,(melt)} \leftrightharpoons 2FeO_{(melt)} + CO_{(gas)}, \quad (3.5)$$

and

$$CO_{(gas)} + Fe_2O_{3\,(melt)} \leftrightharpoons 2FeO_{(melt)} + CO_{2\,(gas)}. \quad (3.6)$$

Medard *et al.* (2008) found graphite-lined Pt capsules to impose an fO_2 ranging from the graphite-carbon dioxide buffer (CCO) to CCO-0.8 between 0.5-3 GPa and 1100-1500°C. Therefore, reported fO_2 values (Series 4.0 in Table 2.1) correspond to CCO at pressure-temperature conditions using the calibration of Ulmer and Luth (1991), representing the maximum possible fO_2 for these experiments.

3.2.2 Fe-Ir Capsules

The fO_2 values for experiments contained in Fe-Ir alloy capsules were calculated using the Fe content in the alloy capsule and FeO in the run-product melt phase, according to Equation (2.1). The equilibrium constant (K_{eq}) of Equation (2.1) is:

$$K_{eq} = \frac{a_{FeO}}{a_{Fe}\, {fO_2}^{1/2}}, \quad (3.7)$$

and fO_2 can be calculated relative to the IW buffer (Hirschmann 2021) using the following expression:

$$\Delta IW = 2[\log(a_{FeO}) - \log(a_{Fe})], \quad (3.8)$$

in which a_{FeO} is the activity of the FeO in the silicate glass and a_{Fe} is the activity of Fe in the Fe-Ir alloy capsule. The activity of FeO in the silicate glass and Fe in the Fe-Ir alloy is defined as:

$$a_i = \gamma_i X_i, \quad (3.9)$$

in which a is the activity of component *i,* FeO or Fe*,* γ is the activity coefficient of component *i* and *X* is the mole fraction of component *i*. The activity coefficient of Fe in the alloy was calculated using the calibration of Borisov and Palme (2000) and a constant value of 1.7, determined by Holzheid *et al*. (1997), was used for the activity coefficient for FeO in the melt. These activity coefficient models were selected based on an experimental investigation summarized in Appendix C.

The fO_2 values were calculated for experiments done in Fe-Ir capsules in three iterations which are summarized in Table 3.2. For the first iteration, FeO_T of the melt and the alloy capsule composition were used to calculate the equilibrium fO_2 value. With the resultant fO_2 value, the calibration of Kress and Carmichael (1991) was employed to calculate the ratio of FeO to Fe_2O_3 from FeO_T in the melt. The capsule composition and the new FeO value were then used to calculate the fO_2 value for the second iteration. This was repeated for a third iteration in which the fO_2 value converges, with maximum difference between the second and third iteration of $\log fO_2 = 0.01$.

Results show that the average fO_2 of experiments contained in Fe-Ir alloy capsules is FMQ-0.27 ± 0.14. The small deviation from the intended fO_2 value at FMQ results from changing FeO content in the melt by silicate mineral crystallization, lowering FeO content of the melt and Fe loss from melt to the capsule.

3.2.3 Iron loss

Iron loss from experiments enclosed in Fe-Ir capsules was determined by comparing the amount of FeO in the starting material to the total amount in the run-product (solid and liquid phases) by mass balance:

$$C_i^{\circ} = C_i^{liq} F + C_i^{s}(1 - F), \quad (3.10)$$

in which F is the fraction of remaining melt, C_i° is the initial composition of component *i* in the melt, C_i^{liq} is the composition of component *i* in the remaining melt and C_i^{s} is the composition of component *i* in the mineral. The relative loss of Fe for these experiments, summarized in Table 3.2, ranges from 0.02-23.5%. Reasons for Fe loss to the capsule are unclear. A possible explanation could be that small heterogeneities were present in the capsule alloy and Ir-rich blebs alloyed with Fe from the melt.

3.3 Phase Equilibria

Figure 3.3 summarizes all experimental phase equilibria for the B1 and Lat compositions with an initial Cr content of 859 µg/g and 681 µg/g, respectively. Although no structural analysis was conducted, two populations of pyroxene were identified based on wollastonite (Wo) content (Table 3.1), the pyroxene calcium end-member. Pyroxene compositions, presented in Figure 3.2b, below 5 mol % Wo are an orthopyroxene and above are a low-Ca clinopyroxene, based on pyroxene nomenclature (Morimoto 1988). These are referred to as orthopyroxene and clinopyroxene hereafter.

3.3.1 B1 Composition

Orthopyroxene defines the silicate liquidus at all pressures which increases in temperature with rising pressure (1280°C at 0.1 MPa to 1370°C at 0.5 GPa to 1500°C at 1 GPa). At 0.5 GPa and 1 GPa, clinopyroxene is more abundant than orthopyroxene by 1230°C (Table 3.1). Chromite crystallizes in experiments done at 0.1 MPa, starting at

1280°C, and is no longer a crystallizing phase by 0.5 GPa. For the pressure-temperature range studied, plagioclase only appears in an experiment done at 1230°C and 1 GPa.

3.3.2 Lat Composition

Chromite-alone crystallization begins at 1280°C in experiments done at 0.1 MPa and 0.5 GPa. At 0.5 GPa, chromite is no longer a crystallizing phase by 1260°C and does not crystallize at 1 GPa. The silicate liquidus for the Lat composition is ~ 100-200°C lower than that of the B1 composition. At 0.1 MPa, the silicate liquidus mineral is plagioclase at 1230°C, at 0.5 GPa it is plagioclase and orthopyroxene at 1260°C, and at 1 GPa it is orthopyroxene at 1280°C with plagioclase joining later at 1230°C, which demonstrates the increased stability of plagioclase with decreasing pressure. By 1230°C, at 1 GPa, clinopyroxene is the only crystallizing pyroxene.

3.4 Textural Observations

Backscatter election (BSE) images of run-products are presented in Figure E1. Crystals in all run-products are evenly dispersed. Some run-products from experiments done at 0.1 MPa have a rim of crystals around the edge of the sample bead which are interpreted as quench crystals. Chromite crystals are sub-euhedral with a few anhedral crystals.

No textural differences are observed between orthopyroxene and clinopyroxene in BSE images, consequently, both are described as pyroxene here. Chromite inclusions in pyroxene are common in all chromite-saturated experiments.

3.4.1 B1 Composition

At 0.1 MPa, chromite crystals are <5 μm at 1280°C, decreasing to 1 μm or less by 1230°C. Experiments done at 0.1 MPa using the chromite-doped starting material contain slightly larger crystals, up to 5-8 μm at 1280°C, which decrease to 5 μm or less by 1230°C (Figure E1i).

Pyroxene crystals are mostly euhedral with a few subhedral crystals that decrease in size down temperature from 50 μm (on the long axis) to 30 μm at 0.1 MPa, 100 μm to 30 μm at 0.5 GPa and 50 μm to 15 μm at 1 GPa. Some pyroxenes in experiments done at 0.1 MPa, display dark cores with chromite inclusions and light rims, in BSE images. The onset of zoning occurs at 1230°C (Figure E1e) and becomes more prevalent with decreasing temperature, which corresponds to the aforementioned break-down of chromite. Sufficient Cr in experiments done at 0.1 MPa using the chromite-doped starting material results in uniform pyroxenes at 1230°C (Figure E1i). Minor zoning of pyroxenes is present in experiments done at 0.5 GPa and 1 GPa using Fe-Ir alloy capsules, which consists of lighter cores and darker rims, in BSE images, due to Fe loss from the melt to the capsule during the experiment (Figure E1u).

3.4.2 Lat Composition

At 0.1 MPa, chromite crystals are <5 μm at 1280°C, decreasing to 1 μm or less by 1170°C. Again, experiments done at 0.1 MPa using the chromite-doped starting material contain slightly larger crystals of ~ 5 μm at 1280°C and 1230°C. Plagioclase forms euhedral laths where present. At 0.1 MPa, plagioclase increases in size with falling temperature from 15 μm at 1230°C to 30 μm at 1170°C. In high pressure experiments, plagioclase is present at 1230°C and is ≤ 30 μm at 0.5 GPa and ≤10 μm at 1 GPa.

Pyroxene in experiments done at 0.1 MPa and 0.5 GPa is present as euhedral to subhedral oikocrysts which are ≤70 μm (Figure E1h). Pyroxene crystallizing at 1 GPa decreases in size from ~25 μm at 1280°C to 10 μm or less at 1230°C.

3.5 Chromite Chemistry

Table 3.3 summarizes experiments in which chromite crystallized and the chromite composition. The ferric and ferrous content of chromite was calculated from stoichiometry using the method of Barnes and Roeder (2001). The covariation of Cr# [Cr/(Cr+Al)] and Fe# [Fe^{2+}/(Fe^{2+}+Mg)] of chromite crystallizing over the temperature range investigated at 0.1 MPa is portrayed in Figure 3.4. The variation of trivalent cations (Cr, Al and Fe^{3+}) in experimental chromite as a function of temperature and pressure is portrayed in Figure 3.5a and Figure 3.5b, respectively.

Chromite composition is strongly influenced by melt composition and reflects the evolving melt chemistry as other minerals crystallize. At all conditions, chromite produced by the Lat composition is more Al-rich compared to those produced by the B1 composition due the high-Al of the Lat composition relative to B1. Overall, B1 experimental chromite is more Cr- and Mg-rich than chromite produced by the Lat composition.

3.5.1 Effect of Temperature

Figure 3.4 shows that the Cr# of chromite decreases with falling temperature from ~0.75 to 0.63 for the B1 composition and 0.61 to 0.5 for the Lat composition. The Fe# of chromite produced by the B1 composition increases with decreasing temperature from ~0.39-0.48, whereas there is little change in Fe# of chromite with decreasing temperature

for Lat chromites. The differing Fe# trend in B1 and Lat corresponds to the higher orthopyroxene-in temperature for the B1 composition (1280°C vs 1170°C for B1 and Lat, respectively) and therefore, higher FeO/MgO in the melt. In the trivalent cation plot (Figure 3.5a), both compositions show increasing proportions of Al and Fe^{3+} in crystallizing chromite with decreasing temperature.

3.5.2 Effect of Pressure

In the trivalent cation plot (Figure 3.5b), at constant temperature and variable pressure, it is challenging to determine the effect of pressure on chromite composition due to the impact of co-crystallizing minerals on the melt composition. However, experiments done at 1280°C using the Lat composition crystallize chromite-alone. This series shows a general increase in Al with increasing pressure. This result is consistent with observations from chromite in natural samples (Dick and Bullen 1984) and experimental data compiled by Nikolaev *et al.* (2018).

3.6 CCCS

The Cr content of melt measured in run-products is presented Table 2.1, and for experiments in which chromite crystallizes, this value represents the CCCS. In some high pressure experiments where melt pockets were too small for measurement using LA-ICP-MS, the Cr content of melt was measured using the EPMA instead. Figure 3.6 compares CCCS values measured using LA-ICP-MS and EPMA, demonstrating that the measurements display close to a 1:1 relationship. This indicates that average CCCS values determined by the EPMA, while less precise, are acceptable.

The CCCS is plotted as a function of temperature in Figure 3.1, which highlights the slight difference in CCCS between compositions. This difference is likely due to compositional effects since all other variables are consistent (temperature, pressure and fO_2).

3.6.1 Effect of Temperature

The CCCS values measured from experiments done at 0.1 MPa and FMQ for the B1 composition decrease from 722 ± 35 µg/g at 1280°C to 228 µg/g at 1170°C and the Lat composition decrease from 587 ± 20 µg/g at 1280°C to 252 µg/g at 1170°C. The variation in experimental CCCS is plotted as a function of inverse temperature in Figure 3.7 and is compared with CCCS data from previous studies done at 0.1 MPa using basaltic compositions (Murck and Campbell 1986; Barnes 1986a; Roeder and Reynolds 1991). The same trend is displayed in all studies in which the CCCS decreases with decreasing temperature. Results of this investigation are in good agreement with results of Murck and Campbell (1986) and Roeder and Reynolds (1991) and together are defined by Equations 1 and 2 in Table 3.4, for the Lat and B1 composition, respectively. Data from Barnes (1986a) is offset from all other data and is, therefore, excluded from these regressions.

3.6.2 Effect of Pressure

Murck and Campbell (1986), Barnes (1986a) and Roeder and Reynolds (1991) found fO_2 to be the strongest control on the CCCS, which decreases with increasing fO_2, with the largest change occurring around FMQ-5.5, decreasing towards FMQ (Figure 1.4). Therefore, before evaluating the effect of pressure on the CCCS, it is important to assess

the effect of small variations in experimental fO_2, which ranges from FMQ+0.10 to FMQ-0.51. Figure 3.8 portrays the CCCS as a function of ΔFMQ. At 1230°C, there is little change in CCCS over the range of fO_2. At 1280°C, there is an increase in the CCCS with decreasing fO_2 with the largest increase recorded between experiments done at 0.1 MPa and FMQ+0.1 and at FMQ-0.4 corresponding to ~ 130 µg/g Cr for the B1 composition and ~115 µg/g Cr for the Lat composition. For experiments at similar fO_2 in Figure 3.8, there appears to be no correlation between pressure and the CCCS. Experimental CCCS values measured at 1280°C and 1230°C are averaged over the range of experimental fO_2 and portrayed in Figure 3.9 as function of pressure. Averages exclude Exp # Lat_3.7, an outlier with a CCCS value of 1057 µg/g at 1280°C. Reasons for the outlier are unclear, however, this experiment did not crystallize orthopyroxene whereas a repeat experiment did. For the B1 composition, the average CCCS over the pressure interval studied is 430 ± 22 µg/g at 1230°C and 811 ± 27 µg/g at 1280°C. The average CCCS over the pressure interval studied for the Lat composition is 411 ± 24 µg/g at 1230°C and 708 ± 45 µg/g at 1280°C. Overall, results indicate that there is no significant or systematic change in the CCCS with pressure.

Roeder and Reynolds (1991) describe a "slight" increase in CCCS with pressure of ~330 µg/g at the same log fO_2 value. Unlike this study, Roeder and Reynolds (1991) did not investigate the CCCS as a function of relative fO_2 but rather over a range of log fO_2 values. Using the function defined by CCCS data collected at 0.1 MPa and 1300°C by Roeder and Reynolds (1991) (Figure 1.4), the CCCS can be calculated at the same relative fO_2 as their 1 GPa experiment. Results yield ~ 40 µg/g increase in experimental CCCS from 0.1 MPa to 1 GPa, both at 1300 °C and FMQ-1.7. This small difference is consistent with results of this study.

3.7 Pyroxene Composition

The compositions of run-product pyroxenes are summarized in Table 3.1 and portrayed in Figure 3.2 and Figure 3.11.

Experimental orthopyroxenes are all enstatite (En) based on their En number [En#=Mg/(Ca+Mg+Fe_T)] which for the B1 composition ranges from 0.87-0.80 at 0.1 MPa, 0.85-0.77 at 0.5 GPa, and 0.85-0.80 at 1 GPa. The En# of orthopyroxene produced by the Lat composition is 0.79 at 0.1 MPa, 0.77-0.78 at 0.5 GPa, and 0.80 at 1 GPa. Therefore, at constant pressure, En# of orthopyroxene generally decreases with falling temperature, and at constant temperature En# decreases with rising pressure.

Experimental clinopyroxenes are all low in calcium (Figure 3.2b) and classified as pigeonite ($5 \leq Wo \leq 25$ mol %) following the description of Bertka and Holloway (1993). The same En# trend is observed for clinopyroxene but with lower Mg contents resulting in an En# of 0.67-0.69 for clinopyroxene produced by the B1 composition and 0.61 for those produced by the Lat composition.

3.7.1 Mass Fraction

Mass fractions of pyroxene crystallizing in experiments were calculated by mass balance using Equation 3.10. There are not enough pyroxene data for the Lat composition in this study to evaluate the change in pyroxene mass fraction with pressure and temperature. The calculated mass fraction of pyroxene produced by the B1 composition are portrayed in Figure 3.10 as a function of temperature at each pressure investigated. Resulting linear fit parameters, Equations 6, 7, and 8, are summarized in Table 3.4. Results from B1 show that the mass fraction of pyroxene increases with falling

temperature. At constant temperature, the mass fraction increases over the pressure interval studied from 0.10-0.31 at 1230°C and 0.05-0.27 at 1280°C.

3.7.2 Chromium Content

The Cr_2O_3 content of pyroxenes produced by the Lat composition in chromite-saturated experiments is consistently higher than B1 pyroxenes at all pressures.

Clinopyroxenes, in this study, do not crystallize in enough experiments to establish the effect of temperature and pressure Cr_2O_3 content in clinopyroxene and therefore, these effects are only explored for orthopyroxene. However, where both pyroxene compositions are present, there is no systematic difference in Cr_2O_3 content observed between them (Figure 3.2b). Chromium content in clinopyroxene also seems to be correlated to Wo content, in which Cr_2O_3 increases with increasing Wo number [Wo#=Ca/(Ca+Mg+Fe_T)]; Figure 3.2b). This result is consistent with that of Papike *et al.* (2016) who showed that Ca, which occupies the M2 site in pyroxene, strongly influences Cr partitioning in both orthopyroxene and clinopyroxene, although this effect is not observed for orthopyroxene in this study (Figure 3.2b).

3.7.2.1 Effect of Temperature

Orthopyroxene data for the Lat composition are insufficient to evaluate the effect of temperature. However, in chromite-saturated experiments done at 0.1 MPa and 1280°C to 1170°C using the B1 composition, orthopyroxene in run-products has an average of 0.52 ± 0.04 wt% Cr_2O_3, in which Cr content of orthopyroxene shows no systematic change with temperature. This is consistent with results of Barnes (1986a) who conducted experiments at 0.1 MPa and found fO_2 to be the strongest control on Cr content in

orthopyroxene, followed by temperature in which the Cr content increases with decreasing fO_2 and decreases with falling temperature. Barnes (1986a) found the effects of both diminish at fO_2 values above ~ FMQ-1.5, resulting in roughly constant Cr contents in orthopyroxene.

3.7.2.2 Effect of Pressure

Figure 3.11a shows the Cr_2O_3 content of experimental orthopyroxene as a function of pressure for chromite-saturated experiments at variable temperature and fO_2. The Cr_2O_3 content in orthopyroxene produced by the B1 composition increases from 0.52 ± 0.04 wt % at 0.1 MPa to 0.92 ± 0.3 wt % at 0.5 GPa and to 1.62 ± 0.09 wt % at 1 GPa. The Cr_2O_3 of orthopyroxene produced by the Lat composition increases from 0.67 ± 0.20 wt % at 0.1 MPa to 1.36 ± 0.27 wt % at 0.5 GPa and to 2.12 ± 0.12 wt % at 1 GPa. Therefore, results indicate that the Cr content of orthopyroxene is sensitive to pressure in a chromite-saturated system from the substantial observed increase in Cr_2O_3 (wt%) in experiments done at 0.1 MPa to 1 GPa.

3.7.2.3 $D_{Cr(opx/liq)}$

The calculated values of $D_{Cr(opx/liq)}$ for experimental orthopyroxenes are presented in Table 3.1 and are defined as:

$$D_{Cr}^{opx/liq} = \frac{C_{Cr}^{opx}}{C_{Cr}^{liq}}, \tag{4.1}$$

in which C_{Cr}^{opx} is the concentration of Cr in orthopyroxene and C_{Cr}^{liq} is the concentration of Cr in the coexisting melt.

The values of $D_{Cr(opx/liq)}$ calculated for B1 orthopyroxene produced in chromite-saturated experiments are plotted as a function of inverse temperature at each pressure investigated in Figure 3.12. Equations 3, 4, and 5, summarized in Table 3.4, describe the temperature dependence of $D_{Cr(opx/liq)}$ at 0.1 MPa, 0.5 GPa, and 1 GPa, respectively. In this study, pyroxene produced by the Lat composition is too limited to establish a $D_{Cr(opx/liq)}$ trend as a function of temperature. However, results from the B1 composition in Figure 3.12 show that $D_{Cr(opx/liq)}$ increases with decreasing temperature. This trend was well described by Barnes (1986a), however, a pressure dependence has not been as well documented. Results demonstrate an increase in $D_{Cr(opx/liq)}$ with rising pressure which is consistent with the previous experimental study of Auwera *et al*. (2000). Auwera *et al*. (2000) attributed this to Cr^{3+} substitution in orthopyroxene at high pressure being more favourable due to the smaller ionic radius of Cr^{3+} relative to Mg^{2+} and Fe^{2+}. Chromium, which occupies the M1 site in pyroxene, is coupled with Al, in the tetrahedral site, for charge balancing (Papike *et al.* 2016) which also increases with rising pressure in experimental orthopyroxenes, demonstrated in Figure 3.11b.

CHAPTER 4: DISCUSSION

4.1 Evaluation of MELTS Modelling Software

A key component of the pressure reduction hypothesis is the thermodynamic MELTS model, by Latypov *et al*. (2018), constructed using alphaMELTS (Smith and Asimow 2005). The MELTS family of software (Ghiorso and Sack 1995) is a an experimentally calibrated thermodynamic modelling software that is designed to calculate phase equilibria for igneous systems. AlphaMELTS is a front-end interface to MELTS that includes various improvements such as updated activity-compositional relations and increased automation. However, MELTS is known to model chromite poorly (Section 1.3.6; Asimow *et al*. 1995; Nikolaev *et al.* 2018). In this study, the MELTS software's ability to model chromite composition and the CCCS are evaluated in the context of the pressure reduction hypothesis through direct comparison to experimental results.

Isobaric batch crystallization simulations were performed at conditions ranging from 0.1 MPa to 1 GPa, 900 to 1500°C, and FMQ to FMQ-0.4, using the B1 and Lat experimental starting compositions (See Appendix F for example of set-up files). To be consistent with Latypov *et al.* (2018), MELTS results presented here are obtained using alphaMELTS version 1.4.1., however, simulations were also preformed using the latest version, alphaMELTS 2. Crystallization sequences are similar in both versions, but phase-in temperatures differ by 10-30°C.

4.1.1 Chromite Composition

Chromite compositions predicted by MELTS from chromite saturation in simulations (1270°C for the B1 composition and 1230°C for the Lat composition) to 1200°C are compared to experimental chromite compositions in Figure 3.4 and Figure 3.5. The

covariation trend of Cr# and Fe# exhibited by chromite crystallizing in experiments done at 0.1 MPa is reproduced by MELTS for both compositions. The Cr#'s of chromite produced by the B1 composition are in good agreement with MELTS predictions, generally within uncertainty of experimental values at a given temperature, and Fe#'s of chromite are slightly higher in MELTS at a given temperature. In contrast, the Fe#'s of chromite produced by the Lat composition are in excellent agreement and Cr#'s of chromite are slightly lower in MELTS at a given temperature.

The evolving proportions of trivalent cations in chromite produced by the B1 and the Lat compositions with temperature, Figure 3.5a, and pressure, Figure 3.5b, are broadly similar to MELTS predictions. However, MELTS consistently overestimates the proportion of Fe^{3+} in chromite by 5-10 %.

4.1.2 CCCS

The CCCS predicted by MELTS for both compositions are compared to experimentally determined values as functions of temperature and pressure in Figure 3.1 and Figure 3.9, respectively. At 0.1 MPa, the CCCS predicted by MELTS is higher than measured in experiments, resulting in higher chromite crystallization temperatures than predicted (Figure 3.1). This indicates that chromite crystallization is favoured even more so at low pressure than MELTS suggests, strengthening the pressure reduction hypothesis. However, from 0.1 MPa to 1 GPa, MELTS predicts that the CCCS decreases by ~ 420 μg/g at 1230°C and ~ 615 μg/g 1280°C for both compositions (Figure 3.9), whereas experiments from this study and Roeder and Reynolds (1991) show that the CCCS remains relatively constant over this pressure interval. This result clearly indicates that MELTS overestimates the effect of pressure on the CCCS.

4.1.3 Phase Equilibria

The phase equilibria predicted by MELTS for the B1 and Lat compositions are compared to experimental results in Figure 3.3. Experimental silicate-in temperatures are generally within 30°C of MELTS predictions and the crystallization orders are consistent. For the Lat composition, the measured chromite-in temperature at 0.1 MPa is 1280°C, which is 50°C higher than the MELTS prediction, resulting in a larger interval of chromite-alone crystallization in experiments at low pressure. This is in contrast to the previous work by Nikolaev *et al.* (2018) who found that MELTS calculated chromite-in temperatures are higher than measured. However, the Al-rich nature of the Lat composition is likely stabilizing chromite at a higher temperature. In contrast, the measured chromite-in temperature for the B1 composition at 0.1 MPa is in good agreement with MELTS predictions. Experiments show that chromite is no longer a crystallizing phase by 0.5 GPa for the B1 composition and by 1 GPa for the Lat composition, which is inconsistent with MELTS. To understand this difference, the crystallizing phases in an experiment done at 0.1 MPa and 1280°C using the B1 composition are compared to phases in an experiment done at 1 GPa and 1280°C in BSE images in Figure 4.1. Orthopyroxene crystallizes in both experiments but without chromite, until 0.1 MPa. Not only does the modal abundance of orthopyroxene increase considerably at 1 GPa but experiments also show that $D_{Cr(opx/liq)}$ (Figure 3.12) is higher at 1 GPa than 0.1 MPa. Consequently, orthopyroxene consumes more Cr from the melt with increasing pressure, preventing chromite saturation. This effect is not predicted by MELTS because Cr is not included in the model for pyroxenes. This result also indicates that reduction of pressure can promote chromite crystallization, as the modal abundance and $D_{Cr(opx/liq)}$ of orthopyroxene decrease with pressure, allowing for more Cr to be

available for chromite crystallization. This is consistent with the hypothesis of Latypov *et al*. (2018), however, it is not changes in the CCCS that produce the desired result, but instead the mass balance of Cr involving changes in orthopyroxene partitioning and abundance.

4.2 Parent Magmas of the Bushveld Complex

In this study, the chromite-generating capacity of two different parental liquids proposed for the Critical Zone (CZ), B1 and Lat, are evaluated in terms of their phase equilibria and CCCS over a similar pressure range as estimated for the emplacement of Bushveld magmas (0.06 to 0.3 GPa; Waters and Lovegrove 2002; Wallmach *et al*.1989). Although past literature has discussed the various lines of geochemical and petrological support for the B1 and Lat compositions as parental to some portions of the Lower Zone (LZ) and CZ (B1; LZ and Lower Critical Zone (LCZ), Lat; Upper Critical Zone (UCZ)), there are limited (B1; Sharpe and Irvine 1983; Cawthorn and Davies 1983; Barnes 1986a; Cawthorn and Biggar 1993) to no (Lat) corroborating experimental phase equilibria and mineral composition data. In this section, an additional test for which of these compositions could be viable parental liquids to the CZ chromitites is made by comparing the phase equilibria and mineral compositions measured in this study to the natural samples.

4.2.1 Chromite Compositions

Compositions of chromite from massive chromitites in the CZ (Lower Group, Middle Group, and Upper Group; see Figure 1.1 for stratigraphy) compiled from Von Gruenewaldt and Worst (1986), Naldrett *et al.* (2009), and Langa *et al.* (2021) are

compared to 0.1 MPa experimental data on the Cr# and Fe# covariation plot (Figure 3.4) and trivalent cation plot (Figure 3.5a). Experiments done at 0.5 GPa and 1 GPa used chromite-doped starting materials, shifting chromite compositions to unnaturally high Cr levels, causing an upward bias in the Cr component of chromite and, therefore, are not comparable to Bushveld chromitites.

On the covariation plot, B1 experimental chromites define an array similar to the aforementioned "trend B" for CZ chromitites described by Naldrett *et al*. (2009), in which Cr# decreases with increasing Fe# in response to orthopyroxene fractionation. In experiments done at 0.1 MPa, the Lat composition crystallizes predominantly chromite-alone and therefore, lacks a silicate fractionation trend, and the Fe# of chromite remains relatively unchanged as the Cr# of chromite decreases. The Cr#'s for B1 chromite crystallizing between 1280-1200°C span the range of compositions observed in the natural chromitites. In contrast, only the most primitive chromite compositions produced by the Lat composition overlap with the most Cr-poor compositions in natural chromitites (Figure 3.4). In terms of the Fe# of chromite, both B1 and Lat overlap with the least evolved (~Fe#<0.5) of the Bushveld compositions.

Chromite and silicate minerals in natural systems can deviate from their original compositions through subsolidus re-equilibration with adjacent silicates (Barnes and Roeder 2001) and interstitial liquid (trapped liquid shift; Barnes 1986b). The fast exchange between Fe^{2+} and Mg^{2+} can shift the Fe# of chromite to more evolved compositions (higher Fe#). The modal proportion of chromite relative to the liquid or silicate reservoir controls the magnitude of the shift (Barnes 1986b). Consequently, subsolidus re-equilibration predominantly affects chromite disseminated in silicate-rich cumulates, along the margins of chromitite seams or in semi-massive chromitites (Barnes

and Roeder 2001; Langa *et al.* 2021). Therefore, experimental chromite compositions are only compared to chromite compositions from massive chromitites in the CZ in Figure 3.4 and 3.5a. The agreement between Cr#'s of experimental B1 chromite with values from the natural chromitites (Figure 3.4) suggests that the magmatic character of the natural chromite has been preserved in the CZ. Experiments define the magmatic chromite composition trend for the Fe#, which, over the temperature interval investigated, is Fe#<0.48 for chromite produced by the B1 composition. Subsolidus re-equilibration could contribute to the wide range in Fe# for the natural chromitites (Figure 3.4) but the extent is uncertain.

Chromite compositions cast on the trivalent cation diagram (Figure 3.5a) demonstrate excellent agreement between B1 experimental chromite and the Bushveld compositions. As expected, Lat chromite compositions only overlap with the most Al-rich natural compositions, and only the most Cr-rich and Fe-poor Lat compositions do so.

4.2.2 Orthopyroxene Compositions

Figure 4.2a portrays the variation of Mg# [Mg# = Mg/(Mg+ Fe^{2+})] with stratigraphic height in natural orthopyroxenes measured in the LZ and CZ. The Mg# is subject to frequent reversals to more primitive values, commonly interpreted as magma replenishment, but overall, decreases up section. Values of Mg# range from 0.88-0.85 in the LZ, 0.88-0.82 in the LCZ, and 0.82-0.79 in the UCZ (Cawthorn 2007, Eales and Costin 2012, Cawthorn 2015). For comparison, the Mg# of experimental orthopyroxenes at all pressures is portrayed as a function of temperature in Figure 4.2b. Over the pressure range investigated, orthopyroxene-in temperatures vary from 1170-1500°C, however, the Mg#'s of primitive orthopyroxene are quite similar, often within uncertainty. The Mg#'s

for all B1 experimental orthopyroxene are in excellent agreement with the LZ and LCZ compositions. Albeit, low pressure experimental orthopyroxenes are most relevant to the Bushveld, which, for the B1 composition, range in Mg# from 0.88-0.82 at 0.1 MPa. Upon further cooling the B1 composition would likely reproduce the Mg# of the UCZ as well. The Lat composition crystallizes orthopyroxene with a Mg# of 0.81 which is consistent with the UCZ.

As noted by Cawthorn (2015), the Cr content of orthopyroxene throughout the LZ and CZ is very consistent. The average Cr_2O_3 content measured in orthopyroxenes is 0.42-0.5 wt%, 0.47 wt%, and 0.44-0.5 wt%, for the LZ, LCZ, and UCZ respectively (Cawthorn 2007 and references therein). Results of this study show that, in addition to fO_2 (Barnes 1986a), pressure exerts a strong control on $D_{Cr(opx/liq)}$ in a chromite-saturated system. At all pressures, orthopyroxenes produced by the Lat composition in chromite-saturated experiments contain higher Cr_2O_3 (0.68-2.12 wt%) than those observed in the Bushveld. Chromium contents in orthopyroxene crystallizing from the B1 composition in experiments done at 0.1 MPa are in good agreement with the natural compositions (0.5 ± 0.03 wt% Cr_2O_3). Employing the regression defined for Cr_2O_3 as a function of pressure for B1 experimental orthopyroxene (Figure 3.11a) yields 0.58 wt% Cr_2O_3 in orthopyroxene at 0.06 GPa and 0.86 wt% Cr_2O_3 at 0.3 GPa, which are both slightly higher than the LZ and CZ range. This difference might be too small to be of significance, but it could suggest that the LZ and CZ crystallized at the lower end of the proposed pressure interval for the Bushveld or that they crystallized at a higher fO_2 than investigated in this study (Barnes 1986a). As a complementary approach, the Al_2O_3 content of orthopyroxene is also an indication of crystallizing pressure in an Al-saturated system, which increases with pressure (Longhi *et al*. 1992). The Al_2O_3 content of experimental orthopyroxene

from the B1 composition increases from 1.2 ± 0.3 wt% at 0.1 MPa to 3.4 ± 0.02 wt% at 1 GPa (Figure 3.11b). The regression defined for Al_2O_3 involving B1 experimental orthopyroxene compositions as a function of pressure yields 1.2 wt% Al_2O_3 at 0.06 GPa and 1.7 wt% Al_2O_3 at 0.3 GPa. Bushveld orthopyroxenes contain less than 1.5 wt% Al_2O_3 (Cawthorn 2015 and references therein) which, from Figure 3.11b, corresponds to crystallization conditions of ~ 0.2 GPa or lower for the LZ and CZ. Orthopyroxene produced from the Lat composition is too Al-rich to be consistent with those in the Bushveld, ranging from 2.7 wt % at 0.1 MPa to 6.1 ± 0.1 wt % at 1 GPa (Figure 3.11b).

4.2.3 Phase Equilibria

The crystallization sequence of the LZ to LCZ in the Bushveld is as follows: olivine + chromite → olivine + orthopyroxene + chromite → orthopyroxene + chromite (Barnes *et al.* 2010). The LZ consists of 60% olivine-bearing rocks (harzburgite and dunite) which decrease significantly to less than 10% in the LCZ, which contains two main harzburgite intervals (Maier *et al.* 2013 and references therein). Olivine did not crystallize in experiments involving the B1 composition, which reproduced only the end of this sequence: orthopyroxene + chromite. Olivine crystallizes in the phase equilibrium experiments of Sharpe and Irvine (1983) for a brief 15°C interval (1275-1260°C) indicating the possibility that this interval was missed in the current experiments. The experiments of Sharpe and Irvine (1983) were conducted at 0.1 MPa using a natural sample of B1, which is compositionally similar to B1 of this study. Aside from the absence of olivine, the 0.1 MPa phase equilibria measured in this study are in remarkable agreement with Sharpe and Irvine (1983) in which orthopyroxene and chromite crystallization temperatures are within 10°C. Collectively, results suggest that the B1

composition can reproduce the crystallization order observed in the LZ and LCZ. Albeit, olivine, which is most stable at low pressures, only crystallizes over a small interval at 0.1 MPa. Therefore, questions regarding the ability of a B1 composition to produce the mass of olivine observed in the LZ are valid (Eales and Costin 2012; Wilson 2012), which has led to the proposal that a more primitive, komatiitic parent is responsible for the LZ and LCZ (Eales and Costin 2012).

The crystallization sequence of the UCZ in the Bushveld is as follows: orthopyroxene + chromite (± olivine) → plagioclase + orthopyroxene (Barnes *et al*. 2010). Experiments in this study were not done at low enough temperatures to capture plagioclase-in for the B1 composition at 0.1 MPa and 0.5 GPa. Other experimental phase equilibria studies using different estimates of the B1 composition (Sharpe and Irvine 1983; Cawthorn and Davies 1983; Barnes 1986a; Cawthorn and Biggar 1993) crystallize plagioclase between 1170-1160°C, consistent with the crystallization sequence of the UCZ. Even so, the B1 composition cannot solely be responsible for the UCZ due to the observed increase in initial Sr ratio in the UCZ (Kruger 1994), which is inconsistent with measured initial Sr ratio for B1.

For the proposed depth of emplacement, the Lat composition crystallizes chromite → chromite + plagioclase → chromite + plagioclase + orthopyroxene, which is inconsistent with both the original MELTS model proposed by Latypov *et al*. (2018) and the UCZ crystallization sequence.

4.3 Modelling Chromite Crystallization

Chromite-in temperatures can be modelled for different initial Cr contents in the B1 and Lat compositions using CCCS data and silicate phase equilibria established by the

experiments of this study. Because results show that the CCCS lacks a pressure dependence at constant relative fO_2, the CCCS at all pressures (0.1 MPa - 1 GPa) can be modelled using a temperature dependence only. Equations 1 and 2 (Table 3.4; Section 3.6.1) are used to calculate the CCCS as a function of temperature and predict chromite-in temperatures for the B1 and Lat compositions.

With data provided in this study, it is possible to extend the crystallization model beyond chromite-alone and predict the temperature interval over which chromite will continue to crystallize with other phases. To do this, batch crystallization is modelled by mass balance employing phase mass fractions and $D_{Cr(opx/liq)}$ (Figure 3.10 and 3.12). In the pressure-temperature space studied, data were too limited to define trends for clinopyroxene so for the purpose of this exercise, all pyroxene is modelled using $D_{Cr(opx/liq)}$. This can reasonably be done for the B1 composition down to the lowest experimental temperatures investigated of 1170°C at 0.1 MPa and 1230°C at both 0.5 GPa and 1 GPa. Unfortunately, $D_{Cr(opx/liq)}$ data are limited for the Lat composition and would require additional low temperature experiments to model chromite and coexisting silicates with certainty.

At a given temperature, pressure, and initial Cr content of the melt, chromite saturation conditions are determined by calculating the Cr in the melt (C_{Cr}^{liq}):

$$C_{Cr}^{liq} = \frac{C_{Cr}^{\circ} - C_{Cr}^{px} F^{px}}{F^{liq}}, \quad (4.2)$$

in which C_{Cr}° is the initial Cr content of the melt, C_{Cr}^{px} is the Cr content of pyroxene, F^{liq} is the mass fraction of remaining melt, F^{px} is the mass fraction of pyroxene. The F^{px} is calculated using Equations 6, 7, and 8 in Table 3.4 and F^{liq} = 1 - F^{px}, assuming the mass

fraction of chromite is negligible (~ ≤0.01). The C_{Cr}^{px} is calculated for pyroxene at chromite-saturation, yielding:

$$C_{Cr}^{px} = \mathrm{D}_{\mathrm{Cr(opx/liq)}} \times \mathrm{CCCS}, \quad (4.3)$$

in which $D_{Cr(opx/liq)}$ is calculated from Equations 3, 4, and 5 in Table 3.4.

If C_{Cr}^{l} exceeds the CCCS, chromite will crystallize. By interpolating between functions at 0.1 MPa and 0.5 GPa of pyroxene mass fractions and $D_{Cr(opx/liq)}$ (Figure 3.10 and 3.12) chromite crystallization can be predicted between 0.1 GPa to 0.3 GPa, the pressure interval most relevant to the Bushveld.

Figure 4.3a portrays the calculated chromite-in curve for the Lat composition using 700 µg/g Cr, a value similar to that of the MELTS thermodynamic model by Latypov *et al.* (2018). Figure 4.3b portrays the calculated chromite-in curve for the B1 composition containing 1000 µg/g Cr and 1400 µg/g Cr, and the shaded regions correspond to modelled chromite-alone crystallization and chromite coexisting with pyroxene.

In this exercise, orthopyroxene and clinopyroxene were not differentiated but it is known that $D_{Cr(cpx/liq)} > D_{Cr(opx/liq)}$ (Barnes 1986a). Consequently, chromite may cease to form at higher temperatures than the model predicts, depending on the clinopyroxene-in temperature. The simulations by MELTS predict that between 0.1 MPa and 0.2 GPa, the clinopyroxene-in temperature is between 1150-1170°C.

4.4 Pressure Reduction Hypothesis

The low-pressure interval of chromite-alone crystallization from the original thermodynamic model by Latypov *et al.* (2018) is reproduced by experiments of this study, indicating that pressure reduction is a plausible mechanism to produce a chromite

layer. The model constructed in this study predicts chromite-alone crystallization from 0.1 MPa to 0.5 GPa for the Lat composition (Figure 4.3a) with a maximum temperature interval of 50°C at 0.1 MPa. This temperature range corresponds to ~ 280 μg/g decrease in Cr content of the melt. Using the average composition of chromite produced by the Lat composition, a chromite density of 4500 kg/m^3 (Eales 2000) and a density of 2600 kg/m^3 for basaltic magma (Lesher and Spera 2015), the chromite-alone interval would crystallize ~ 0.5 mm of chromite from 1 m^3 of magma. Therefore, to crystallize a 1 m thick chromitite, as observed in the Critical Zone, a ~ 2 km thick column of magma is required at a minimum.

However, the composition used in the thermodynamic model by Latypov *et al.* (2018) is not likely a parent magma to the Bushveld because it is unable to reproduce the crystallization sequence or phase compositions observed in the UCZ. Importantly, experiments show that the chromite that would crystallize is too Cr-poor to be responsible for Bushveld chromitites. It is apparent that the high-Al of the Lat composition, relative to other parent magmas proposed for the Bushveld, impacts orthopyroxene and chromite composition and potentially stabilizes chromite at higher temperatures, which accentuates the chromite-alone crystallization interval.

Applying the pressure reduction hypothesis to the B1 composition, Figure 4.3b shows, for a B1 magma with the commonly proposed 1000 μg/g Cr, an interval of chromite-alone crystallization only occurs below 0.1 GPa, for a maximum of 30°C at 0.1 MPa. Using the same method as above, this corresponds to a change in CCCS of ~ 270 μg/g, yielding 0.5 mm of chromite per m^3 of magma or ~1 m thick chromitite layer from a ~ 2 km magma column. Figure 4.3b also shows that a Cr content at or above the high-end of previous estimates for B1 (>1400 μg/g Cr) is required to achieve a chromite-alone

crystallization interval between 0.06 to 0.3 GPa. Crystallization of B1 with a Cr content of 1400 μg/g (Harmer and Shape 1985) yields a chromite-alone interval below 0.3 GPa with a maximum of 70°C at 0.1 MPa. The same B1 with 1400 μg/g Cr would yield ~1 m of chromite from 1 km of magma at 0.1 MPa.

These results indicate that an unusually high Cr content in the B1 magma would be required for an interval of chromite-alone crystallization to occur in the pressure range estimated for the emplacement of Bushveld magmas. Even so, at least a kilometre of magma is necessary to crystallize 1 m of chromitite, requiring several kilometres to produce the up to 20 m of chromitite observed (Veksler and Hou 2020 and references therein) in the CZ, which itself is just over 1 km thick. Therefore, the pressure reduction model would require effective extraction of chromite from significant volumes of a Cr-enriched B1 magma to produce the chromitites observed in the CZ. Many authors suggest that the large volume of residual magma was removed by lateral or vertical expulsion; however, it is challenging to validate this as the solidification products of this volume of magma have not been found and could have been removed by erosion (Eales 2000; Naldrett *et al.* 2012; Latypov *et al.* 2018).

CHAPTER 5: CONCLUSIONS

This study sought to determine the effect of pressure on chromite crystallization and evaluate the pressure reduction mechanism proposed by Latypov *et al*. (2018) to produce the Bushveld chromitites. This was done by conducting laboratory experiments to determine phase equilibrium and chromite solubility with careful consideration of controlling fO_2. By exploring the B1 magma, in addition to the composition employed in the pressure reduction model, this study provides one of the most complete experimental investigations of the phase equilibria and chromite solubility for this proposed parental composition in pressure-temperature space. From experimental and model results several key conclusions can be made:

- Pressure dependence on the CCCS at constant relative fO_2 is insignificant and, as a result, the CCCS can be modelled considering only the effects of temperature, melt composition, and fO_2.
- The B1 magma reproduces the crystallization order (orthopyroxene + chromite) of the LCZ and mineral compositions of the LZ and LCZ with high fidelity. At low pressure, current experiments did not crystallize olivine which is required to account for the harzburgites and dunites in the LZ. However, previous experimental studies that explored the low pressure near-liquidus temperature interval of the B1 composition more precisely did yield an interval of olivine crystallization. This suggests that a B1 magma can reproduce the crystallization order of the LZ.
- Chromite and orthopyroxene produced by the Lat composition in experiments are too Al-rich compared to those observed in the Bushveld. Therefore, the composition used

in the pressure reduction thermodynamic model can be rejected as a possible parent magma to the UCZ.

- The MELTS thermodynamic modelling software accurately reproduces the experimental chromite compositions of this study. However, MELTS predicts that the CCCS decreases with increasing pressure, in contrast to the results of this study. Additionally, MELTS does not include Cr in the model for orthopyroxene. This is important at mid-to-low crustal pressures in which $D_{Cr(opx/liq)}$ increases, allowing orthopyroxene to consume a significant amount of Cr from the melt. Therefore, MELTS should be used with caution when modelling the behaviour of Cr in an orthopyroxene-saturated system.
- Reduction of pressure upon magma ascent favours chromite crystallization due to the decrease of $D_{Cr(opx/liq)}$, increasing the amount of Cr in melt available for chromite crystallization and because the CCCS remains approximately constant while silicate crystallization temperatures decrease. Although the MELTS thermodynamic model, described in Latypov *et al*. (2018), predicts a similar result, the evaluation of MELTS in this study shows that this outcome is achieved by a different mechanism.
- If a B1 magma ascends crystal-free, with the commonly proposed Cr content of 1000 μg/g, it would only produce chromitites on the millimetre scale at low pressure. For a reasonable interval of chromite-alone crystallization to occur in the B1 magma at the proposed depth of emplacement, a magma with a considerably higher Cr content is needed. Therefore, to produce the chromitites observed in the CZ by pressure reduction, significant volumes of unusually Cr-enriched magma would be required. This process would also require accumulation of crystallizing chromite to be highly

effective to yield a chromite layer during the short interval of chromite-alone crystallization. Additionally, the substantial volume of residual magma, that significantly exceeds the volume of the CZ, would have been removed from the system, which seems geologically unreasonable.

Future work should investigate trace element systematics of chromite that are sensitive to chromite-alone crystallization (i.e., Ga and V; Brenan *et al*. 2022) for chromite produced in the Bushveld Complex. This would provide insight into the role of chromite-alone crystallization, which is employed in the pressure reduction model as well as many other hypotheses, in the formation of Bushveld chromitites.

REFERENCES

Asimow, P.D., Hirschmann, M.M., Ghiorso, M.S., O'Hara, M.J., and Stolper, E.M. 1995. The effect of pressure-induced solid-solid phase transitions on decompression melting of the mantle. Geochimica et Cosmochimica Acta, **59**: 4489–4506.

Baker, D.R. 2004. Piston-cylinder calibration at 400 to 500 MPa: A comparison of using water solubility in albite melt and NaCl melting. American Mineralogist, **89**: 1553–1556.

Barnes, S.J. 1986a. The distribution of chromium among orthopyroxene, spinel and silicate liquid at atmospheric pressure. Geochimica et Cosmochimica Acta, **50**: 1889–1909.

Barnes, S.J. 1986b. The effect of trapped liquid crystallization on cumulus mineral compositions in layered intrusions. Contributions to Mineralogy and Petrology, **93**: 524–531.

Barnes, S.J. 1998. Chromite in Komatiites, 1. Magmatic Controls on Crystallization and Composition Distribution of Chromium and Chromite in Komatiites Introduction Petrographic features of chromite in. Journal of Petrology, **39**: 1689–1720.

Barnes, S.J., Maier, W.D., and Curl, E.A. 2010. Composition of the marginal rocks and sills of the rustenburg layered suite, Bushveld Complex, South Africa: Implications for the formation of the platinum-group element deposits. Economic Geology, **105**: 1491–1511.

Barnes, S.J., Mansur, E.T., and Pagé, P. 2022. Differences in composition of chromites from low-Ti and high-Ti picrites of the Emeishan Large Igneous Province and comparison with chromites of the UG-2 platinum-deposit of the Bushveld complex. Lithos, **412**–**413:**106613.

Barnes, S.J., and Roeder, P.L. 2001. The range of spinel compositions in terrestrial mafic and ultramafic rocks. Journal of Petrology, **42**: 2279–2302.

Bédard, J.H. 2007. Trace element partitioning coefficients between silicate melts and orthopyroxene: Parameterizations of D variations. Chemical Geology, **244**: 263–303.

Bertka, C.M., and Holloway, J.R. 1993. Pigeonite at solidus temperatures: implications for partial melting. Journal of Geophysical Research, **98:** 19755-19766.

Bilenker, L.D., Vantongeren, J.A., Lundstrom, C.C., and Simon, A.C. 2017. Iron isotopic evolution during fractional crystallization of the uppermost Bushveld Complex layered mafic intrusion. Geochemistry, Geophysics, Geosystems, **18**: 956–972.

Bohlen, S. 1984. Equilibria for precise pressure calibration and a frictionless furnace assembly for the piston-cylinder apparatus. Neues Jahrbuch für Mineralogie Monatshefte, **9**: 404–412.

Borisov, A., and Palme, H. 2000. Solubilities of noble metals in Fe-containing silicate melts as derived from experiments in Fe-free systems. American Mineralogist, **85**: 1665–1673.

Boudreau, A. E. 1992. Volatile fluid overpressure in layered intrusions and the formation of potholes. Australian Journal of Earth Sciences, **39**: 277–287.

Boudreau, A. E. 2002. The Stillwater and Bushveld magmas were wet! Extended Abstracts, 9th International Platinum Symposium, 2002 Billings: 57-60.

Boyd, F. R., and England, J. L. 1960. Apparatus for phase-equilibrium measurements at pressures up to 50 kilobars and temperatures up to 1750°C. Journal of Geophysical Research, **65**: 741-748.

Brenan, J.M., Finnigan, C.F., McDonough, W.F., and Homolova, V. 2012. Experimental constraints on the partitioning of Ru, Rh, Ir, Pt and Pd between chromite and silicate melt: The importance of ferric iron. Chemical Geology, **302**–**303**: 16–32.

Brenan, J.M., Woods, K., Mungall, J.E., and Weston, R. 2022. Origin of chromitites in the Esker Intrusive Complex, Ring of Fire Intrusive Suite, as revealed by chromite trace element chemistry and simple crystallization models. Targeted Geoscience Initiative 5: grant program final reports (2018-2020), Geological Survey of Canada, Open File 8755, 1–19.

Cameron, E.N. 1977. Chromite in the central sector of the Eastern Bushveld Complex, South Africa. American Mineralogist, **62**: 1082–1096.

Cameron, E.N., and Desborough, G.A. 1969. Occurrence and characteristics of chromite deposits, eastern Bushveld Complex. Economic Geology Monographs, **4:** 23–40.

Canil, D. 2002. Vanadium in peridotites, mantle redox and tectonic environments: Archean to present. Earth and Planetary Science Letters, **195**: 75–90.

Cawthorn, R.G. 2007. Cr and Sr: Keys to parental magmas and processes in the Bushveld Complex, South Africa. Lithos, **95**: 381–398.

Cawthorn, R.G. 2015. The Bushveld Complex, South Africa. *In* Layered In. *Edited By* B. Charlier, O. Namur, R. Latypov, and C. Tegner. Springer Geology, Dordrecht. 517-588.

Cawthorn, R.G., and Biggar, G.M. 1993. Crystallization of titaniferous chromite, magnesian ilmenite and armalcolite in tholeiitic suites in the Karoo Igneous Province. Contributions to Mineralogy and Petrology, **114**: 221–235.

Cawthorn, R.G., and Davies, G. 1983. Experimental data at 3 kbars pressure on parental magma to the Bushveld Complex. Contributions to Mineralogy and Petrology, **83**: 128–135.

Cawthorn, R.G., and Walraven, F. 1998. Emplacement and crystallization time for the Bushveld Complex. Journal of Petrology, **39**: 1669–1687.

Clarke, B., Uken, R., and Reinhardt, J. 2009. Structural and compositional constraints on the emplacement of the Bushveld Complex, South Africa. Lithos, **111**: 21–36.

Cole, J., Finn, C.A., and Webb, S.J. 2021. Geometry of the Bushveld Complex from 3D potential field modelling. Precambrian Research, **359**: 106219.

Curl, E.A. 2001. Parental magmas of the Bushveld Complex, South Africa: Unpublished Ph.D. thesis, Clayton, Victoria, Australia, Monash University, 140.

Davies, G., Cawthorn, R.G., Barton Jr, J.M., and Morton, M. 1980. Parental Magma to the Bushveld Complex. Nature, **287**: 33–35.

Dick, H.J.B., and Bullen, T. 1984. Chromian Spinel as a Petrogenetic Indicator in Abyssal and Alpine-Type Peridotites and Spatially Associated Lavas. Contributions to Mineralogy and Petrology, **86:** 54-76.

Eales, H. V. 2000. Implications of the chromium budget of the Western Limb of the Bushveld Complex. South African Journal of Geology, **103**: 141–150.

Eales, H.V., and Cawthorn, R.G. 1996. The Bushveld Complex. In: Cawthorn RG (ed) Layered intrusions. Elsevier, Amsterdam, 181–229.

Eales, H. V., and Costin, G. 2012. Crustally contaminated komatiite: Primary source of the chromitites and marginal, Lower, and Critical zone magmas in a staging chamber beneath the Bushveld Complex. Economic Geology, **107**: 645–665.

Ford, C.E., Biggar, G.M., Humphries, D.J., Wilson, G., Dixon, D., and O'Hara, M.J. 1972. Role of water in the evolution of the lunar crust; an experimental study of samples 14310; an indication of lunar calc-alkaline volcanism. Proceedings of the Third Lunar Science Conference, **1**: 207-229.

Forien, M., Tremblay, J., Barnes, S.J., Burgisser, A., and Pagé, P. 2015. The role of viscous particle segregation in forming chromite layers from slumped crystal slurries: Insights from analogue experiments. Journal of Petrology, **56**: 2425–2444.

Ghiorso, M.S., and Sack, R.O. 1995. Chemical Mass-Transfer in Magmatic Processes IV. A Revised and Internally Consistent Thermodynamic Model for the Interpolation and Extrapolation of Liquid-Solid Equilibria in Magmatic Systems at Elevated-Temperatures and Pressures. Contributions to Mineralogy and Petrology, **119:** 197-212.

Godel, B., Barnes, S.J., and Maier, W.D. 2011. Parental magma composition inferred from trace element in cumulus and intercumulus silicate minerals: An example from the Lower and Lower Critical Zones of the Bushveld Complex, South-Africa. Lithos, **125**: 537–552.

Haggerty, Stephen E. 1976. Chapter 8: Opaque mineral oxides in terrestrial igneous rocks. Oxide Minerals, edited by Douglas Rumble. De Gruyter. 303-502.

Harmer, R.E., and Sharpe, M.R. 1985. Field relation and strontium isotope systematics of the marginal rocks of the eastern Bushveld Complex. Economic Geology, **80**: 813-837.

Hatton, C.J. 1995. Magma plume origin for the Bushveld and Ventersdrop magmatic provinces. Journal of African Earth Sciences, **21**: 571-577.

Hirschmann, M.M. 2021. Iron-wüstite revisited: A revised calibration accounting for variable stoichiometry and the effects of pressure. Geochimica et Cosmochimica Acta, **313**: 74–84.

Holland, T.J.B., and Powell, R. 1990. An enlarged and updated internally consistent thermodynamic dataset with uncertainties and correlations: the system K2O–Na2O–CaO–MgO–MnO–FeO–Fe2O3–Al2O3–TiO2–SiO2–C–H2–O2. Journal of Metamorphic Geology, **8**: 89–124.

Holzheid, A., Palme, H., and Chakraborty, S. 1997. The activities of NiO, CoO and FeO in silicate melts. Chemical Geology, **139**: 21–38.

Irvine, T.N. 1975. Crystallization sequences in the Muskox intrusion and other layered intrusions-II. Origin of chromitite layers and similar deposits of other magmatic ores. Geochimica et Cosmochimica Acta, **39**.

Irvine, T.N. 1977. Origin of chromitite layers in the Muskox intrusion and other stratiform intrusions: A new interpretation. Geology, **5**: 273–277.

Jensen, L.S. 1976. A New Cation Plot for Classifying Subalkalic Volcanic Rocks. Ontario Div. Mines, **MP 66**: 22.

Jochum, K.P., Weis, U., Stoll, B., Kuzmin, D., Yang, Q., Raczek, I., Jacob, D.E., Stracke, A., Birbaum, K., Frick, D.A., Günther, D., and Enzweiler, J. 2011. Determination of reference values for NIST SRM 610-617 glasses following ISO guidelines. Geostandards and Geoanalytical Research, **35**: 397–429.

Jochum, K.P., Weis, U., Schwager, B., Stoll, B., Wilson, S.A., Haug, G.H., Andreae, M.O., and Enzweiler, J. 2016. Reference Values Following ISO Guidelines for Frequently Requested Rock Reference Materials. Geostandards and Geoanalytical Research, **40**: 333–350.

Kress, V.C., and Carmichael, I.S.E. 1991. The compressibility of silicate liquids containing Fe2O3 and the effect of composition, temperature, oxygen fugacity and pressure on their redox states. Contributions to Mineralogy and Petrology, **108**: 82–92.

Kruger, F.J. 1994. The Sr-isotopic stratigraphy of the western Bushveld Complex. South African Journal of Geology, **97**: 393–398.

Kruger, F.J. 2005. Filling the Bushveld Complex magma chamber: Lateral expansion, roof and floor interaction, magmatic unconformities, and the formation of giant chromitite, PGE and Ti-V-magnetitite deposits. Mineralium Deposita, **40**: 451–472.

Langa, M.M., Jugo, P.J., Leybourne, M.I., Grobler, D.F., Adetunji, J., and Skogby, H. 2021. Chromite chemistry of a massive chromitite seam in the northern limb of the Bushveld Igneous Complex, South Africa: correlation with the UG-2 in the eastern and western limbs and evidence of variable assimilation of footwall rocks. Mineralium Deposita, **56**: 31–44.

Latypov, R., and Chistyakova, S. 2022. Misinterpretation of zircon ages in layered intrusions. South African Journal of Geology, **125**: 1–14.

Latypov, R., Chistyakova, S., Barnes, S.J., Godel, B., Delaney, G.W., Cleary, P.W., Radermacher, V.J., Campbell, I., and Jakata, K. 2022. Chromitite layers indicate the existence of large, long-lived, and entirely molten magma chambers. Scientific Reports, **12**: 1–15.

Latypov, R., Chistyakova, S., and Mukherjee, R. 2017. A novel hypothesis for origin of massive chromitites in the Bushveld igneous Complex. Journal of Petrology, **58**: 1899–1940.

Latypov, R., Costin, G., Chistyakova, S., Hunt, E.J., Mukherjee, R., and Naldrett, T. 2018. Platinum-bearing chromite layers are caused by pressure reduction during magma ascent. Nature Communications, **9**: 1–7.

Lesher, C.E., and Spera, F.J. 2015. Thermodynamic and transport properties of silicate melts and magma. *In:* The Encyclopedia of Volcanoes. *Edited By* H Sigurdsso. Academic Press. **2:** 113–141.

Lipin, B.R. 1993. Pressure increases, the formation of chromite seams, and the development of the ultramafic series in the stillwater complex, Montana. Journal of Petrology, **34**: 955–976.

Longhi, J., Auwera, J. V., and Fram, M.S. 1992. Pressure effects, kinetics, and rheology of anorthositic and related magmas. American Mineralogist, **78**: 1016–1030.

Magee, C., Stevenson, C.T.E., and Ebmeier, S.K. 2018. Magma plumbing systems: a geophysical perspective. Journal of Petrology, **59**: 1217–1251.

Maier, W.D., Barnes, S.J., and Groves, D.I. 2013. The Bushveld Complex, South Africa: Formation of platinum-palladium, chrome- and vanadium-rich layers via hydrodynamic sorting of a mobilized cumulate slurry in a large, relatively slowly cooling, subsiding magma chamber. Mineralium Deposita, **48**: 1–56.

Maier, W.D., Barnes, S.J., and Karykowski, B.T. 2016. A chilled margin of komatiite and Mg-rich basaltic andesite in the western Bushveld Complex, South Africa. Contributions to Mineralogy and Petrology, **171**: 1–22.

Médard, E., McCammon, C.A., Barr, J.A., and Grove, T.L. 2008. Oxygen fugacity, temperature reproducibility, and H 2 O contents of nominally anhydrous piston-cylinder experiments using graphite capsules. American Mineralogist, **93**: 1838–1844.

Mondal, S.K., and Mathez, E.A. 2007. Origin of the UG2 chromitite layer, Bushveld Complex. Journal of Petrology, **48**: 495–510.

Morimoto, N., Fabries, J., Ferguson, A.K., Ginzburg, I.V., Ross, M., Seifert, F.A., Zussman, J., Aoki, K., and Gottardi, G. 1988. Nomenclature of pyroxenes Subcommittee on Pyroxenes Commission on New Minerals and Mineral Names International Mineralogical Association. American Mineralogist, **73**: 1123–1133.

Mungall, J.E. 2015. Physical Controls of Nucleation, Growth and Migration of Vapor Bubbles in Partially Molten Cumulates. *In* Layered Intrusions. *Edited By* B. Charlier, O. Namur, R. Latypov, and C. Tegner. Springer Geology, Dordrecht. 331-378.

Mungall, J., and Brenan, J. 2014. Partitioning of platinum-group elements and Au between sulfide liquid and basalt and the origins of mantle-crust fractionation of the chalcophile elements. Geochimica et Cosmochimica Acta, **125**: 265–289.

Mungall, J.E., Kamo, S.L., and Mcquade, S. 2016. U-Pb geochronology documents out-of-sequence emplacement of ultramafic layers in the Bushveld Igneous Complex of South Africa. Nature Communications, **7**: 1–13.

Murck, B.W., and Campbell, I.H. 1986. The effects of temperature, oxygen fugacity and melt composition on the behaviour of chromium in basic and ultrabasic melts. Geochimica et Cosmochimica Acta, **50**: 1871–1887.

Naldrett, A.J., Kinnaird, J., Wilson, A., Yudovskaya, M., McQuade, S., Chunnett, G., and Stanley, C. 2009. Chromite composition and PGE content of Bushveld chromitites: Part 1 - The Lower and Middle Groups. Applied Earth Science; Institutions of Mining and Metallurgy, Section B. **118:** 131-161.

Naldrett, A.J., Wilson, A., Kinnaird, J., Yudovskaya, M., and Chunnett, G. 2012. The origin of chromitites and related PGE mineralization in the Bushveld Complex: New mineralogical and petrological constraints. Mineralium Deposita, **47**: 209–232.

Natural Resources Canada (NRCan) 2019. Targeted Geoscience Initiative – increasing deep exploration effectiveness with next-generation science and innovation. General Information Product, **120e**: 1-15.

Nicholson, D.M., and Mathez, E.A. 1991. Petrogenesis of the Merensky Reef in the Rustenburg section of the Bushveld Complex. Contributions to Mineralogy and Petrology, **107**: 293–309.

Nikolaev, G.S., Ariskin, A.A., and Barmina, G.S. 2018. SPINMELT-2.0: Simulation of Spinel–Melt Equilibrium in Basaltic Systems under Pressures up to 15 Kbar: II. Description of the Program Package, the Topology of the Cr-spinel–Melt Model System, and Petrological Implications. Geochemistry International, **56**: 125–135.

Olsson, J.R., Soderlund, U., Hamilton, M.A., Klausen, M.B., and Helffrich. G.R. 2011. A late Archaean radiating dyke swarm as possible clue to the origin of the Bushveld Complex. Nature Geoscience, **4**: 865-869.

O'Neill, H. St. C. 1987. Quartz-fayalite-iron and quartz-fayalite-magnetite equilibria and the free energy of formation of fayalite (Fe2SiO4) and magnetite (Fe3O4). American Mineralogist, **72**: 67–75.

Papike, J.J., Simon, S.B., Burger, P. V., Bell, A.S., Shearer, C.K., and Karner, J.M. 2016. Chromium, vanadium, and titanium valence systematics in Solar System pyroxene as a recorder of oxygen fugacity, planetary provenance, and processes. American Mineralogist, **101**: 907–918.

Putirka, K.D. 2008. Thermometers and barometers for volcanic systems. Reviews in Mineralogy and Geochemistry, **69**: 61–120.

Rhodes, J.M., Dungan, M.A., Blanchard, D.P., and Long, P.E. 1979. Magma mixing at mid-ocean ridges: evidence form basalts drilled near 22 N on the mid-Atlantic ridge. Tectonophysics, **55:** 35-61.

Robb, S.J., and Mungall, J.E. 2020. Testing emplacement models for the Rustenburg Layered Suite of the Bushveld Complex with numerical heat flow models and plagioclase geospeedometry. Earth and Planetary Science Letters, **534**: 116084.

Roeder, P.L., and Reynolds, I. 1991. Crystallization of chromite and chromium solubility in basaltic melts. Journal of Petrology, **32**: 909–934.

Schulte, R.F., Taylor, R.D., Piatak, N.M., and Seal ll, R.R. 2012. Stratiform chromite deposit model, chap. E of Mineral deposit models for resource assessment. U.S. Geological Survey Scientific Investigations Report 2010–5070-E, **5070**: 131.

Sen, G., and Presnall, D.C. 1984. Liquidus phase relationships on the join anorthite-forsterite-quartz at 10 kbar with applications to basalt petrogenesis. Contributions to Mineralogy and Petrology, **85**: 404–408.

Sharpe, M.R. 1981. The chronology of magma influxes to the eastern compartment of the Bushveld Complex as exemplified by its marginal border groups. Journal of the Geological Society, **138:** 307–326.

Sharpe, M.R., and Irvine, T.N. 1983. Melting Relations of Two Bushveld Chilled Margin Rocks and Implications for the Origin of Chromitite. Carnegie Institution Geophysical Laboratory Yearbook, **82**: 295–300.

Silver, P.G., Fouch, M.J., Gao, S.S., and Schmitz, M. 2004. Seismic anisotropy, mantle fabric, and the magmatic evolution of Precambrian southern Africa. South African Journal of Geology, **107**: 45–58.

Sisson, T.W., and Grove, T.L. 1993. Experimental investigations of the role of H2O in calc-alkaline differentiation and subduction zone magmatism. Contributions to Mineralogy and Petrology, **113**: 143–166.

Smith, P. M., and Asimow, P. D. 2005. Adiabat_1ph: A new public front-end to the MELTS, pMELTS, and pHMELTS models. Geochemistry Geophysics Geosystems, **6:** 1-8.

Smith, W.D., and Maier, W.D. 2021. The geotectonic setting, age and mineral deposit inventory of global layered intrusions. Earth-Science Reviews, **220**: 103736.

Stamper, C.C., Melekhova, E., Blundy, J.D., Arculus, R.J., Humphreys, M.C.S., and Brooker, R.A. 2014. Oxidised phase relations of a primitive basalt from Grenada, Lesser Antilles. Contributions to Mineralogy and Petrology, **167**: 1–20.

Stevens, R.E. 1944. Compositions of some chromites of the Western Hemisphere. American Mineralogist, **29**: 1–34.

Stowe, C.W. 1994. Compositions and tectonic settings of chromite deposits through time. Economic Geology, **89**: 528–546.

Taylor, J.R., Wall, V.J., and Pownceby, M.I. 1992. The calibration and application of accurate redox sensors. American Mineralogist, **77**: 284–295.

Toplis, M.J., and Corgne, A. 2002. An experimental study of element partitioning between magnetite, clinopyroxene and iron-bearing silicate liquids with particular emphasis on vanadium. Contributions to Mineralogy and Petrology, **144:** 22-37.

Ulmer, P., and Luth, R. W. 1991. The graphite-COH fluid equilibrium in P, T, fO2 space. Contributions to Mineralogy and Petrology, **106**: 265-272.

U.S. Geological Survey (USGS), 2019. Mineral Commodity Summaries 2019. U.S. Geological Survey, 200.

Vander Auwera, J., Longhi, J., and Duchesne, J.C. 2000. The effect of pressure on D(Sr) (plag/melt) and D(Cr) (opx/melt): Implications for anorthosite petrogenesis. Earth and Planetary Science Letters, **178**: 303–314.

VanTongeren, J.A., and Mathez, E.A. 2012. Large-scale liquid immiscibility at the top of the Bushveld Complex, South Africa. Geology, **40**: 491–494.

Veksler, I. V., and Hou, T. 2020. Experimental study on the effects of H2O upon crystallization in the Lower and Critical Zones of the Bushveld Complex with an emphasis on chromitite formation. Contributions to Mineralogy and Petrology, **175**.

Von Gruenewaldt, G., Sharpe, M.R., and Hatton, C.J. 1985. The Bushveld complex: introduction and review. Economic Geology, **80**: 803–812.

Von Gruenewaldt, G., and Worst, B. G. 1986. Chromite deposits at Zwartkop chrome mine, western Bushveld Complex. In *Mineral deposits of Southern Africa*. 1217-1227.

Wager, L.R., and Brown, G.M. 1968. Layered Igneous Intrusions. Edinburgh London Oliver Boyd, 1–588.

Wallmach, T., Hatton, C.J., and Droop, G.T. 1989. Extreme facies of contact metamorphism developed in calc-silicate xenoliths in the eastern Bushveld Complex. The Canadian Mineralogist, **27**: 509–523.

Walraven, F., Armstrong, R., and Kruger, F.J. 1990. A chronostratigraphic framework for the north-central Kaapvaal Craton, the Bushveld Complex and the Vredefort Structure. Tectonophysics **171**: 23-48.

Waters, D.J., and Lovegrove, D.P. 2002. Assessing the extent of disequilibrium and overstepping of prograde metamorphic reactions in metapelites from the Bushveld Complex aureole, South Africa. Journal of Metamorphic Geology, **20:** 135-149.

Watson, E., Wark, D., Price, J., and Van Orman, J. 2002. Mapping the thermal structure of solid-media pressure assemblies. Contributions to Mineralogy and Petrology, **142**: 640–652.

Wilson, A.H. 2012. A chill sequence to the bushveld complex: Insight into the first stage of emplacement and implications for the parental magmas. Journal of Petrology, **53**: 1123–1168.

Yao, Z., Mungall, J.E., and Jenkins, M.C. 2021. The Rustenburg Layered Suite formed as a stack of mush with transient magma chambers. Nature Communications, **12**.

Zeh, A., Ovtcharova, M., Wilson, A.H., and Schaltegger, U. 2015. The Bushveld Complex was emplaced and cooled in less than one million years - results of zirconology, and geotectonic implications. Earth and Planetary Science Letters, **418**: 103–114.

Zientek, M.L., Causey, J.D., Parks, H.L., and Miller, R.J. 2014. Platinum-group elements in southern Africa—Mineral inventory and an assessment of undiscovered mineral resources. U.S. Geological Survey Scientific Investigations Report 2010–5090–Q, 126.

Table 2.1. Summary of run conditions and major and trace element compositions of starting materials and run-product glasses.

Sample	Series	#	T (°C)	P (GPa)	Δ FMQ	t (h)	SM[2]	Capsule[3]	K_2O	CaO	TiO_2	Na_2O	MgO	Al_2O_3	FeO_T	MnO	SiO_2	P_2O_5	Cr (μg/g)	Total
Lat_SM_3	-	-	-	-	-	-	-	-	0.13	9.91	0.11	1.42	5.81	17.37	8.71	0.00	55.60	0.00	681	99.16
									0.02	*0.09*	*0.03*	*0.04*	*0.06*	*0.16*	*0.11*	*0.00*	*0.21*	*0.00*	*32*	*0.07*
B1_SM_3	-	-	-	-	-	-	-	-	0.98	6.70	0.33	1.66	11.17	11.73	9.69	0.18	56.78	0.09	859	99.43
									0.03	*0.06*	*0.04*	*0.04*	*0.07*	*0.10*	*0.11*	*0.03*	*0.19*	*0.03*	*3*	*0.05*
Lat_1.5	1.0	1300	0.0001	-0.02	48	a	Fe-Ir loop		0.14	9.73	0.11	1.57	5.87	17.80	8.82	0.00	56.33	0.01	784	100.46
n=15				*0.01*					*0.02*	*0.12*	*0.03*	*0.04*	*0.07*	*0.13*	*0.14*	*0.03*	*0.23*	*0.03*	*15*	*0.07*
B1_1.5	1.0	1300	0.0001	-0.02	48	a	Fe-Ir loop		0.90	6.66	0.34	1.64	11.21	12.07	9.93	0.19	57.52	0.06	920	100.64
n=15				*0.01*					*0.03*	*0.11*	*0.02*	*0.03*	*0.07*	*0.09*	*0.09*	*0.03*	*0.17*	*0.03*	*3*	*0.05*
Lat_1.3	1.0	1280	0.0001	0.10	24	a	Fe-Ir loop		0.13	9.68	0.10	1.61	5.86	17.78	8.87	0.01	56.59	0.00	602	100.71
n=15				*0.02*					*0.02*	*0.14*	*0.04*	*0.05*	*0.07*	*0.15*	*0.12*	*0.02*	*0.27*	*0.03*	*8*	*0.08*
B1_1.3	1.0	1280	0.0001	0.10	24	a	Fe-Ir loop		0.94	6.64	0.33	1.80	10.96	12.16	9.82	0.19	57.67	0.05	746	100.65
n=15				*0.02*					*0.04*	*0.07*	*0.05*	*0.04*	*0.10*	*0.12*	*0.09*	*0.03*	*0.34*	*0.04*	*6*	*0.09*
Lat_1.10	1.0	1280	0.0001	-0.14	48	a	Fe-Ir loop		0.12	10.16	0.01	1.60	5.57	17.69	8.90	0.01	56.32	0.02	602	100.50
n=15				*0.01*					*0.01*	*0.06*	*0.01*	*0.05*	*0.07*	*0.10*	*0.06*	*0.01*	*0.45*	*0.02*	*8*	*0.13*
B1_1.10	1.0	1280	0.0001	-0.14	48	a	Fe-Ir loop		1.00	6.93	0.25	1.72	10.64	11.96	9.87	0.18	56.94	0.07	752	99.68
n=15				*0.01*					*0.02*	*0.03*	*0.03*	*0.06*	*0.14*	*0.08*	*0.05*	*0.02*	*0.28*	*0.02*	*5*	*0.08*
Lat_2.3[1]	2.0	1280	0.0001	-0.16	24	a	Fe-Ir loop		0.13	9.75	0.10	1.57	5.71	17.21	8.57	-0.01	55.80	0.00	561	100.33
n=14				*0.01*					*0.02*	*0.12*	*0.03*	*0.05*	*0.09*	*0.11*	*0.17*	*0.02*	*0.33*	*0.00*	*7*	*0.09*
B1_2.3[1]	2.0	1280	0.0001	-0.16	24	a	Fe-Ir loop		0.95	6.72	0.24	1.75	10.59	12.02	9.82	0.18	57.72	0.06	677	100.15
n=15				*0.01*					*0.02*	*0.07*	*0.02*	*0.07*	*0.12*	*0.10*	*0.09*	*0.02*	*0.15*	*0.02*	*9*	*0.07*
Lat_2.4[1]	2.0	1280	0.0001	-0.15	12	a	Fe-Ir loop		0.13	9.83	0.11	1.54	5.82	17.45	8.83	0.01	56.63	0.00	581	98.92
n=15				*0.01*					*0.02*	*0.11*	*0.03*	*0.04*	*0.04*	*0.15*	*0.07*	*0.02*	*0.23*	*0.05*	*6*	*0.10*
B1_2.4[1]	2.0	1280	0.0001	-0.15	12	a	Fe-Ir loop		0.95	6.70	0.35	1.75	10.90	11.92	9.81	0.18	57.50	0.07	711	100.14
n=15				*0.01*					*0.03*	*0.07*	*0.03*	*0.03*	*0.08*	*0.11*	*0.11*	*0.02*	*0.24*	*0.06*	*8*	*0.05*
Lat_5.1	5.0	1280	0.0001	-0.40	48	d	Fe-Ir loop		0.15	9.43	0.10	1.47	6.43	16.62	8.91	0.01	57.11	0.00	717	100.43
n=21				*0.00*					*0.02*	*0.11*	*0.03*	*0.04*	*0.07*	*0.15*	*0.16*	*0.02*	*0.29*	*0.03*	*8*	*0.07*
B1_5.1	5.0	1280	0.0001	-0.40	48	d	Fe-Ir loop		0.74	6.43	0.32	1.37	10.79	11.20	9.97	0.19	59.01	0.02	878	100.22
n=20				*0.00*					*0.03*	*0.09*	*0.04*	*0.05*	*0.13*	*0.10*	*0.21*	*0.03*	*0.18*	*0.04*	*28*	*0.06*
Lat_1.6	1.0	1260	0.0001	0.02	48	a	Fe-Ir loop		0.14	9.84	0.10	1.61	5.85	17.69	8.83	0.01	56.22	0.02	540	100.38
n=15				*0.05*					*0.02*	*0.11*	*0.02*	*0.03*	*0.06*	*0.08*	*0.10*	*0.02*	*0.19*	*0.03*	*5*	*0.05*

Sample	Series #	T (°C)	P (GPa)	Δ FMQ	t (h)	SM[2]	Capsule[3]	K_2O	CaO	TiO_2	Na_2O	MgO	Al_2O_3	FeO_T	MnO	SiO_2	P_2O_5	Cr (μg/g)	Total
B1_1.6	1.0	1260	0.0001	0.02	48	a	Fe-Ir loop	0.97	7.20	0.37	1.88	9.77	12.74	9.87	0.19	57.25	0.06	620	100.39
n=15				*0.05*				*0.03*	*0.16*	*0.05*	*0.05*	*0.19*	*0.12*	*0.15*	*0.03*	*0.37*	*0.04*	*18*	*0.11*
Lat_1.9	1.0	1230	0.0001	0.04	48	a	Fe-Ir loop	0.12	9.78	0.01	1.56	5.65	17.33	8.86	0.01	56.95	0.01	397	100.34
n=15				*0.04*				*0.01*	*0.08*	*0.01*	*0.05*	*0.11*	*0.10*	*0.14*	*0.01*	*0.31*	*0.02*	*5*	*0.09*
B1_1.9	1.0	1230	0.0001	0.04	48	a	Fe-Ir loop	1.11	7.52	0.28	1.99	7.67	13.56	9.67	0.17	57.88	0.08	431	100.00
n=15				*0.04*				*0.05*	*0.14*	*0.03*	*0.11*	*0.22*	*0.10*	*0.19*	*0.02*	*0.56*	*0.02*	*18*	*0.16*
Lat_1.11	1.0	1230	0.0001	0.05	96	a	Fe-Ir loop	0.15	9.75	0.11	1.58	5.77	17.46	8.67	0.00	56.63	0.03	366	100.16
n=15				*0.00*				*0.01*	*0.11*	*0.03*	*0.04*	*0.07*	*0.11*	*0.12*	*0.02*	*0.19*	*0.04*	*4*	*0.06*
B1_1.11	1.0	1230	0.0001	0.05	96	a	Fe-Ir loop	1.09	7.30	0.38	1.94	8.39	13.03	9.66	0.19	57.94	0.05	389	100.03
n=15				*0.00*				*0.03*	*0.06*	*0.03*	*0.05*	*0.08*	*0.10*	*0.11*	*0.03*	*0.32*	*0.04*	*4*	*0.08*
Lat_5.2	5.0	1230	0.0001	-0.38	48	d	Fe-Ir loop	0.15	9.37	0.10	1.72	6.42	16.58	8.79	0.01	57.08	0.02	409	100.30
n=20				*0.03*				*0.02*	*0.12*	*0.04*	*0.06*	*0.06*	*0.13*	*0.12*	*0.02*	*0.32*	*0.03*	*6*	*0.09*
B1_5.2	5.0	1230	0.0001	-0.38	48	d	Fe-Ir loop	0.85	7.42	0.35	1.81	7.57	12.38	9.88	0.18	59.05	0.05	447	99.61
n=19				*0.03*				*0.04*	*0.16*	*0.03*	*0.06*	*0.28*	*0.17*	*0.25*	*0.02*	*0.36*	*0.03*	*15*	*0.12*
Lat_1.7	1.0	1200	0.0001	-0.03	48	a	Fe-Ir loop	0.14	9.22	0.11	1.56	6.14	16.22	9.34	0.00	57.27	0.00	323	100.05
n=15				*0.10*				*0.02*	*0.11*	*0.03*	*0.04*	*0.10*	*0.11*	*0.19*	*0.02*	*0.33*	*0.03*	*17*	*0.10*
B1_1.7	1.0	1200	0.0001	-0.03	48	a	Fe-Ir loop	1.09	8.06	0.40	2.16	6.70	13.91	9.83	0.18	57.50	0.10	326	99.98
n=15				*0.10*				*0.04*	*0.13*	*0.03*	*0.08*	*0.21*	*0.14*	*0.18*	*0.03*	*0.29*	*0.04*	*27*	*0.09*
Lat_2.2[1]	2.0	1200	0.0001	-0.20	48	a	Fe-Ir loop	0.12	9.31	0.01	1.48	6.05	16.52	9.38	0.01	57.10	0.01	239	100.02
n=15				*0.01*				*0.01*	*0.08*	*0.01*	*0.07*	*0.13*	*0.18*	*0.18*	*0.01*	*0.32*	*0.01*	*27*	*0.10*
B1_2.2[1]	2.0	1200	0.0001	-0.20	48	a	Fe-Ir loop	1.11	7.71	0.30	2.08	7.29	13.96	9.69	0.17	57.60	0.10	259	100.05
n=14				*0.01*				*0.06*	*0.61*	*0.03*	*0.10*	*1.41*	*0.55*	*0.31*	*0.02*	*0.43*	*0.02*	*8*	*0.42*
Lat_1.8	1.0	1170	0.0001	0.00	30	a	Fe-Ir loop	0.15	8.75	0.13	1.50	6.42	14.94	10.45	0.00	57.27	0.01	252	99.65
n=15				*0.04*				*0.02*	*0.21*	*0.03*	*0.11*	*0.31*	*0.29*	*0.60*	*0.02*	*0.95*	*0.03*	*22*	*0.30*
B1_1.8	1.0	1170	0.0001	0.00	30	a	Fe-Ir loop	1.20	8.13	0.43	2.25	5.59	14.45	9.28	0.17	57.93	0.10	228	99.56
n=15				*0.04*				*0.13*	*0.42*	*0.04*	*0.09*	*0.23*	*0.15*	*0.63*	*0.02*	*1.00*	*0.03*	*13*	*0.31*
B1_4.10	4.0	1400	0.51	-2.15	4	h	Graphite	0.94	6.70	0.35	1.68	11.84	11.51	9.61	0.19	56.72	0.07	850[4]	99.72
n=19			*0.02*					*0.04*	*0.09*	*0.03*	*0.06*	*0.17*	*0.14*	*0.36*	*0.03*	*0.54*	*0.03*	*215*	*0.17*
B1_4.11	4.0	1370	0.51	-2.10	4	h	Graphite	0.96	6.62	0.34	1.68	11.60	11.68	9.68	0.19	57.18	0.04	862[4]	100.08
n=18			*0.02*					*0.03*	*0.08*	*0.03*	*0.04*	*0.12*	*0.11*	*0.14*	*0.03*	*0.23*	*0.04*	*203*	*0.06*
Lat_3.4	3.0	1280	0.51	-0.32	12	d	Graphite	0.16	9.61	0.10	1.46	6.41	17.15	7.56	0.00	57.52	0.00	747	100.08
n=14			*0.02*	*0.18*				*0.02*	*0.07*	*0.03*	*0.03*	*0.06*	*0.12*	*0.10*	*0.02*	*0.20*	*0.04*	*5*	*0.06*

Sample	Series #	T (°C)	P (GPa)	Δ FMQ	t (h)	SM[2]	Capsule[3]	K_2O	CaO	TiO_2	Na_2O	MgO	Al_2O_3	FeO_T	MnO	SiO_2	P_2O_5	Cr (μg/g)	Total
B1_3.4	3.0	1280	0.51	-0.51	12	d	Fe-Ir	1.19	7.67	0.38	1.99	6.78	13.82	7.95	0.18	59.46	0.11	801	99.64
n=15			*0.02*	*0.30*				*0.03*	*0.09*	*0.03*	*0.03*	*0.09*	*0.15*	*0.11*	*0.02*	*0.21*	*0.05*	*45*	*0.06*
Lat_4.12	4.0	1260	0.51	-1.92	4	h	Graphite	0.15	9.51	0.11	1.35	6.18	16.35	9.42	0.00	56.40	0.01	504[4]	99.55
n=19			*0.02*					*0.02*	*0.11*	*0.04*	*0.06*	*0.55*	*0.58*	*0.46*	*0.02*	*0.65*	*0.04*	*154*	*0.27*
Lat_3.5	3.0	1230	0.51	-0.24	12	d	Fe-Ir	0.25	9.13	0.15	1.65	4.23	14.47	8.98	0.01	60.27	0.01	374[4]	99.22
n=14			*0.02*	*0.14*				*0.02*	*0.12*	*0.03*	*0.07*	*0.14*	*0.14*	*0.21*	*0.02*	*0.39*	*0.05*	*147*	*0.11*
B1_3.5	3.0	1230	0.51	-0.34	12	d	Fe-Ir	1.15	7.43	0.41	2.33	5.38	14.45	7.63	0.14	60.58	0.03	413[4]	99.64
n=16			*0.02*	*0.16*				*0.09*	*0.36*	*0.05*	*0.18*	*1.62*	*0.95*	*0.32*	*0.03*	*0.59*	*0.03*	*160*	*0.50*
B1_4.5	4.0	1530	1.03	-2.16	12	h	Graphite	0.97	6.45	0.34	1.64	11.51	11.54	9.46	0.19	56.61	0.09	898[4]	98.92
n=14			*0.04*					*0.04*	*0.07*	*0.03*	*0.05*	*0.14*	*0.12*	*0.13*	*0.03*	*0.40*	*0.05*	*253*	*0.11*
B1_4.4	4.0	1500	1.03	-2.11	12	h	Graphite	0.99	6.61	0.34	1.72	11.00	11.85	9.60	0.19	56.63	0.07	1067[4]	99.16
n=15			*0.04*					*0.03*	*0.11*	*0.03*	*0.05*	*0.12*	*0.12*	*0.14*	*0.02*	*0.42*	*0.03*	*251*	*0.11*
Lat_4.6	4.0	1310	1.02	-1.79	12	h	Graphite	0.13	9.67	0.10	1.45	6.73	17.26	8.12	-0.02	56.24	0.00	660[4]	99.76
n=12			*0.02*					*0.01*	*0.14*	*0.03*	*0.06*	*0.12*	*0.15*	*0.19*	*0.03*	*0.48*	*0.04*	*175*	*0.14*
B1_4.6	4.0	1310	1.02	-1.79	12	h	Graphite	1.16	8.03	0.41	2.01	6.75	14.01	8.74	0.17	57.34	0.07	374[4]	98.75
n=15			*0.02*					*0.06*	*0.16*	*0.04*	*0.04*	*0.37*	*0.31*	*0.22*	*0.03*	*0.55*	*0.05*	*190*	*0.17*
B1_3.2	3.0	1280	1.02	-0.83	12	d	Fe-Ir	1.23	7.95	0.44	2.10	6.29	13.94	9.06	0.17	57.37	0.12	241	98.99
n=15			*0.02*	*0.13*				*0.05*	*0.08*	*0.04*	*0.04*	*0.08*	*0.07*	*0.05*	*0.03*	*0.16*	*0.04*	*7*	*0.08*
Lat_3.3	3.0	1280	1.02	-0.27	12	d	Fe-Ir	0.14	9.65	0.10	1.46	6.41	17.18	7.15	0.01	57.72	-0.02	718	99.95
n=13			*0.02*	*0.13*				*0.01*	*0.10*	*0.03*	*0.04*	*0.06*	*0.14*	*0.13*	*0.02*	*0.26*	*0.05*	*5*	*0.07*
B1_3.3	3.0	1280	1.02	-0.22	12	d	Fe-Ir	1.30	8.12	0.43	2.14	5.33	14.88	6.88	0.16	59.89	0.11	807	99.37
n=15			*0.02*	*0.13*				*0.04*	*0.11*	*0.04*	*0.05*	*0.11*	*0.17*	*0.11*	*0.02*	*0.30*	*0.06*	*49*	*0.08*
Lat_3.7	3.0	1280	1.02	-0.30	12	d	Fe-Ir	0.17	9.61	0.10	1.71	6.53	16.75	6.86	0.01	57.53	0.03	1057	99.44
n=20			*0.02*	*0.32*				*0.02*	*0.11*	*0.04*	*0.03*	*0.06*	*0.08*	*0.07*	*0.02*	*0.18*	*0.04*	*15*	*0.05*
B1_3.7	3.0	1280	1.02	-0.28	12	d	Fe-Ir	1.21	7.96	0.41	2.32	5.31	14.26	6.43	0.15	61.14	0.07	877	99.38
n=20			*0.02*	*0.18*				*0.03*	*0.12*	*0.04*	*0.04*	*0.05*	*0.22*	*0.09*	*0.02*	*0.24*	*0.05*	*8*	*0.08*

Sample	Series #	T (°C)	P (GPa)	Δ FMQ	t (h)	SM[2]	Capsule[3]	K_2O	CaO	TiO_2	Na_2O	MgO	Al_2O_3	FeO_T	MnO	SiO_2	P_2O_5	Cr (μg/g)	Total
Lat_3.8	3.0	1230	1.02	0.04	12	d	Fe-Ir	0.31	9.25	0.21	1.31	4.50	15.62	9.19	0.01	57.82	0.02	404[4]	98.30
n=20			*0.02*	*0.26*				*0.01*	*0.09*	*0.05*	*0.16*	*1.07*	*0.74*	*0.54*	*0.01*	*0.40*	*0.05*	*218*	*0.35*
B1_3.8	3.0	1230	1.02	-0.22	12	d	Fe-Ir	1.18	6.79	0.41	2.12	6.66	13.91	6.96	0.15	61.37	0.07	455[4]	99.90
n=19			*0.02*	*0.14*				*0.13*	*0.17*	*0.04*	*0.24*	*1.86*	*1.04*	*0.67*	*0.03*	*0.83*	*0.04*	*167*	*0.58*

All oxides values in are wt %, *n*= number of analyses and FeO_T indicates all Fe expressed as FeO. Italicized numbers indicate one standard deviation. Footnotes: 1. Melting experiments. 2. SM indicates the starting materials used for the experiment: a – anhydrous, h – hydrous, and d – chromite-doped and hydrous. 3. Capsule types: Experiments done at 0.1 MPa on wire loops and all other experiments (done at 0.5 and 1 GPa) in graphite-lined Pt or Fe-Ir alloy capsules. 4. Indicates that Cr (µg/g) measured on EPMA with a count time of 60 s for Cr.

Table 3.1. Summary of major element compositions of run-product pyroxenes.

Sample	T (°C)	P (GPa)	Δ FMQ	t (h)	Px[2]	K_2O	CaO	TiO_2	Cr_2O_3	Na_2O	MgO	Al_2O_3	FeO_T	MnO	SiO_2	Total	xWo[3]	xEn[3]	xFs[3]	Mg#[3]	$K_D^{Fe\text{-}Mg}$ [3]	$D_{Cr}^{px\text{-}liq}$ [3]
B1_1.3	1280	0.0001	0.10	24	opx	0.03	0.78	0.03	0.55	0.02	32.42	0.95	7.80	0.19	57.10	99.87	1.49	86.79	11.72	0.88	0.27	5.08
n=9			*0.02*			*0.01*	*0.04*	*0.03*	*0.09*	*0.01*	*0.30*	*0.17*	*0.34*	*0.01*	*0.22*	*0.30*	*0.09*	*0.58*	*0.53*	*0.01*	*0.01*	*0.83*
B1_2.3[1]	1280	0.0001	-0.16	24	opx	0.00	0.81	0.01	0.47	0.02	33.15	1.01	8.48	0.20	55.61	99.77	1.52	86.11	12.36	0.87	0.28	4.72
n=9			*0.01*			*0.00*	*0.17*	*0.01*	*0.05*	*0.01*	*0.79*	*0.65*	*0.34*	*0.02*	*0.82*	*0.53*	*0.35*	*1.01*	*0.67*	*0.01*	*0.01*	*0.54*
B1_2.4[1]	1280	0.0001	-0.15	12	opx	0.03	1.06	0.03	0.48	0.03	32.33	1.18	8.13	0.20	56.48	99.96	2.03	85.86	12.11	0.88	0.28	4.64
n=8			*0.01*			*0.02*	*0.32*	*0.03*	*0.09*	*0.03*	*0.61*	*0.51*	*0.32*	*0.02*	*0.48*	*0.63*	*0.62*	*1.06*	*0.55*	*0.01*	*0.01*	*0.86*
B1_1.6	1260	0.0001	0.02	48	opx	0.03	0.89	0.04	0.48	0.01	32.06	1.14	8.22	0.20	56.80	99.86	1.71	85.94	12.36	0.87	0.25	5.33
n=20			*0.05*			*0.01*	*0.06*	*0.02*	*0.10*	*0.01*	*0.55*	*0.31*	*0.63*	*0.02*	*0.21*	*0.27*	*0.12*	*1.07*	*0.99*	*0.01*	*0.02*	*1.09*
B1_1.9	1230	0.0001	0.04	48	opx	0.00	1.23	0.02	0.56	0.02	30.85	1.30	10.68	0.23	54.43	99.33	2.34	81.78	15.88	0.84	0.27	8.91
n=12			*0.04*			*0.00*	*0.05*	*0.01*	*0.09*	*0.01*	*0.29*	*0.37*	*0.18*	*0.02*	*0.40*	*0.28*	*0.10*	*0.38*	*0.31*	*0.00*	*0.01*	*1.45*
B1_1.11	1230	0.0001	0.05	96	opx	0.02	1.09	0.05	0.47	0.02	31.40	0.99	8.98	0.23	56.65	99.89	2.10	84.35	13.54	0.86	0.25	8.22
n=21			*0.00*			*0.01*	*0.04*	*0.02*	*0.07*	*0.01*	*0.31*	*0.15*	*0.16*	*0.02*	*0.30*	*0.40*	*0.08*	*0.31*	*0.27*	*0.00*	*0.01*	*1.20*
B1_5.2	1230	0.0001	-0.38	48	opx	0.03	1.18	0.03	0.47	0.02	30.38	0.78	10.15	0.24	56.59	99.88	2.29	82.28	15.43	0.84	0.26	7.23
n=18			*0.03*			*0.01*	*0.11*	*0.02*	*0.08*	*0.02*	*0.41*	*0.22*	*0.08*	*0.02*	*0.36*	*0.63*	*0.21*	*0.28*	*0.17*	*0.00*	*0.01*	*1.30*
B1_1.7	1200	0.0001	-0.03	48	opx	0.03	1.42	0.05	0.53	0.02	29.66	1.28	10.40	0.25	55.19	98.81	2.79	81.23	15.98	0.84	0.24	11.04
n=19			*0.10*			*0.01*	*0.05*	*0.02*	*0.08*	*0.01*	*0.28*	*0.16*	*0.25*	*0.02*	*0.31*	*0.26*	*0.11*	*0.48*	*0.41*	*0.00*	*0.01*	*1.85*
B1_2.2[1]	1200	0.0001	-0.20	48	opx	0.01	1.49	0.06	0.49	0.02	30.15	2.39	10.86	0.26	53.63	99.36	2.88	80.79	16.33	0.83	0.27	12.97
n=8			*0.01*			*0.01*	*0.25*	*0.02*	*0.05*	*0.01*	*0.88*	*0.32*	*0.86*	*0.02*	*0.43*	*0.15*	*0.50*	*1.90*	*1.40*	*0.02*	*0.06*	*1.48*
Lat_1.8	1170	0.0001	0.00	29.5	opx	0.03	1.55	0.02	0.67	0.02	28.17	2.68	11.72	0.00	53.89	98.75	3.11	78.53	18.36	0.81	0.26	18.15
n=11			*0.04*			*0.01*	*0.26*	*0.03*	*0.20*	*0.03*	*1.38*	*0.58*	*1.20*	*0.02*	*0.35*	*0.18*	*0.57*	*2.47*	*2.07*	*0.02*	*0.03*	*5.74*
B1_1.8	1170	0.0001	0.00	29.5	opx	0.03	1.64	0.06	0.52	0.02	28.89	1.84	11.19	0.26	54.46	98.89	3.24	79.49	17.27	0.82	0.23	15.62
n=11			*0.04*			*0.01*	*0.08*	*0.03*	*0.08*	*0.01*	*0.51*	*0.36*	*0.55*	*0.02*	*0.34*	*0.26*	*0.18*	*1.02*	*0.91*	*0.01*	*0.02*	*2.66*
B1_4.11	1370	0.51	-2.10	4	opx	0.03	1.18	0.03	0.23	0.04	32.21	0.96	8.52	0.19	57.63	101.01	2.24	85.12	12.64	0.87	0.32	1.80
n=3		*0.02*				*0.02*	*0.06*	*0.01*	*0.01*	*0.00*	*0.15*	*0.14*	*0.06*	*0.03*	*0.20*	*0.38*	*0.12*	*0.08*	*0.05*	*0.00*	*0.01*	*0.44*
B1_3.4	1280	0.51	-0.51	12	opx	0.03	1.68	0.05	1.29	0.06	29.24	2.21	9.60	0.23	55.04	99.43	3.37	81.60	15.02	0.84	0.28	11.02
n=19		*0.02*	*0.30*			*0.01*	*0.25*	*0.03*	*0.28*	*0.02*	*0.33*	*0.51*	*0.24*	*0.02*	*0.45*	*0.34*	*0.49*	*0.80*	*0.35*	*0.00*	*0.01*	*2.45*

Sample	T (°C)	P (GPa)	Δ FMQ	t (h)	Px[2]	K_2O	CaO	TiO_2	Cr_2O_3	Na_2O	MgO	Al_2O_3	FeO_T	MnO	SiO_2	Total	xWo[3]	xEn[3]	xFs[3]	Mg#[3]	$K_D^{Fe\text{-}Mg}$ [3]	$D_{Cr}^{px\text{-}liq}$ [3]
Lat_4.12	1260	0.51	-1.92	4	opx	0.01	1.97	0.02	0.58	0.06	27.06	4.37	11.78	0.01	54.33	100.21	4.05	77.11	18.84	0.80	0.34	7.93
n=10		*0.02*				*0.01*	*0.39*	*0.01*	*0.05*	*0.06*	*1.13*	*1.12*	*0.55*	*0.02*	*0.34*	*0.45*	*0.93*	*1.39*	*0.80*	*0.01*	*0.02*	*2.51*
Lat_3.5	1230	0.51	-0.24	12	opx	0.02	1.89	0.01	1.36	0.03	27.65	3.83	11.23	0.02	53.46	99.50	3.85	78.32	17.84	0.81	0.19	21.31
n=27		*0.02*	*0.14*			*0.01*	*0.13*	*0.02*	*0.27*	*0.01*	*0.58*	*0.99*	*0.38*	*0.01*	*0.89*	*0.46*	*0.28*	*0.79*	*0.63*	*0.01*	*0.01*	*8.32*
B1_3.5	1230	0.51	-0.34	12	opx	0.03	1.98	0.05	0.68	0.05	27.47	1.57	12.45	0.29	55.04	99.61	3.96	76.57	19.47	0.80	0.33	11.23
n=2		*0.02*	*0.16*			*0.00*	*0.03*	*0.02*	*0.00*	*0.00*	*0.33*	*0.19*	*0.15*	*0.03*	*0.33*	*0.54*	*0.10*	*0.09*	*0.02*	*0.00*	*0.06*	*4.36*
B1_3.5	1230	0.51	-0.34	12	cpx	0.25	4.32	0.12	0.68	0.45	21.71	4.10	12.03	0.27	55.95	99.88	10.64	67.74	21.62	0.76	0.40	11.33
n=16		*0.02*	*0.16*			*0.28*	*1.13*	*0.08*	*0.20*	*0.43*	*5.19*	*2.93*	*1.31*	*0.04*	*1.64*	*0.89*	*5.25*	*6.76*	*1.57*	*0.03*	*0.13*	*5.46*
B1_4.4	1500	1.03	-2.11	12	opx	0.01	1.13	0.04	0.55	0.07	31.76	1.25	8.59	0.15	57.22	100.75	2.17	84.94	12.88	0.87	0.31	3.50
n=1		*0.04*																			*0.01*	*0.82*
B1_4.6	1310	1.02	-1.79	12	opx	0.02	1.85	0.06	0.43	0.06	28.64	2.12	11.03	0.23	55.28	99.73	3.68	79.20	17.12	0.82	0.30	7.95
n=20		*0.02*				*0.01*	*0.14*	*0.03*	*0.09*	*0.02*	*0.53*	*0.38*	*0.24*	*0.02*	*0.52*	*0.72*	*0.31*	*0.63*	*0.38*	*0.00*	*0.02*	*4.40*
Lat_3.3	1280	1.02	-0.27	12	opx	0.02	1.80	0.00	2.12	0.06	27.47	6.72	9.70	0.02	52.19	100.10	3.78	80.32	15.91	0.83	0.32	20.24
n=3		*0.02*	*0.13*			*0.01*	*0.08*	*0.04*	*0.12*	*0.01*	*0.24*	*0.48*	*0.13*	*0.00*	*0.50*	*0.31*	*0.12*	*0.16*	*0.04*	*0.00*	*0.01*	*1.17*
B1_3.3	1280	1.02	-0.22	12	opx	0.02	1.96	0.07	1.67	0.08	27.47	3.39	10.74	0.24	53.85	99.49	4.04	78.69	17.27	0.82	0.30	14.13
n=19		*0.02*	*0.13*			*0.01*	*0.10*	*0.02*	*0.33*	*0.01*	*0.57*	*0.76*	*0.44*	*0.03*	*0.76*	*0.32*	*0.21*	*0.80*	*0.78*	*0.01*	*0.02*	*2.94*
B1_3.7	1280	1.02	-0.28	12	opx	0.03	1.95	0.04	1.68	0.08	28.08	3.36	10.04	0.27	53.92	99.45	3.99	79.97	16.04	0.83	0.30	13.14
n=20		*0.02*	*0.18*			*0.01*	*0.09*	*0.02*	*0.25*	*0.01*	*0.52*	*0.63*	*0.22*	*0.02*	*0.68*	*0.53*	*0.18*	*0.47*	*0.45*	*0.00*	*0.01*	*1.98*
Lat_3.8	1230	1.02	0.04	12	cpx	0.03	6.97	0.03	1.43	0.21	19.83	5.47	13.57	0.02	51.62	99.18	15.48	61.04	23.48	0.72	0.34	24.26
n=17		*0.02*	*0.26*			*0.02*	*0.78*	*0.03*	*0.21*	*0.05*	*1.27*	*1.10*	*0.38*	*0.01*	*0.93*	*0.56*	*1.99*	*2.05*	*0.75*	*0.01*	*0.09*	*13.57*
B1_3.8	1230	1.02	-0.22	12	cpx	0.04	5.67	0.11	1.52	0.22	22.80	4.20	11.92	0.32	52.49	99.28	12.16	67.92	19.92	0.77	0.50	22.82
n=20		*0.02*	*0.14*			*0.02*	*1.33*	*0.03*	*0.21*	*0.06*	*1.17*	*0.62*	*0.57*	*0.02*	*0.58*	*0.43*	*2.94*	*2.63*	*0.92*	*0.01*	*0.15*	*8.92*

All oxides values in wt % and *n*= number of analyses. Italicized numbers indicate one standard deviation.

Footnotes: 1. Melting experiments. 2. Px indicates pyroxene type in which opx – orthopyroxene and cpx – clinopyroxene. 3. Pyroxene compositions expressed as wollastonite content - xWo = $Ca/(Ca+Mg+Fe_T)$, enstatite content - xEn = $Mg/(Ca+Mg+Fe_T)$, ferrosilite content - xFs = $Fe_T/(Ca+Mg+Fe_T)$, Mg#= $Mg/(Mg+Fe_T)$ and partition coefficients: $K_D^{Fe\text{-}Mg} = (x_{Fe}^{px}\, x_{Mg}^{liq})/ (x_{Fe}^{liq}\, x_{Mg}^{px})$, $D_{Cr}^{px\text{-}liq} = Cr_2O_3^{pyroxene}/\, Cr_2O_3^{melt}$.

Table 3.2. Summary of Fe-Ir capsule compositions and calculated fO_2.

				Wire		Glass		1st iteration	2nd iteration			3rd iteration		
Sample	T (°C)	P (GPa)	t (h)	Fe	Ir	FeO_T	Rel. % Diff.	Log fO_2	FeO	Fe_2O_3	Log fO_2	FeO	Fe_2O_3	Log fO_2
Lat_3.5	1230	0.51	12	1.96	96.95	8.98	0.02	-7.84	7.54	1.52	-7.98	7.61	1.45	-7.98
n=14		*0.02*		*0.12*	*0.71*	*0.21*		*0.14*	*0.18*	*0.00*	*0.14*	*0.18*	*0.03*	*0.14*
B1_3.5	1230	0.51	12	1.90	96.66	7.63	5.61	-7.95	6.52	1.29	-8.09	6.58	1.23	-8.08
n=16		*0.02*		*0.20*	*0.52*	*0.32*		*0.16*	*0.25*	*0.00*	*0.16*	*0.26*	*0.05*	*0.16*
Lat_3.4	1280	0.51	12	1.76	97.61	7.56	11.9	-7.39	6.48	1.21	-7.52	6.53	1.15	-7.51
n=14		*0.02*		*0.25*	*0.76*	*0.10*		*0.18*	*0.09*	*0.00*	*0.18*	*0.09*	*0.02*	*0.18*
B1_3.4	1280	0.51	12	2.21	97.07	7.95	10.8	-7.59	6.85	1.22	-7.72	6.90	1.16	-7.71
n=15		*0.02*		*0.63*	*0.57*	*0.11*		*0.30*	*0.09*	*0.00*	*0.30*	*0.10*	*0.02*	*0.30*
Lat_3.8	1230	1.02	12	1.35	98.98	9.19	9.2	-7.23	7.46	1.92	-7.40	7.57	1.80	-7.39
n=20		*0.02*		*0.32*	*0.60*	*0.54*		*0.26*	*0.44*	*0.00*	*0.26*	*0.45*	*0.10*	*0.26*
B1_3.8	1230	1.02	12	1.36	99.42	6.96	13.2	-7.49	5.73	1.36	-7.66	5.81	1.28	-7.65
n=19		*0.02*		*0.22*	*0.51*	*0.67*		*0.21*	*1.28*	*0.00*	*0.21*	*0.57*	*0.12*	*0.21*
Lat_3.3	1280	1.02	12	1.40	98.51	7.15	11.9	-7.03	5.97	1.31	-7.18	6.03	1.24	-7.17
n=13		*0.02*		*0.12*	*0.18*	*0.13*		*0.14*	*0.11*	*0.02*	*0.14*	*0.11*	*0.02*	*0.14*
B1_3.3	1280	1.02	12	1.29	98.66	6.88	16.0	-6.70	5.65	1.37	-7.14	5.72	1.29	-7.12
n=15		*0.02*		*0.06*	*0.59*	*0.11*		*0.13*	*0.09*	*0.02*	*0.13*	*0.09*	*0.02*	*0.13*
Lat_3.7	1280	1.02	12	1.40	99.07	6.86	22.5	-7.06	5.72	1.27	-7.21	5.78	1.20	-7.20
n=20		*0.02*		*0.44*	*0.81*	*0.07*		*0.32*	*0.25*	*0.00*	*0.32*	*0.06*	*0.01*	*0.32*
B1_3.7	1280	1.02	12	1.30	99.15	6.43	23.5	-7.03	5.29	1.27	-7.20	5.36	1.19	-7.19
n=20		*0.02*		*0.19*	*0.47*	*0.09*		*0.18*	*0.08*	*0.02*	*0.18*	*0.08*	*0.02*	*0.18*

All oxides values in wt %, *n*= number of analyses and FeO_T indicates all Fe expressed as FeO. The FeO and Fe_2O_3 in the glass was calculated using the method of Kress and Carmichael (1991) from the estimated experimental fO_2. Italicized numbers indicate one standard deviation. Iron loss during the experiment is expressed as the relative % difference: Rel. % Diff. = ((FeO_T in run-product - FeO_T in the starting material) / FeO_T in the starting material)*100.

Table 3.3. Summary of major element compositions of run-product chromites.

Sample	T (°C)	P (GPa)	Δ FMQ	t (h)	CaO	TiO_2	MgO	Al_2O_3	Cr_2O_3	FeO_T	FeO	Fe_2O_3[2]	MnO	SiO_2	Total	Cr #[3]	Fe #[3]
Lat_1.3	1280	0.0001	0.10	24	0.33	0.04	10.76	18.62	45.12	22.73	17.81	5.47	0.01	0.28	98.37	0.62	0.48
n=4			*0.02*		*0.04*	*0.03*	*0.15*	*0.87*	*1.36*	*0.24*	*0.24*	*0.20*	*0.01*	*0.17*	*0.56*	*0.02*	*0.01*
B1_1.3	1280	0.0001	0.10	24	0.22	0.32	12.45	11.87	52.09	20.45	14.28	6.85	0.19	0.45	98.73	0.75	0.39
n=7			*0.02*		*0.02*	*0.04*	*0.14*	*0.92*	*1.64*	*0.32*	*0.18*	*0.43*	*0.02*	*0.13*	*0.35*	*0.02*	*0.01*
Lat_1.10	1280	0.0001	-0.14	48	0.38	0.04	10.75	18.81	43.99	23.21	17.68	6.15	0.05	0.59	98.45	0.61	0.48
n=6			*0.01*		*0.02*	*0.01*	*0.04*	*0.36*	*0.24*	*0.19*	*0.09*	*0.25*	*0.02*	*0.14*	*0.17*	*0.01*	*0.00*
B1_1.10	1280	0.0001	-0.14	48	0.24	0.29	12.76	12.12	51.38	20.69	13.80	7.66	0.26	0.44	98.95	0.74	0.38
n=6			*0.01*		*0.02*	*0.01*	*0.25*	*0.31*	*0.49*	*0.10*	*0.23*	*0.23*	*0.01*	*0.18*	*0.67*	*0.01*	*0.01*
Lat_2.3[1]	1280	0.0001	-0.16	24	0.35	0.07	10.63	19.40	43.72	23.93	18.32	6.23	0.01	0.31	99.04	0.60	0.49
n=14			*0.01*		*0.04*	*0.01*	*0.08*	*0.28*	*0.38*	*0.33*	*0.11*	*0.32*	*0.01*	*0.19*	*0.30*	*0.01*	*0.00*
B1_2.3[1]	1280	0.0001	-0.16	24	0.24	0.26	12.07	10.51	50.75	21.51	13.91	8.44	0.23	0.48	96.90	0.76	0.39
n=15			*0.01*		*0.02*	*0.02*	*0.35*	*0.45*	*0.42*	*0.32*	*0.11*	*0.36*	*0.01*	*0.13*	*1.44*	*0.01*	*0.01*
Lat_2.4[1]	1280	0.0001	-0.15	12	0.37	0.03	10.71	19.29	43.72	23.57	18.00	6.19	0.01	0.71	99.03	0.60	0.49
n=15			*0.01*		*0.02*	*0.02*	*0.23*	*0.36*	*0.17*	*0.20*	*0.26*	*0.22*	*0.01*	*0.38*	*0.50*	*0.00*	*0.01*
B1_2.4[1]	1280	0.0001	-0.15	12	0.26	0.30	12.38	11.92	50.62	21.06	14.10	7.74	0.18	0.66	98.17	0.74	0.39
n=15			*0.01*		*0.03*	*0.03*	*0.19*	*0.43*	*0.56*	*0.14*	*0.16*	*0.24*	*0.02*	*0.21*	*0.67*	*0.01*	*0.00*
Lat_5.1	1280	0.0001	-0.40	48	0.35	0.01	11.19	15.95	47.71	21.99	16.57	6.02	0.03	0.50	98.33	0.67	0.45
n=2			*0.00*		*0.04*	*0.06*	*0.50*	*0.12*	*0.30*	*0.88*	*0.94*	*0.14*	*0.01*	*0.26*	*0.07*	*0.00*	*0.03*
B1_5.1	1280	0.0001	-0.40	48	0.24	0.35	11.91	10.66	52.83	21.20	14.86	7.05	0.21	0.29	98.41	0.77	0.41
n=5			*0.00*		*0.02*	*0.03*	*0.14*	*0.50*	*0.98*	*0.20*	*0.20*	*0.42*	*0.01*	*0.07*	*0.23*	*0.01*	*0.01*
Lat_1.6	1260	0.0001	0.02	48	0.35	0.06	10.88	19.19	44.12	22.75	17.66	5.65	-0.01	0.47	98.37	0.61	0.48
n=4			*0.05*		*0.04*	*0.02*	*0.17*	*0.34*	*0.31*	*0.28*	*0.18*	*0.27*	*0.02*	*0.31*	*0.38*	*0.01*	*0.07*
B1_1.6	1260	0.0001	0.02	48	0.28	0.38	12.11	13.45	48.73	21.46	14.75	7.45	0.20	0.49	97.83	0.71	0.41
n=7			*0.05*		*0.03*	*0.05*	*0.30*	*1.19*	*1.84*	*0.17*	*0.30*	*0.46*	*0.02*	*0.20*	*0.21*	*0.03*	*0.01*
Lat_1.9	1230	0.0001	0.04	48	0.41	0.08	11.24	24.49	38.19	23.14	18.00	5.72	0.00	0.80	98.94	0.51	0.47
n=3			*0.04*		*0.02*	*0.01*	*0.10*	*0.88*	*1.33*	*0.25*	*0.39*	*0.21*	*0.02*	*0.18*	*0.89*	*0.02*	*0.01*
B1_1.9	1230	0.0001	0.04	48	0.24	0.42	11.24	14.83	45.11	24.19	16.25	8.83	0.23	0.37	97.51	0.67	0.45
n=1			*0.04*														
Lat_1.11	1230	0.0001	0.05	96	0.32	0.05	10.97	22.03	38.27	25.29	17.88	8.24	0.00	0.35	98.10	0.54	0.48
n=5			*0.00*		*0.03*	*0.01*	*0.15*	*0.63*	*0.86*	*0.34*	*0.24*	*0.44*	*0.00*	*0.18*	*0.18*	*0.01*	*0.01*

Sample	T (°C)	P (GPa)	Δ FMQ	t (h)	CaO	TiO_2	MgO	Al_2O_3	Cr_2O_3	FeO_T	FeO	Fe_2O_3[2]	MnO	SiO_2	Total	Cr #[3]	Fe #[3]
B1_1.11	1230	0.0001	0.05	96	0.22	0.37	11.37	13.92	43.58	26.58	15.93	11.84	0.21	0.73	98.17	0.68	0.44
n=3			*0.00*		*0.03*	*0.04*	*0.21*	*0.86*	*0.64*	*0.21*	*0.02*	*0.24*	*0.01*	*0.59*	*0.14*	*0.02*	*0.00*
Lat_5.2	1230	0.0001	-0.38	48	0.32	0.08	10.64	17.78	43.54	23.16	17.23	6.59	0.01	0.46	96.65	0.62	0.48
n=20			*0.03*		*0.04*	*0.03*	*0.56*	*2.23*	*2.83*	*0.10*	*0.49*	*0.44*	*0.02*	*0.39*	*0.35*	*0.04*	*0.02*
B1_5.2	1230	0.0001	-0.38	48	0.21	0.38	10.24	11.33	48.13	25.88	17.25	9.59	0.25	0.26	97.66	0.74	0.49
n=6			*0.03*		*0.02*	*0.07*	*0.15*	*0.94*	*1.52*	*0.87*	*0.38*	*0.62*	*0.03*	*0.10*	*0.54*	*0.02*	*0.01*
Lat_2.2[1]	1200	0.0001	-0.20	48	0.48	0.08	10.92	21.79	32.98	28.94	17.39	12.83	0.01	1.51	97.99	0.50	0.47
n=15			*0.01*		*0.05*	*0.00*	*0.23*	*1.07*	*1.05*	*0.52*	*0.51*	*0.11*	*0.01*	*0.75*	*0.72*	*0.02*	*0.01*
B1_2.2[1]	1200	0.0001	-0.20	48	0.35	0.47	10.54	14.27	37.73	31.82	17.09	16.38	0.23	1.28	98.34	0.63	0.48
n=14			*0.01*		*0.08*	*0.05*	*0.03*	*0.53*	*0.12*	*0.77*	*0.10*	*0.75*	*0.03*	*0.13*	*0.27*	*0.01*	*0.00*
Lat_3.4	1280	0.51	-0.32	12	0.37	0.01	12.10	22.83	42.67	19.71	16.39	3.69	0.00	0.69	98.73	0.56	0.43
n=1		*0.02*	*0.18*														
B1_3.4	1280	0.51	-0.51	12	0.32	0.27	10.99	14.12	49.93	20.76	16.42	4.82	0.19	1.17	98.92	0.70	0.46
n=1		*0.02*	*0.30*														
Lat_3.5	1230	0.51	-0.24	12	0.39	0.07	7.09	13.79	49.04	27.04	22.59	4.95	0.02	0.55	98.49	0.70	0.64
n=3		*0.02*	*0.14*		*0.09*	*0.02*	*0.07*	*1.35*	*1.73*	*0.32*	*0.32*	*0.08*	*0.01*	*0.46*	*0.11*	*0.03*	*0.01*
B1_3.5	1230	0.51	-0.34	12	0.27	0.23	7.46	9.72	53.96	25.57	21.33	4.71	0.25	0.72	98.58	0.79	0.62
n=5		*0.02*	*0.16*		*0.03*	*0.01*	*0.13*	*0.70*	*0.69*	*0.39*	*0.35*	*0.25*	*0.03*	*0.20*	*0.57*	*0.01*	*0.01*
Lat_3.3	1280	1.02	-0.27	12	0.45	0.06	12.72	26.48	39.19	18.72	15.99	3.04	0.00	1.37	99.28	0.50	0.41
n=2		*0.02*	*0.13*		*0.07*	*0.03*	*0.21*	*0.32*	*0.79*	*0.16*	*0.11*	*0.17*	*0.00*	*0.38*	*0.79*	*0.01*	*0.00*
B1_3.3	1280	1.02	-0.22	12	0.46	0.22	10.82	17.53	47.01	20.99	17.30	4.11	0.24	3.21	100.90	0.64	0.47
n=4		*0.02*	*0.13*		*0.08*	*0.00*	*0.46*	*1.02*	*1.28*	*0.25*	*0.40*	*0.72*	*0.02*	*0.47*	*0.02*	*0.02*	*0.02*
Lat_3.7	1280	1.02	-0.30	12	0.30	0.04	12.63	22.37	45.28	17.84	15.75	2.32	0.03	0.37	99.08	0.58	0.41
n=4		*0.02*	*0.32*		*0.08*	*0.03*	*0.23*	*1.39*	*0.93*	*0.13*	*0.43*	*0.59*	*0.02*	*0.22*	*0.41*	*0.02*	*0.01*
B1_3.7	1280	1.02	-0.28	12	0.25	0.22	10.31	12.46	54.51	20.64	17.74	3.22	0.29	0.44	99.44	0.75	0.49
n=4		*0.02*	*0.18*		*0.05*	*0.06*	*0.33*	*1.36*	*2.07*	*0.18*	*0.27*	*0.44*	*0.03*	*0.13*	*0.45*	*0.03*	*0.01*
Lat_3.8	1230	1.02	0.04	12	0.26	0.09	7.13	13.58	49.66	26.33	22.44	4.32	-0.01	0.40	97.89	0.71	0.64
n=2		*0.02*	*0.26*		*0.13*	*0.01*	*0.05*	*1.33*	*3.06*	*0.06*	*0.29*	*0.25*	*0.00*	*0.18*	*1.76*	*0.03*	*0.00*
B1_3.8	1230	1.02	-0.22	12	0.21	0.18	7.76	10.04	56.69	23.22	21.14	2.31	0.25	0.15	98.74	0.79	0.60
n=1		*0.02*	*0.14*														

All oxides values in wt %, *n*= number of analyses and FeO_T indicates all Fe expressed as FeO. Italicized numbers indicate one standard deviation. Footnotes: 1. Melting experiments. 2. FeO and Fe_2O_3 content calculated from stoichiometry using the method of Barnes and Roeder (2001). 3. Chromite compositions expressed as chromium number – Cr# = Cr/(Cr+Al) and iron number – Fe# = Fe^{2+}/(Mg+ Fe^{2+}).

Table 3.4. Summary of equations used for chromite crystallization models.

Composition	Equation #	Pressure	y	x	Slope		Intercept		r^2
Lat	1	All	log CCCS (μg/g)	10^4/T (K)	-1.01	± 0.04	9.33	± 0.29	0.95
B1	2	All	log CCCS (μg/g)	10^4/T (K)	-1.02	± 0.03	9.42	± 0.19	0.98
	3	0.1 MPa	log $D_{Cr(px/liq)}$	10^4/T (K)	1.10	± 0.07	-6.40	± 0.47	0.97
	4	0.5 GPa	log $D_{Cr(px/liq)}$	10^4/T (K)	1.10		-6.03		
	5	1 GPa	log $D_{Cr(px/liq)}$	10^4/T (K)	1.10	± 0.13	-5.95	± 0.83	0.99
	6	0.1 MPa	X_{px}	T (˚C)	-0.0016	± 0.0003	2.0383	± 0.3240	0.98
	7	0.5 GPa	X_{px}	T (˚C)	-0.0012	± 0.0002	1.6720	± 0.2998	0.96
	8	1 GPa	X_{px}	T (˚C)	-0.0010	± 0.0001	1.5707	± 0.0756	0.99

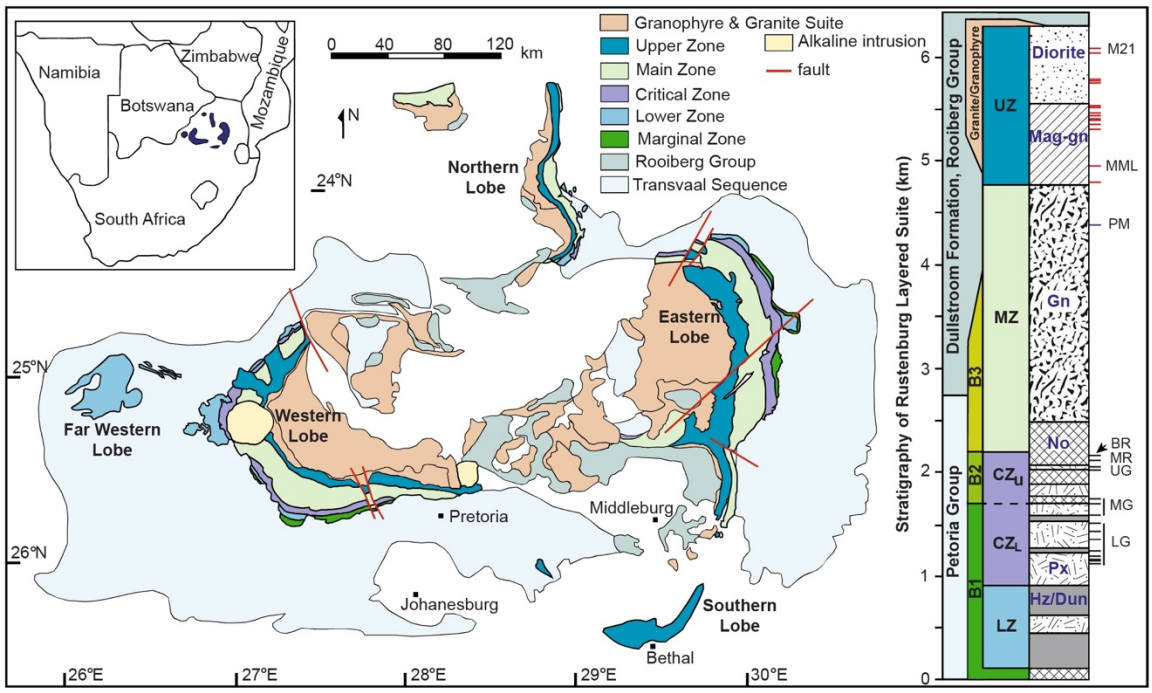

Figure 1.1. Geologic map of the Bushveld Complex and stratigraphic sequence of the Rustenburg Layered Suite, modified from Yao *et al.* (2021). The location of the Complex in South Africa is shaded on the inset map. In the stratigraphic section, chromite horizons are black lines and magnetite horizons are red lines. Position of the Rustenburg Layered Suite within host rocks, Pretoria Group and Rooiberg Group, varies throughout the Complex. Abbreviations: LG – Lower Group chromitites, MG – Middle Group chromitites, UG – Upper Group chromitites, MR – Merensky Reef, BR – Bastard Reef, PM – Pyroxenite Marker, MML – main magnetite layer, M21 – magnetite layer 21, LZ – Lower Zone, CZ_L – Lower Critical Zone, CZ_L – Lower Critical Zone, CZ_U – Upper Critical Zone, MZ – Main Zone, UZ – Upper Zone, Hz – harzburgite, Dun – dunite, Px – pyroxenite, No – norite, Gn – gabbronorite, Mg-gn – magnetite gabbronorite.

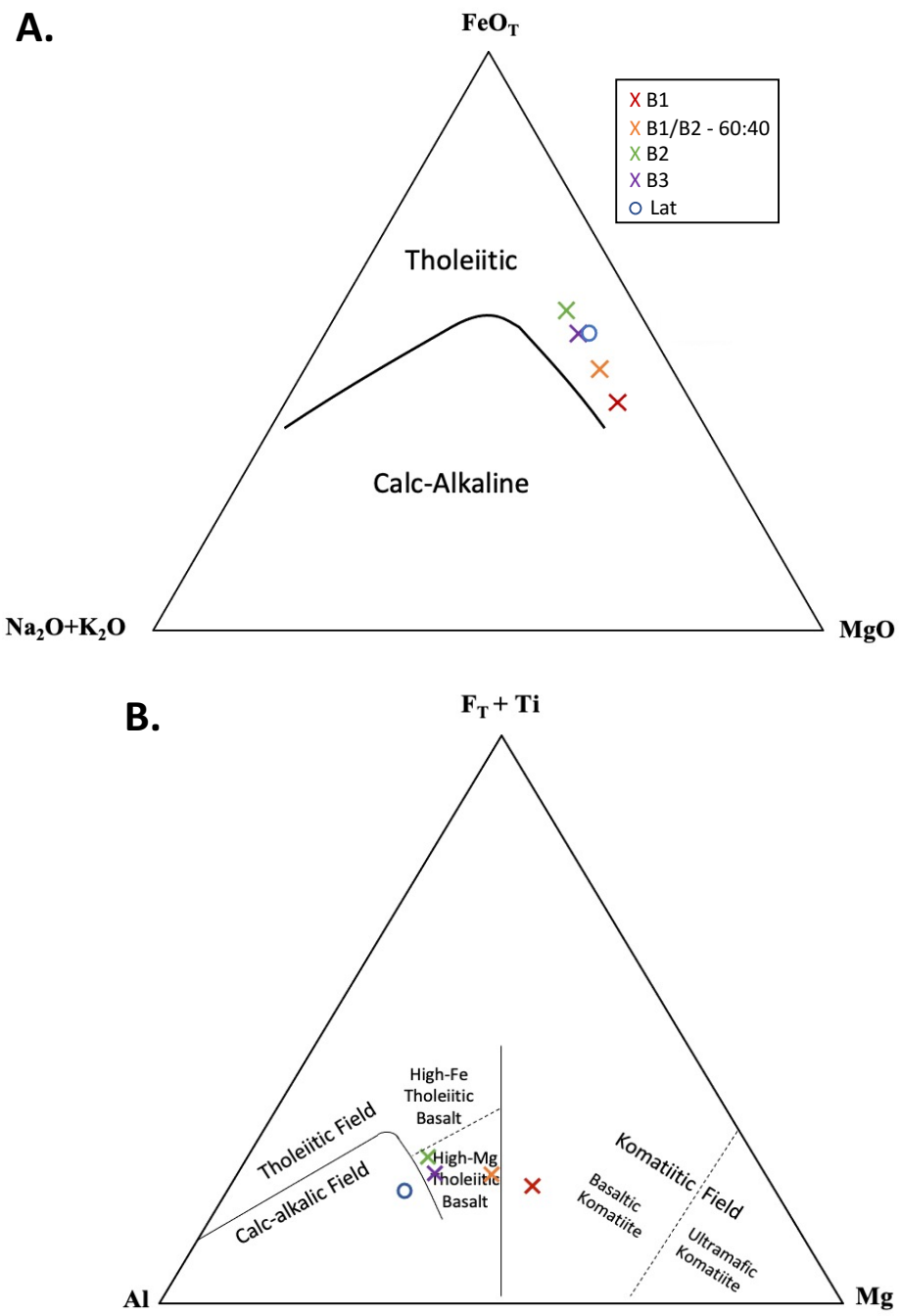

Figure 1.2. Classification of proposed parental magmas in the Bushveld Complex by major elements. The X symbols represent the average compositions for B1, B2, and B3 reported by Barnes *et al.* (2010) and the B1-B2 mix suggested by Barnes *et al.* (2010). The circle represents the composition used in the MELTS thermodynamic model of Latypov *et al*. (2018). A) AFM diagram. B) Jensen (1976) cation plot.

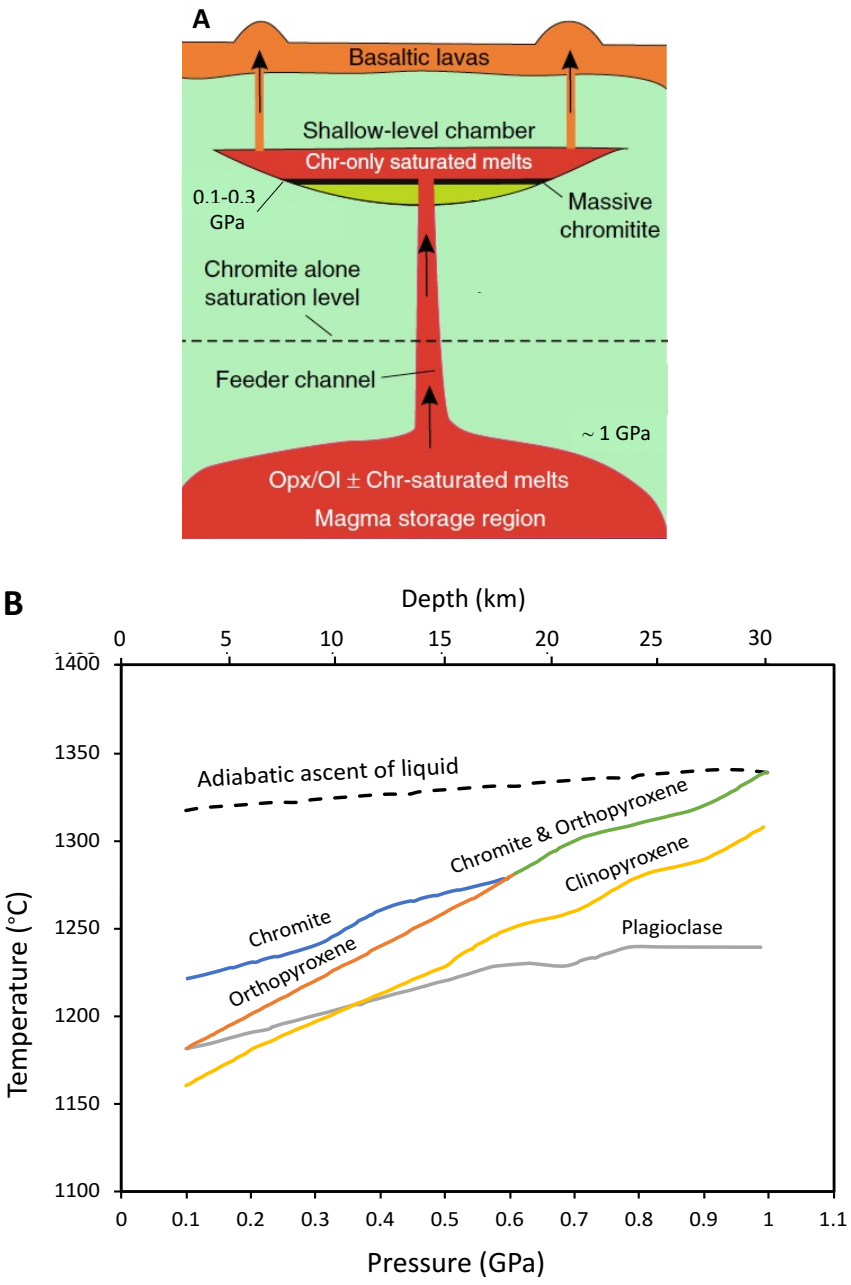

Figure 1.3. Pressure reduction hypothesis. A) Schematic from Latypov *et al.* (2018) describing the pressure reduction hypothesis. A magma saturated in chromite, with orthopyroxene or olivine, rises. As pressure decreases the melt becomes saturated in chromite-alone. The melt reaches the main chamber and crystallizes chromite as the sole liquidus phase, forming a massive chromitite. B) Summary of the results of the MELTS thermodynamic model described in Latypov *et al.* (2018). At high pressure the melt is saturated in orthopyroxene and chromite first (green). As pressure decreases to about 0.6 GPa, the melt becomes saturated in chromite-alone (blue), followed by orthopyroxene (orange). Modified from Latypov *et al*. (2018). Abbreviations: Opx – orthopyroxene, Ol – olivine, Chr – chromite, Pl – plagioclase, Cpx – clinopyroxene.

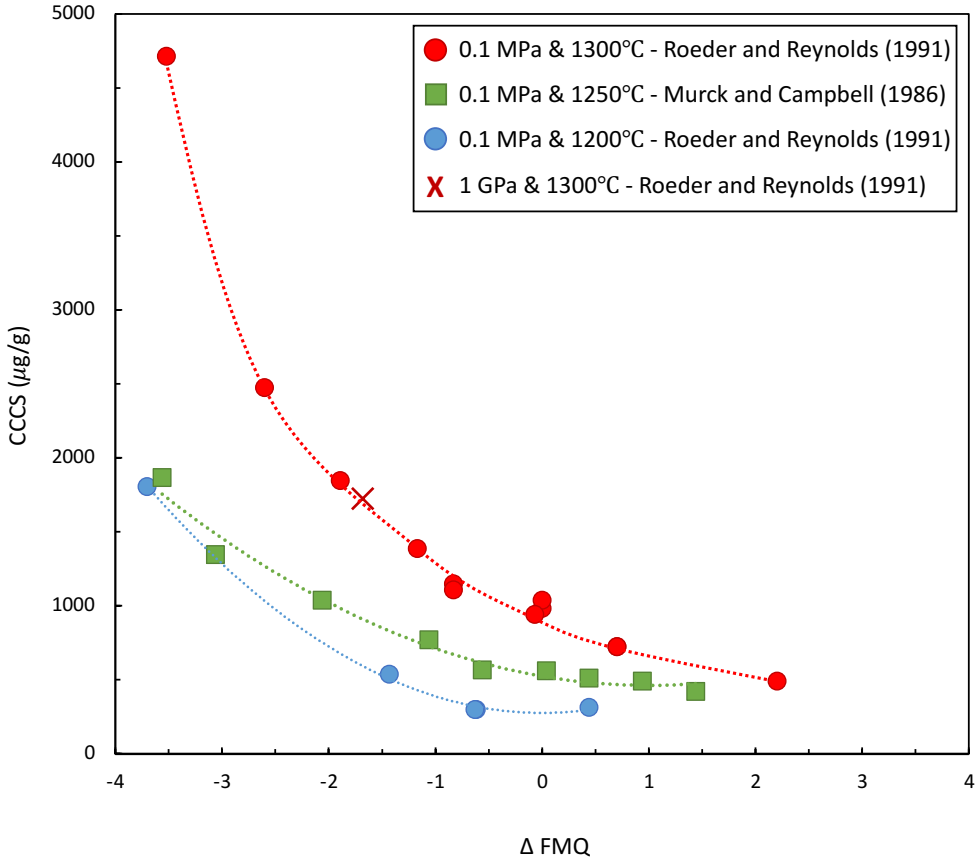

Figure 1.4. Plot of the CCCS as a function of ΔFMQ summarizing previous experimental data measured at 0.1 MPa and 1 GPa for the '401 diabase' basaltic composition. Squares represent data from Murck and Campbell (1986) and circles and x symbols represent data from Roeder and Reynolds (1991).

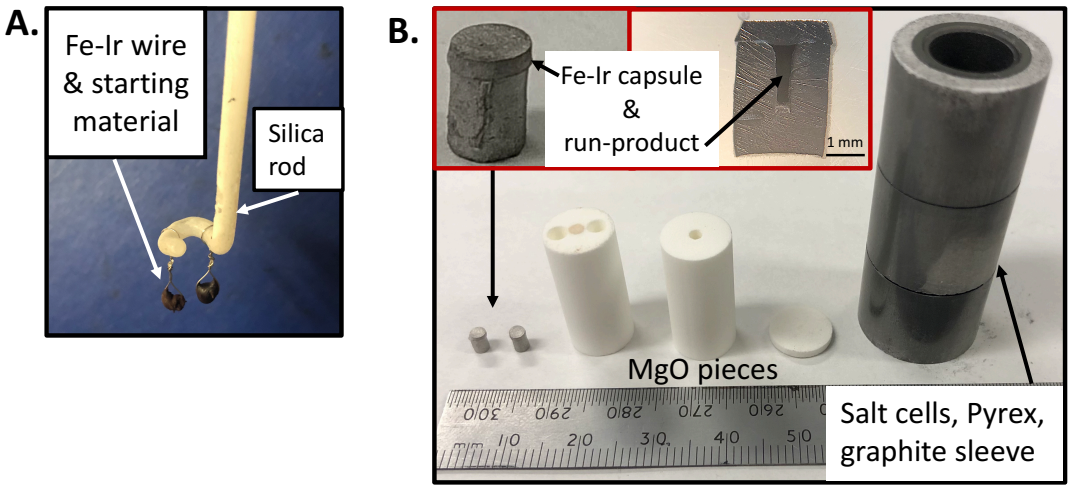

Figure 2.1. Configuration for low- and high-pressure experiments. A) Gas mixing furnace sample configuration in which samples mounted on pre-saturated Fe-Ir loops are suspended from a silica rod. B) Cell used for 19.05 mm diameter piston-cylinder pressure vessel. Components include salt cells, Pyrex sleeve, graphite sleeve and MgO pieces. Fe-Ir capsule, both post-experiment and sectioned revealing the internal sample.

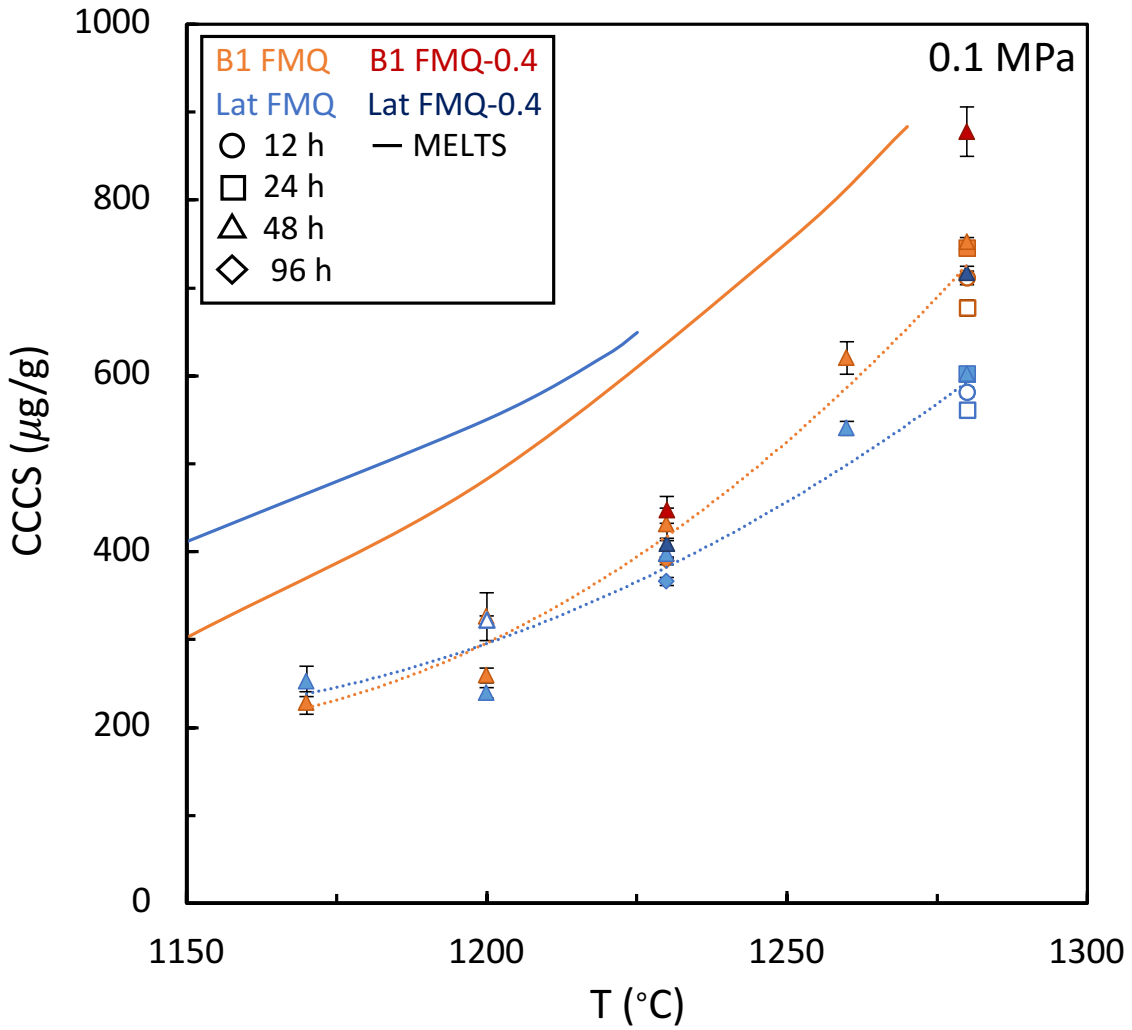

Figure 3.1. Plot of the CCCS as a function of temperature showing results of experiments done at 0.1 MPa. Solid symbols represent crystallization experiments and hollow symbols represent melting experiments. Symbol shapes correspond to experimental duration in which a circle is 12 h, a square is 24 h, a triangle is 48 h, and a diamond is 96 h. Orange and light blue represent experiments done at ~FMQ, for the B1 and the Lat composition, respectively. Dark red and blue represent experiments done at ~FMQ-0.4, for the B1 and the Lat composition, respectively. Error bars represent one standard deviation of multiple analyses. In some cases, error bars are smaller than the symbols. Solid lines represent results for the same compositions as predicted by the MELTS thermodynamic model.

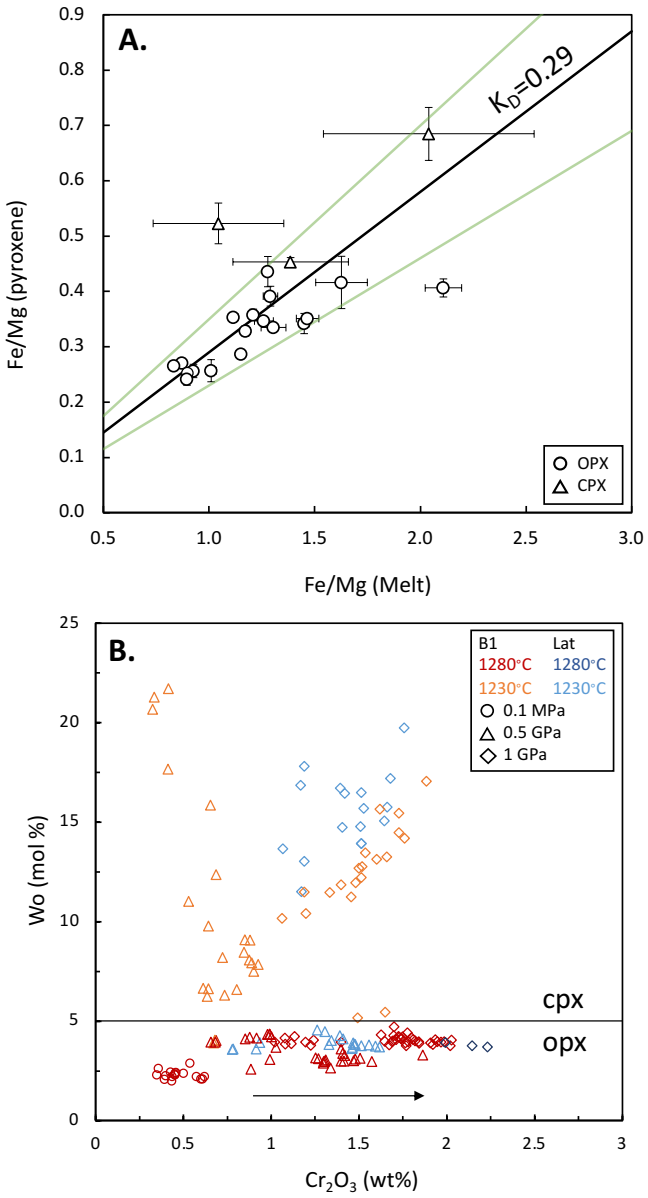

Figure 3.2. Compositional characteristics of experimental pyroxenes. A) Fe/Mg in pyroxene as a function of Fe/Mg in the melt. The black line represents the distribution coefficient, K_D $(Fe\text{-}Mg)^{opx\text{-}liq}$ = 0.29 ± 0.06, defined by Putirka (2008) with one standard deviation represented by green lines. The circles are orthopyroxene, and the triangles are clinopyroxene. Error bars represent one standard deviation of multiple analyses. In some cases, error bars are smaller than the symbols. B) Wo (mol %) as a function of Cr_2O_3 (wt%) for pyroxenes. The black line at 5 mol % Wo represents the transition between orthopyroxene and clinopyroxene based on pyroxene nomenclature convention (Morimoto 1988). The black arrow is in the direction of increasing pressure. Symbol shapes correspond to experimental pressure: circles are at 0.1 MPa, triangles are at 0.5 GPa, and diamonds are at 1 GPa. Dark red and blue represent experiments at 1280°C for B1 and Lat, respectively. Orange and light blue represent experiments at 1230°C for B1 and Lat, respectively. Abbreviations: opx – orthopyroxene, cpx – clinopyroxene, Wo= $[Ca/(Ca+Mg+Fe_T)]*100$.

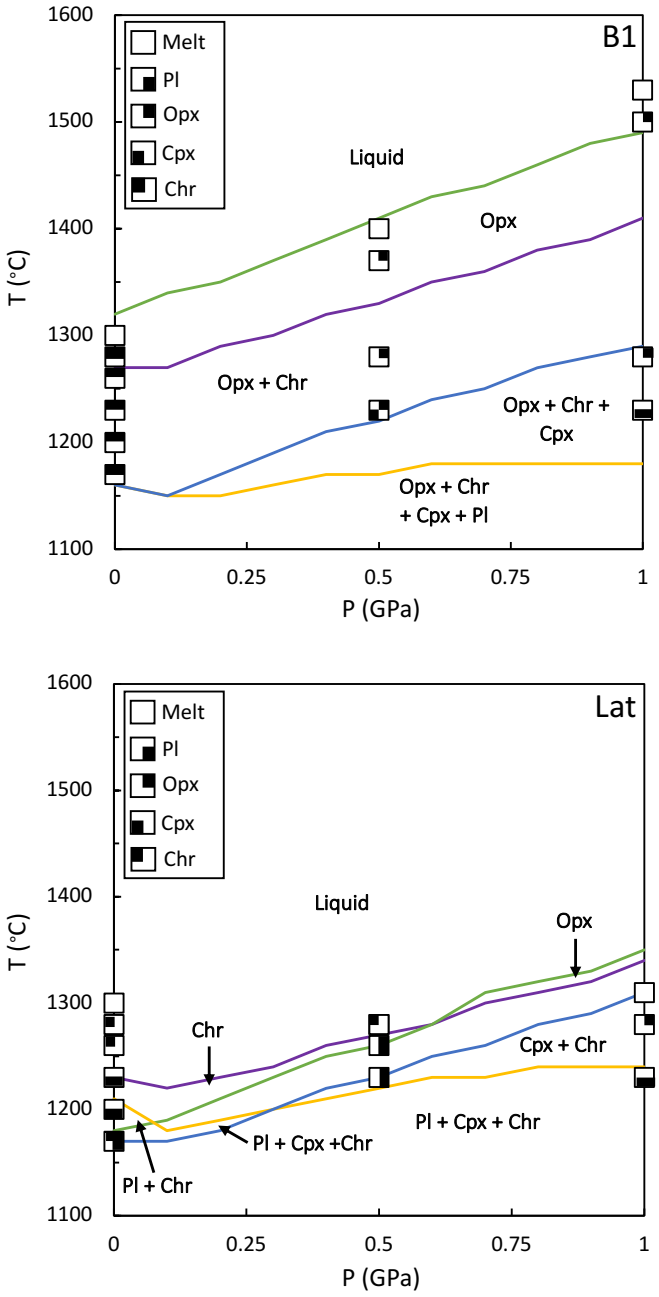

Figure 3.3. Comparison of measured phase equilibria for the B1 and Lat compositions with the MELTS thermodynamic model. Each quadrant of the box symbol designates a phase present in the experiment. The chromite crystallization temperature from experiments is based on the solubility relations established at ~ FMQ for an initial Cr content Cr of 859 µg/g and 681 µg/g, for B1 and Lat, respectively. The solid lines represent the crystallization temperature modelled by MELTS for each composition; green is orthopyroxene-in, purple is chromite-in, yellow is plagioclase-in and blue is clinopyroxene-in. Abbreviations: opx – orthopyroxene, cpx – clinopyroxene, pl – plagioclase, and chr – chromite.

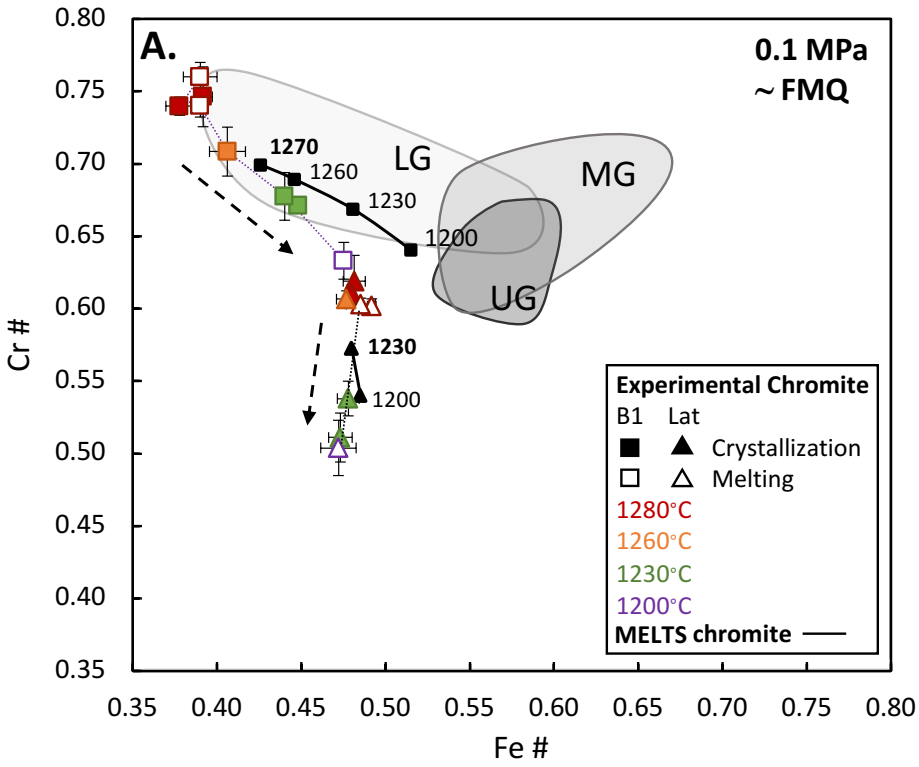

Figure 3.4. Cr# of chromite as a function of Fe# of chromite in experiments done at 0.1 MPa and ~ FMQ from 1280°C to 1200°C compared to chromite compositions from massive chromitites in the Critical Zone (compiled from Von Gruenewaldt and Worst (1986), Naldrett *et al.* (2009), and Langa *et al.* (2021)). Squares are B1 and triangles are Lat. Solid symbols represent crystallization experiments and hollow symbols represent melting experiments. The colours correspond to experimental temperature (1280°C – red, 1260°C – orange, 1230°C – green and 1200°C – purple). The black dashed arrow is in the direction of decreasing temperature. Error bars represent one standard deviation of multiple analyses. In some cases, error bars are smaller than the symbols. Solid black symbols represent MELTS predictions for each composition. Abbreviations: LG – Lower Group chromitites, MG – Middle Group chromitites, UG – Upper Group chromitites.

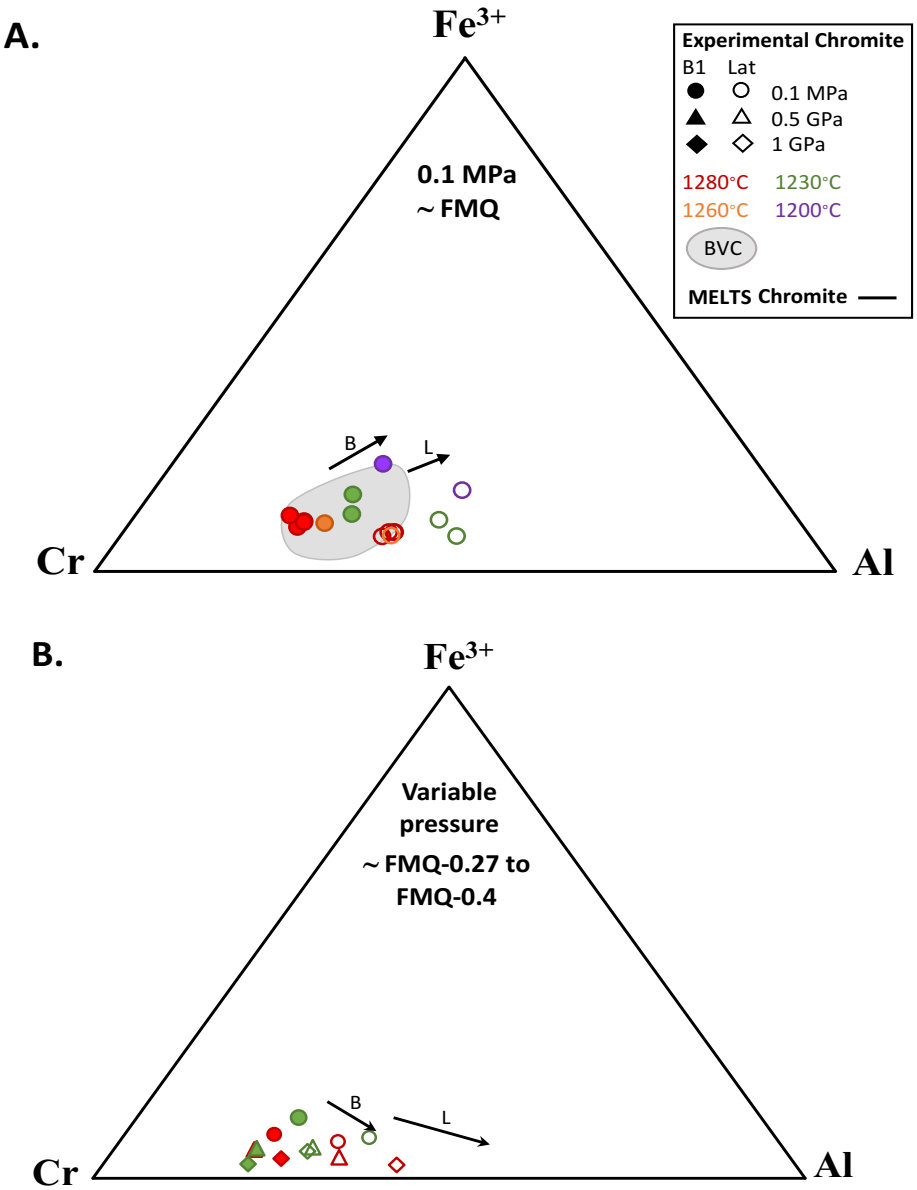

Figure 3.5. Trivalent cation plots portraying experimental chromite compositions. The colours in A and B correspond to experimental temperature (1280°C – red, 1260°C – orange, 1230°C – green and 1200°C – purple). Solid symbols represent B1 and hollow symbols represent Lat. A) Trivalent cation plot for chromite produced in experiments done at 0.1 MPa and ~ FMQ compared to chromite compositions from massive chromitites in the Bushveld (BVC) (compiled from Von Gruenewaldt and Worst (1986), Naldrett *et al.* (2009), and Langa *et al.* (2021)). Solid black arrow represents MELTS predictions pointing down temperature for B (B1) and L (Lat). B) Trivalent cation plot for chromite produced in experiments over the pressure interval studied at ~ FMQ-0.27 to FMQ-0.4. Symbol shapes correspond to experimental pressure in which a circle is at 0.1 MPa, a triangle is 0.5 GPa, and a diamond is at 1 GPa. Solid black arrow represents MELTS predictions pointing in the direction of increasing pressure for B (B1) and L (Lat).

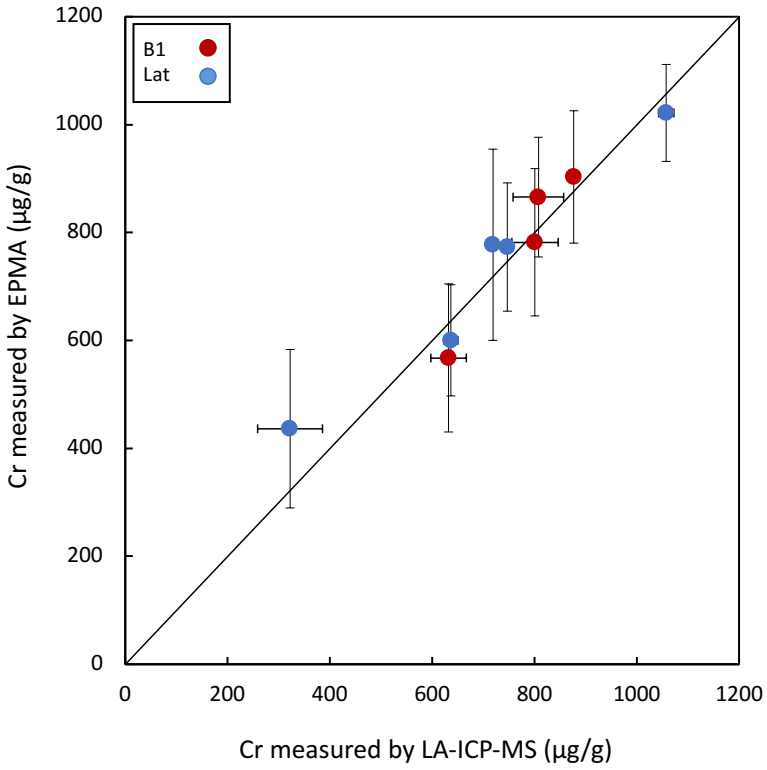

Figure 3.6. Chromium content in the glass phase measured by the Electron Probe Microanalyzer as a function of the Cr content in the glass phase measured by Laser-Ablation Inductively Coupled Plasma Mass Spectrometer. Red symbols represent experiments done using the B1 composition and blue symbols represent experiments done using the Lat composition. The solid black line represents a 1:1 ratio. Error bars represent one standard deviation of multiple analyses. In some cases, error bars are smaller than the symbols.

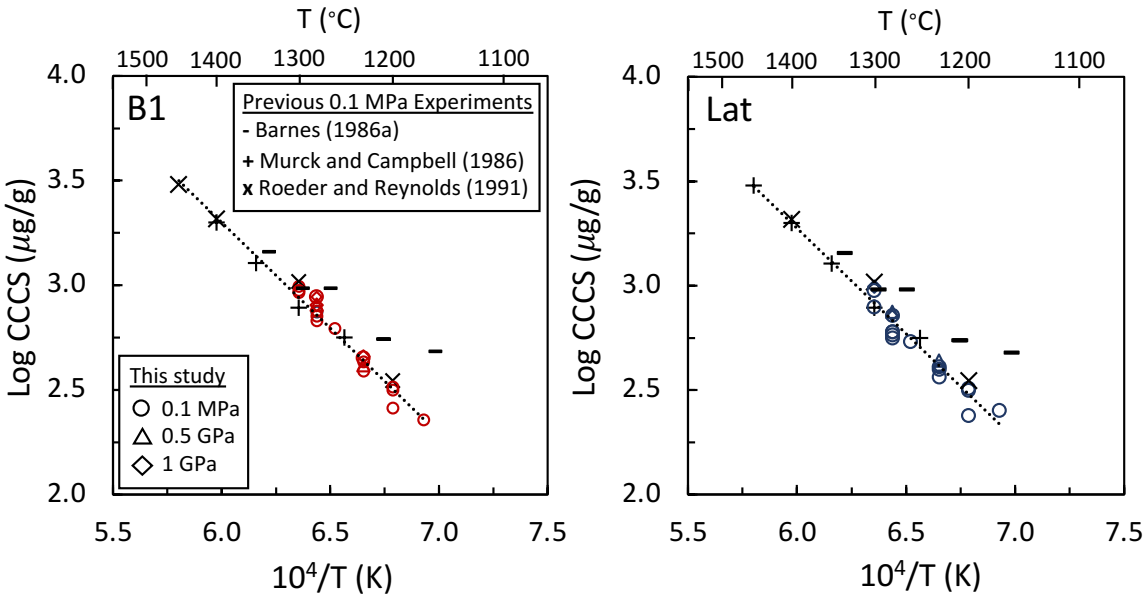

Figure 3.7. Log CCCS as a function of inverse temperature at fO_2 ranging from ~ FMQ to FMQ-0.4 for B1 (red) and Lat (blue), at all pressures investigated. Also included are the previous experimental results obtained at 0.1 MPa for the '401 diabase' basaltic composition by Murck and Campbell (1986), represented by plus signs, and Roeder and Reynolds (1991), represented by x symbols, as well as a B1-orthopyroxene mix by Barnes (1986a), represented by dash signs. Linear regressions of the data (excluding Barnes 1986a) are provided in Table 3.4 (Equations 1 and 2 for B1 and Lat, respectively).

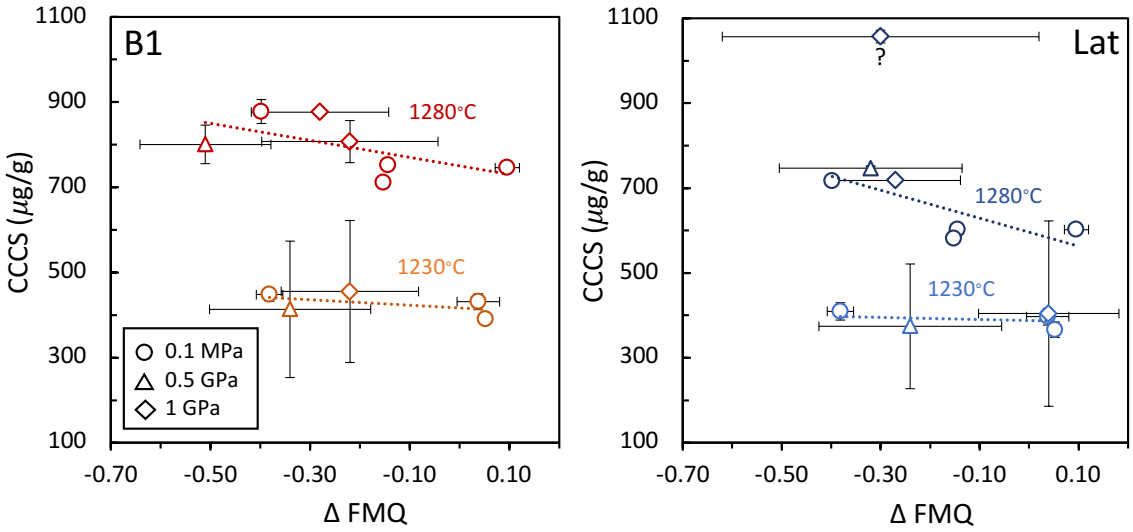

Figure 3.8. CCCS as a function of ΔFMQ for the B1 and the Lat compositions. Symbol shapes correspond to experimental pressure: circles are at 0.1 MPa, triangles are at 0.5 GPa, and diamonds are at 1 GPa. Dark red and blue represent experiments at 1280°C, for B1 and Lat, respectively. Orange and light blue represent experiments at 1230°C, for B1 and Lat, respectively. Dashed lines represent the linear line of best fit for each isotherm. Error bars represent one standard deviation of multiple analyses. In some cases, error bars are smaller than the symbols.

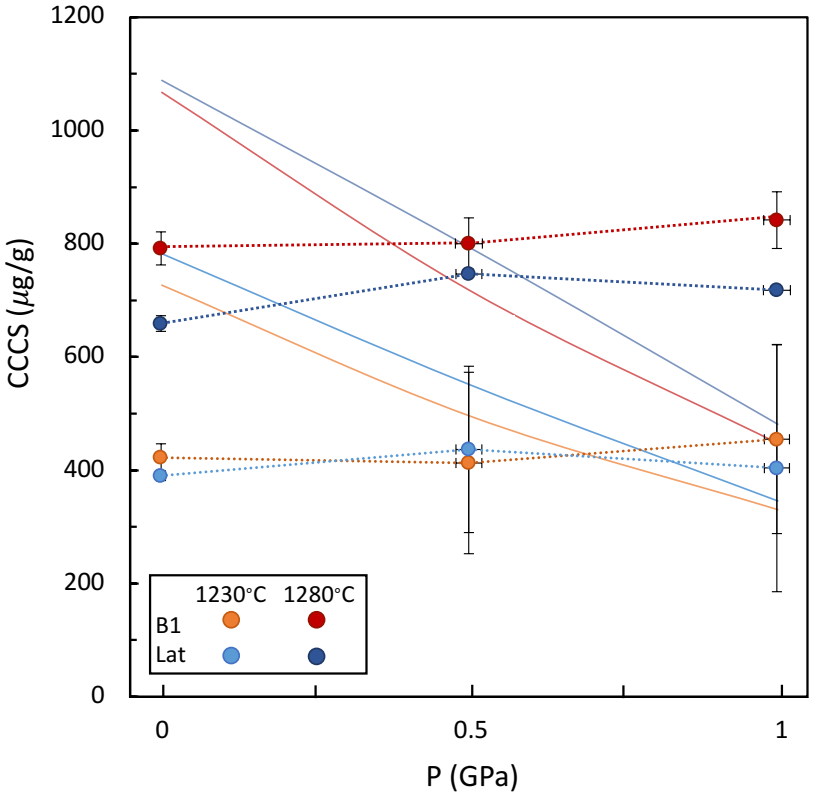

Figure 3.9. CCCS as a function of pressure. Circles represent the average CCCS of multiple experiments done at ~ FMQ to FMQ-0.4, in which dark red and blue represent experiments at 1280°C, for B1 and Lat, respectively. And, orange and light blue represent experiments at 1230°C, for B1 and Lat, respectively. Error bars represent one standard deviation of multiple analyses. In some cases, error bars are smaller than the symbols. Solid lines represent MELTS predictions for each composition at 1280°C and 1230°C.

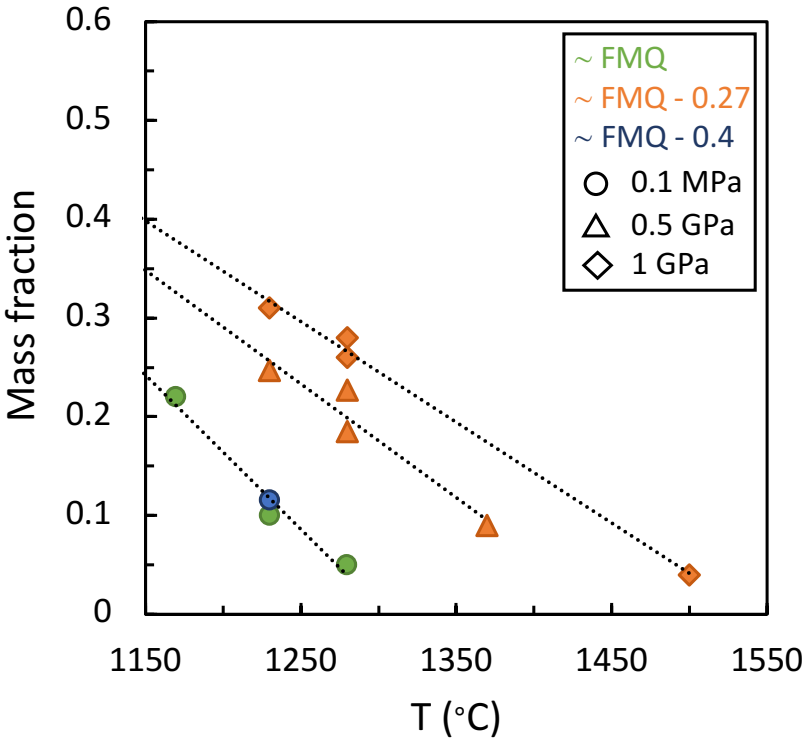

Figure 3.10. Mass fraction of pyroxene produced by the B1 composition as a function of temperature. Experiments done at 0.1 MPa are circles, at 0.5 GPa are triangles and at 1 GPa are diamonds and at FMQ in green, FMQ-0.27 in orange and FMQ-0.4 in blue. Dashed lines represent the linear line of best fit at each pressure which are summarized in Table 3.4 (Equations 6, 7, and 8).

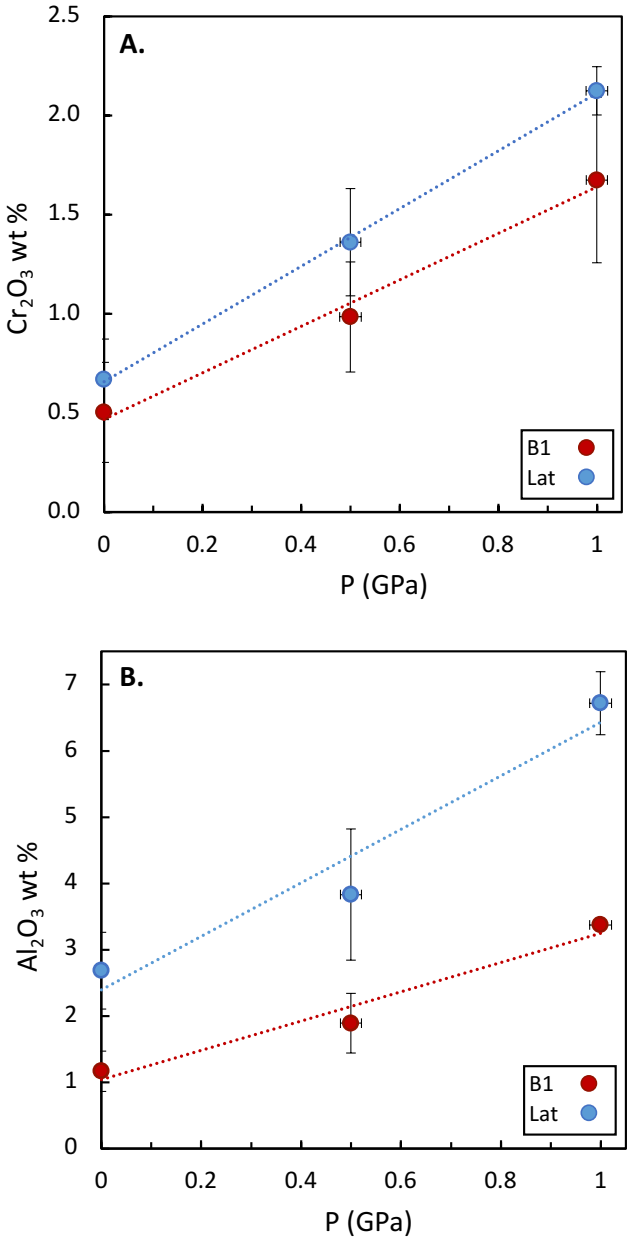

Figure 3.11. Experimental orthopyroxene compositions produced by the B1 composition (red) and the Lat composition (blue) as a function of pressure. Error bars represent one standard deviation of multiple analyses. In some cases, error bars are smaller than the symbols. A) Average Cr_2O_3 content in orthopyroxene. The equation of linear line of best fit is y = 1.17(±0.12)x + 0.47(±0.08), r^2=0.99, for B1 and y = 1.46(±0.04)x + 0.66(±0.03), r^2=0.99, for Lat. B) Average Al_2O_3 content in orthopyroxene. The equation of linear line of best fit is y = 2.21(±0.44)x + 1.04(±0.28), r^2=0.98, for B1 and y = 4.04(±1.00)x + 2.39(±0.65), r^2=0.98, for Lat.

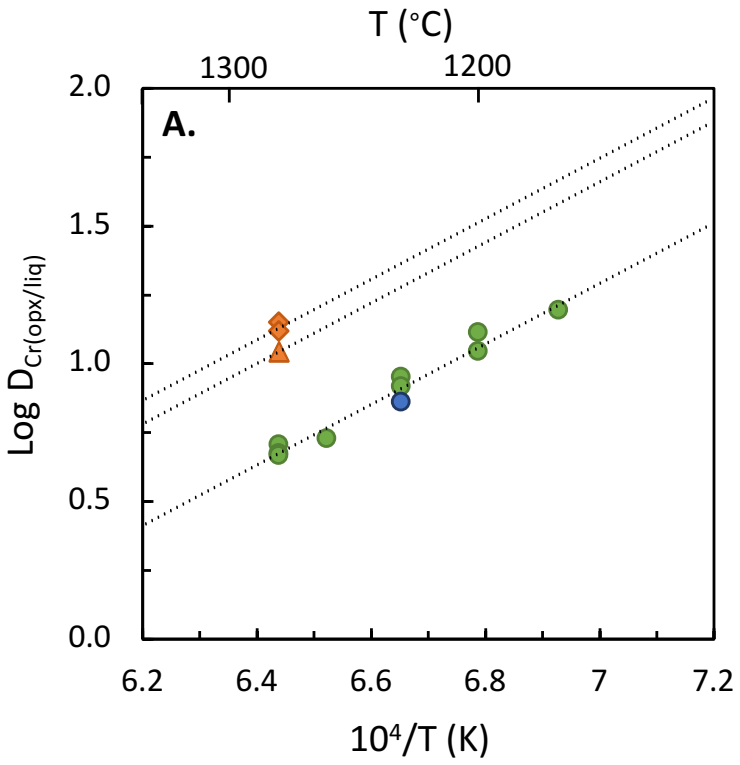

Figure 3.12. Log $D_{Cr(opx/liq)}$ as a function of inverse temperature for the B1 composition. Experiments done at 0.1 MPa are circles, at 0.5 GPa are triangles and at 1 GPa are diamonds and at FMQ in green, ~ FMQ-0.27 in orange and FMQ-0.4 in blue. Dashed lines represent the linear line of best fit which are summarized in Table 3.4 (Equations 3, 4, and 5)

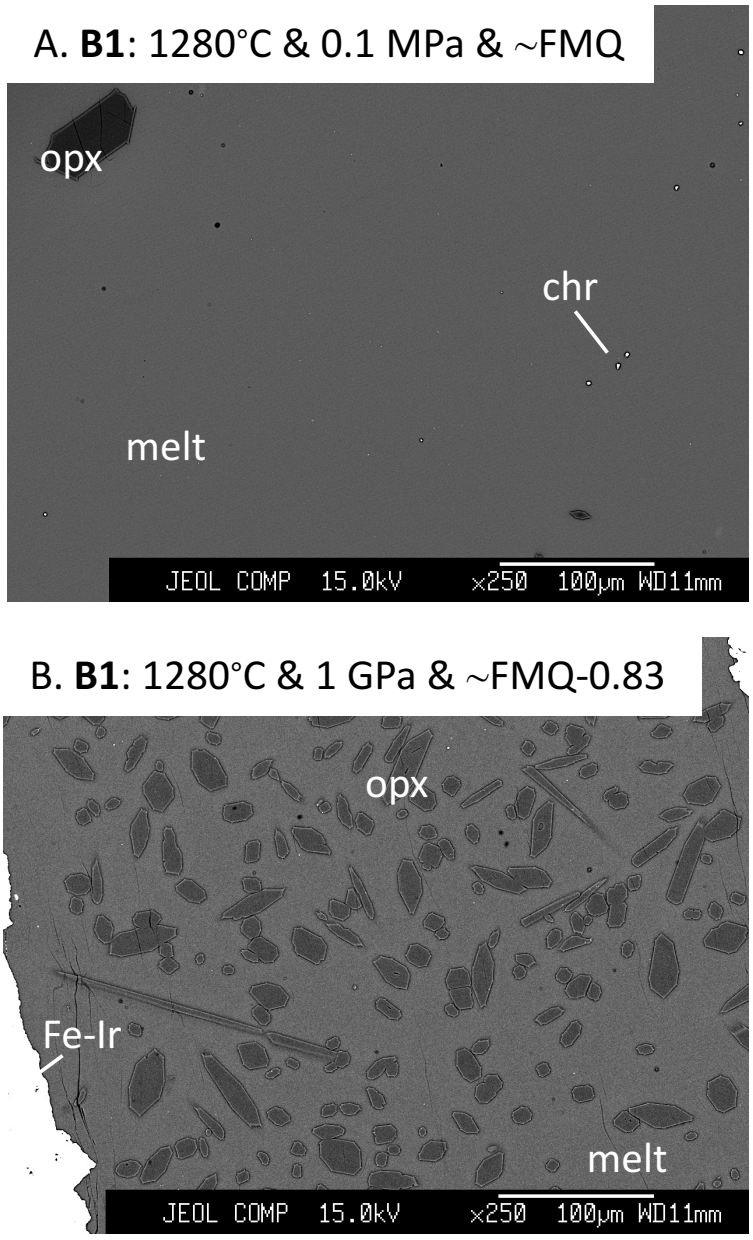

Figure 4.1. Backscattered electron images portraying the modal abundance of orthopyroxene crystallizing in experiments done at A) 0.1 MPa and B) 1 GPa and 1280°C. Both images are at 250x magnification. Abbreviations: opx – orthopyroxene, chr – chromite, Fe-Ir – Fe-Ir alloy capsule.

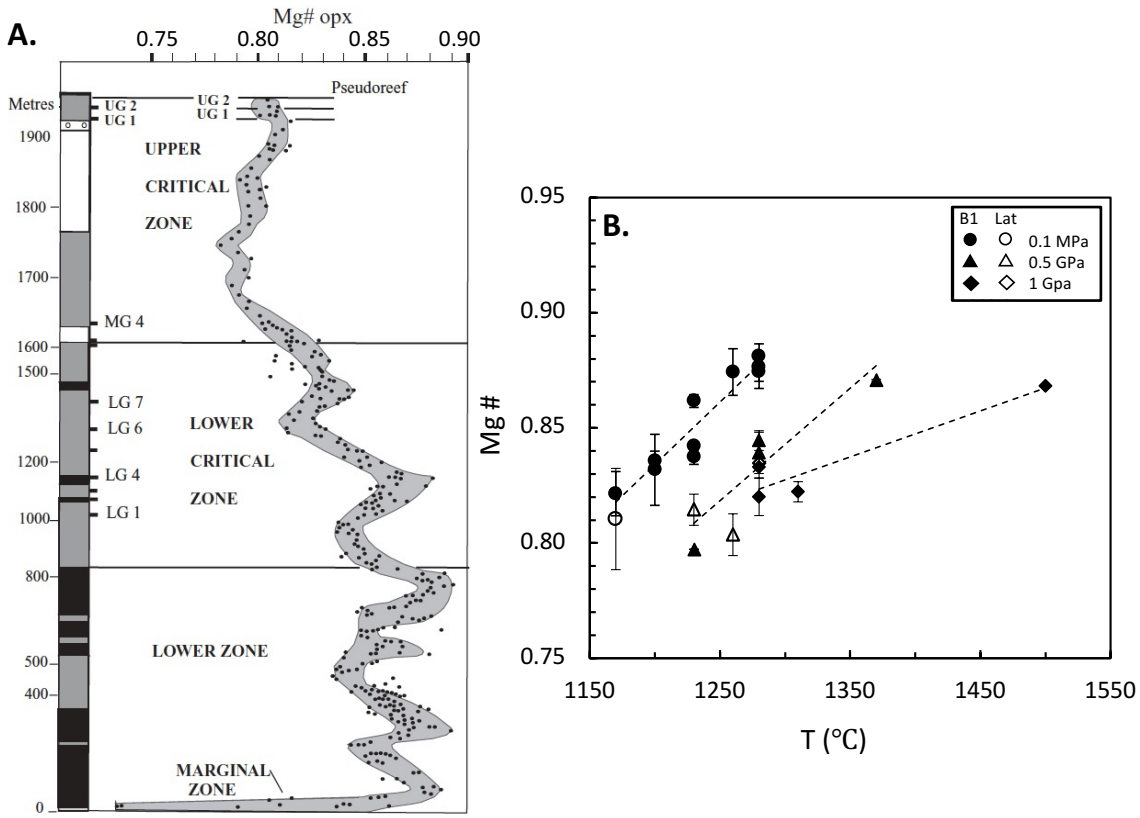

Figure 4.2. Comparison of orthopyroxene Mg#. A) Variation in Mg# of orthopyroxene with stratigraphic height through the LZ and CZ. Modified from Eales and Costin (2012). B) Experimental orthopyroxene Mg# as a function of temperature. Solid symbols represent B1 and hollow symbols represent Lat. Symbol shapes correspond to experimental pressure in which a circle is at 0.1 MPa, a triangle is 0.5 GPa, and a diamond is 1 GPa. Dashed lines represent the linear line of best fit. Error bars represent one standard deviation of multiple analyses. In some cases, error bars are smaller than the symbols.

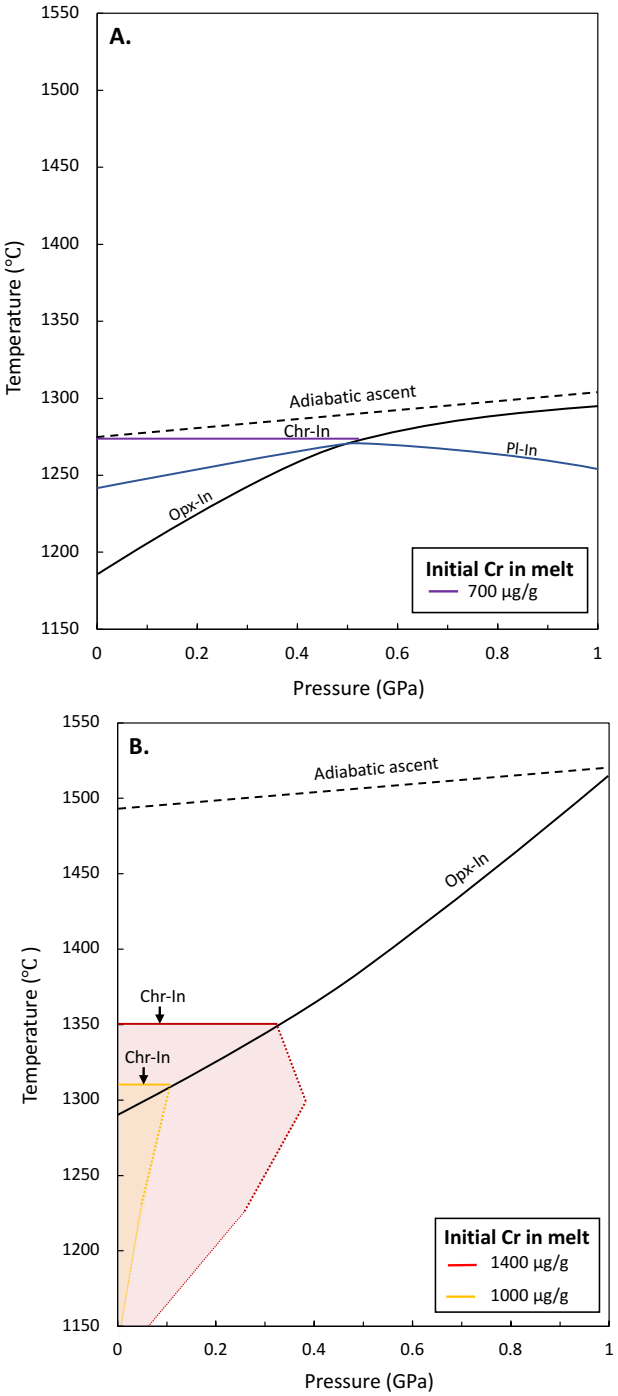

Figure 4.3. Chromite crystallization models for A) the Lat composition and B) the B1 composition in pressure-temperature space. Dashed black lines represent the adiabatic ascent of the liquid modelled by MELTS and solid lines are established from experiments. Orthopyroxene-in (black line) and plagioclase-in (blue line) are established from silicate phase equilibria experiments. Chromite-in curve, calculated from experimental CCCS data, is represented by the red line for 1400 µg/g Cr in the melt, yellow for 1000 µg/g Cr in the melt and purple for 700 µg/g Cr in the melt. Shaded regions in B) correspond to conditions of chromite crystallization.

APPENDIX A:
Gas Mixing Furnace fO_2 Calibration

1.0 Introduction

The accuracy of the Y-doped zirconia fO_2 sensor in the gas mixing furnace was tested using the (Ni,Mn)O binary oxide sensor method by Taylor *et al.* (1992). Mixtures of NiO and MnO form a continuous solid solution of $(Ni_x\text{-}Mn_{x\text{-}1})O$, in which x is dependent on fO_2. Thus, by equilibrating mixtures of NiO and MnO in the gas mixing furnace, the imposed fO_2 can be calculated. The fO_2 measured by the Y-doped zirconia sensor was found to be within 0.07 log units of the binary oxide sensor result.

2.0 Thermodynamic Basis

The Ni-NiO redox sensor is defined by the reaction:

$$Ni_{(s)} + \frac{1}{2}O_{2(g)} = NiO_{(s)}. \quad \text{(A1)}$$

The equilibrium constant (K_{eq}) for this reaction is expressed as:

$$K_{eq} = \frac{a_{NiO}}{a_{Ni}\, {fO_2}^{1/2}}, \quad \text{(A2)}$$

in which a_{NiO} is the activity of the metal oxide, NiO, and a_{Ni} is the activity of Ni metal. The equilibrium constant can also be written as:

$$\log K_{eq} = \log(a_{NiO}) - \left[\log(a_{Ni}) + \frac{1}{2}\log(fO_2)\right]. \quad \text{(A3)}$$

If the metal oxide and metal phases are pure, the respective activity is one and the equilibrium constant is:

$$\log K_{eq} = -\frac{1}{2}\log(fO_2). \quad \text{(A4)}$$

By diluting the metal oxide phase with MnO, the activity is lowered, and the fO_2 can be calculated using:

$$\log fO_2 = -2\left[\log K_{eq} - \log(a_{NiO})\right]. \quad \text{(A5)}$$

Taylor *et al*. (1992) compiled activity-compositional data for the (Ni,Mn)O binary oxide system between 600°C and 1300°C and derived the following equation to calculate fO_2:

$$\log fO_2\ (Ni,Mn)O = 2\log(X_{NiO}) - \frac{1}{2.3025\ RT}\left\{\begin{matrix}(480104 - 244.7T + 21.1078T\log(T)) \\ -[2(1-X_{NiO})^2(9731 + 2.388T)]\end{matrix}\right\}, \quad \text{(A6)}$$

in which X_{NiO} is the mole fraction of NiO, T is temperature in K and R is the gas constant in J/mol·K.

2.0 Method

Starting materials were prepared from reagent grade oxides and metal powder, which were ground under ethanol in an agate mortar. Two mixtures were prepared, both with MnO_2, one with excess Ni, and the other with excess NiO. By running both simultaneously, the equilibrium composition was approached in the former mixture by oxidizing Ni and the latter by reducing NiO.

The experiment was done at 0.1 MPa in a vertical-tube gas mixing furnace in the Dalhousie Experimental Geochemistry Laboratory and at 1200°C for a duration of 48 h at $\log fO_2$ = -8.41 (FMQ), recorded by the Y-doped zirconia sensor. A Type S (Pt-$PtRh_{10}$) thermocouple was used to measure temperature inside the furnace and mass flow controllers regulated the flow of oxidizing (CO_2) and reducing (CO) gases to control the fO_2. Mixtures were pressed into thick-walled silica tubes (ID = 3 mm, OD = 8 mm) and were suspended from a hook fashioned at the end of a high purity silica rod with Pt wire (Figure A1). Experiments were executed by first withdrawing the silica rod to the top of the furnace tube, then sealing the furnace and commencing gas flow. The sample was

then lowered into the predetermined hotspot and remained there for the experiment duration. Experiments were terminated by opening the bottom of the furnace and lowering the silica rod through the bottom and into a beaker of water. Before and after the experiment, fO_2 was measured using Y-doped zirconia sensor.

Run-products were mounted in a 25 mm diameter epoxy puck, then polished and carbon coated for EPMA analysis in the Robert M. MacKay Electron Microprobe Laboratory at Dalhousie University. Oxide compositions were analyzed using a 15 kV accelerating voltage, a 20 nA beam current and a 1 μm beam size. Count times were 30 s for Mn and 20 s for Ni. Standards for analyses were pure Ni metal and pyrolusite for Mn.

3.0 Results

Run conditions and results are summarized in Table A1. The log fO_2 calculated with Equation A6 using the resultant oxide compositions is 8.34 ± 0.01 which is 0.07 log units more oxidizing than the measurement recored by the Y-doped zirconia sensor.

4.0 References

Taylor, J.R., Wall, V.J., and Pownceby, M.I. 1992. The calibration and application of accurate redox sensors. American Mineralogist, **77**: 284–295.

Table A1. Summary of results from the binary oxide redox sensor method and Y-doped zirconia sensor for experiments done at 0.1 MPa.

Sample	T (°C)	P (GPa)	t (h)	Sensor log fO_2	MnO (wt%)	NiO (wt%)	Total (wt%)	X_{MnO}	X_{NiO}	Calculated log fO_2	Difference in log fO_2
Ni-MnO	1200	0.0001	48	-8.41	70.83	29.16	99.99	0.72	0.28	-8.35	0.06
n=15					*0.47*	*0.44*	*0.29*				
NiO-MnO	1200	0.0001	48	-8.41	69.27	30.50	99.77	0.71	0.29	-8.33	0.08
n=10					*0.40*	*0.45*	*0.38*				

Italicized numbers indicate one standard deviation and *n*= number of analyses.

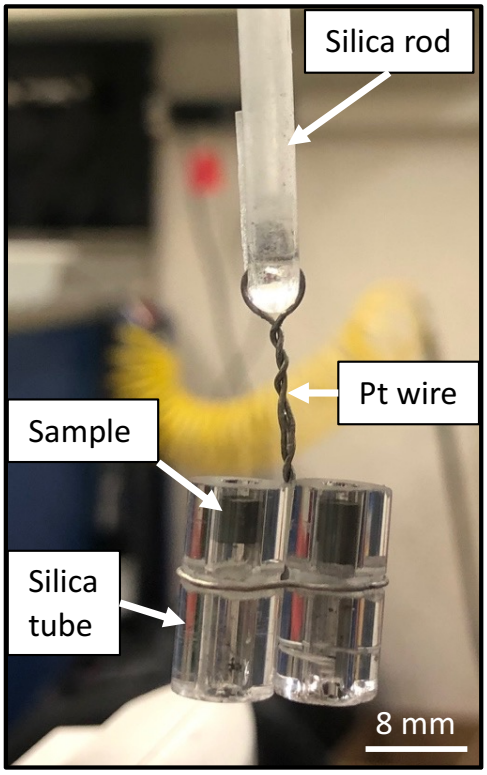

Figure A1. Configuration of the binary oxide redox sensor experiment. Mixtures of Ni-MnO and NiO-MnO, pressed in thick-walled silica tubes (ID = 3 mm, OD = 8 mm), are suspended from the silica rod with Pt wire.

APPENDIX B:
Piston-Cylinder Calibrations

1.0 Thermal Mapping

1.1 Introduction

Thermal mapping experiments of both the 19.05 mm and 12.07 mm diameter solid pressure assembly used in piston-cylinder experiments were conducted to determine the length and position of the hotspot. A reaction between the MgO insulator and the Al_2O_3 thermocouple sheath within the assembly creates a thin spinel layer ($MgAl_2O_4$):

$$MgO_{(s)} + Al_2O_{3(s)} = MgAl_2O_{4(s)}. \quad \text{(B1.1)}$$

The width of this layer, at any position in the assembly, can be related to temperature using the following calibration by Watson *et al.* (2002):

$$\Delta X = [8.58 \times 10^{11} \exp(-48865/T - 2.08 \cdot P^{1/2}) \cdot t]^{1/2}, \quad \text{(B1.2)}$$

in which ΔX is the spinel thickness in μm, T is temperature in K, P is pressure in GPa and t is time in s. The thickness of this layer can be measured on an optical microscope with a maximum uncertainty of ± 2-3 μm, as estimated by Watson *et al*. (2002).

1.2 Method

Experiments were conducted using a piston-cylinder apparatus (Boyd and England 1960) in the Dalhousie Experimental Geochemistry Laboratory. Standard 12.70 mm and 19.05 mm diameter solid pressure assemblies were used, which consisted of MgO filler pieces, a graphite furnace sleeve, and either $BaCO_3$ cells for the 12.70 mm assembly or NaCl cells along with a Pyrex sleeve for the 19.05 mm assembly (Figure B1.1). An Al_2O_3 filler piece was inserted into the lower half of the assembly and an Al_2O_3 -sheathed Type C (WRe_5-WRe_{26}) thermocouple was inserted into the top, with a 1 mm MgO spacer

dividing the two, at the center of the graphite furnace (Figure B1.1). Experiments were cold pressurized to ~ 0.03 GPa above the desired pressure which was then maintained manually while ramping the temperature at 50°C/min. Pressure was periodically adjusted during the run such that values were controlled within ± 0.015 GPa. To terminate the experiment, the power to the furnace was cut. Run conditions are summarized in Table B1.1. Assemblies were sectioned and polished on the long axis, then the spinel layer was measured on an optical microscope.

1.3 Results

Longitudinal temperature profiles, constructed using Equation B1.2 and the measured spinel layer thicknesses, are shown in Figure B1.2 and Figure B1.3, for the 12.70 mm and 19.05 mm diameter assembly, respectively. Results show that the length of the hotspot extends ~ 2.5 mm below the thermocouple height in the 12.70 mm assembly and ~ 5 mm below in the 19.05 mm assembly.

2.0 Thermocouple EMF

2.1 Introduction

The piston-cylinder is equipped with a Eurotherm controller that converts EMF generated by the Type C (WRe_5-WRe_{26}) thermocouple, used for experiments, to temperature. However, there are manufacturing variations between thermocouple wire spools, resulting in deviations from the ASTM E-230 standard values (ASTM international 2017; Table B2.1).

Herein, the accuracy of the display temperature on the Eurotherm controller was tested by directly measuring the thermocouple EMF. The display temperature was found to be accurate within ± 2.2°C over the temperature range investigated.

2.2 Method

Thermocouple EMF is generated when two dissimilar wires are junctioned and a temperature gradient is present along the wires. Therefore, EMF is proportional to the temperature difference between both ends of the thermocouple. However, by creating a reference junction at a known temperature, the absolute temperature of the thermocouple junction in the experiment can be determined. To do this, a reference junction was placed at 0°C, the same reference temperature used in the ASTM E-230 calibration, by submerging it in an ice bath. The EMF was measured by attaching the voltmeter to the 'hot' and 'cold' wire, as portrayed in Figure B2.1.

The thermocouple EMF was measured while ramping the temperature during a thermal mapping experiment (Sp_2; Section B1). This experiment was cold pressurized to ~ 1.15 GPa which was then maintained manually while increasing the temperature at a rate 50°C/min, dwelling every 100°C for 0.1 h, to record the EMF.

2.3 Results

Resultant EMF measurements are summarized in Table B2.2. The EMF was converted to temperature using the ASTM E-230 polynomial for a Type C thermocouple between 630.6°C and 2315°C with a reference junction at 0 °C. Results show that the Eurotherm temperature output is accurate within ± 2.2°C at 1.15 GPa, between 800 °C and 1400 °C.

3.0 Pressure Calibration

3.1 Introduction

In piston-cylinder experiments, sample pressure can deviate from gauge pressure due to the shear strength of the assembly and friction between the assembly and pressure vessel (Mirwald *et al.* 1975). To determine the pressure experienced by the sample, two methods were employed: (1) the solubility of water in albite after Baker (2004) and (2) the melting point of NaCl using the calibration of Bohlen (1984). From these results a pressure correction was applied to the nominal gauge pressure of +20% for experiments done at 0.5 GPa whereas no correction was required for experiments at 1 GPa.

Baker (2004) developed a pressure calibration method for piston-cylinder experiments using the relationship between pressure and the solubility of water in albite melt. With solubility data from Behrens *et al*. (2001), Baker (2004) calculated pressure with the following function:

$$P = -67.061 + 28.777H_2O - 2.2576H_2O^2 + 0.42747H_2O^3 - 0.019803H_2O^4, \quad \text{(B3.1)}$$

in which P is pressure in MPa and H_2O is the concentration of water dissolved in albite melt in wt%. Baker (2004) tested this method against the melting point of NaCl (described below) by conducting piston-cylinder experiments between 800-1200ºC and at 0.4-0.5 GPa. Baker (2004) found the resultant pressure to be accurate within ± 25 MPa, the solubility to be insensitive to temperature, and that relatively short run durations are adequate (<1 h). This method was used to determine the pressure correction for the 19.05 mm diameter solid pressure assemblies used in experiments done at 0.5 GPa.

The NaCl pressure calibration requires at least two experiments to bracket the melting point of NaCl. This calibration is suitable over a range of pressure but is limited to the solidus temperature of NaCl. The melting point of NaCl, determined in gas pressure

vessel experiments by Bohlen (1984), is portrayed as a function of pressure in Figure B3.1. This method was used to determine the pressure correction for experiments done at 1 GPa for both the 12.70 mm and 19.05 mm diameter solid pressure assemblies.

3.2 Method

3.2.1 Solubility of Water in Albite Melt

Synthetic albite was prepared by mixing reagent grade oxides which were ground twice under ethanol in an agate mortar. The starting material was placed in a Pt crucible and calcined in air, at 600°C, in a box furnace for 12 h. It was then ground under ethanol again and fused into a glass by melting in a Pt crucible for 30 min in air, in a box furnace, at 1500°C, then rapidly quenching in water. The albite glass was ground under ethanol into a fine powder and fused for a second time, to ensure homogeneity. The composition of the resultant glass is summarized in Table B3.1.

Experiments were conducted using a piston-cylinder apparatus (Boyd and England 1960) in the Dalhousie Experimental Geochemistry Laboratory. A 3 mm diameter gold capsule was loaded with albite powder and 24 wt% H_2O (well above H_2O saturation of ~11 %; Behrens *et al*. 2001; Baker 2004) and welded shut. The welded capsule was weighed and then stored in a 110°C drying oven overnight. The capsule had the same weight, before and after drying, indicating a successful weld. The capsule was then packed into a standard 19.05 mm solid pressure assembly, identical to those used in experiments, described in Section 2.1.3, as was the method of increasing pressure and temperature during the experiment. The nominal pressure was 0.515 GPa, controlled within ± 0.015 GPa. To terminate the experiment, the power to the furnace was cut. Run conditions are summarized in Table B3.1.

The run-product was mounted in a 25 mm diameter epoxy puck and polished and carbon coated for EPMA analysis in the Robert M. MacKay Electron Microprobe Laboratory at Dalhousie University. The albite glass was analyzed using a 15 kV accelerating voltage, a 5.5 nA beam current and a 20 μm beam size. Count times were 10 s for Na and 20 s for Al and Si. An albite standard was used for Na, Al and Si. The water concentration dissolved in the run-product was determined using the difference from 100 technique (Baker 2004). This method assumes that the difference between the total sum of EPMA measurements for the water-saturated albitic glass and 100% is equal to the concentration of the water in the glass.

3.2.1 Melting point of NaCl

Reagent grade NaCl was ground under ethanol into a fine powder and dried overnight at 200ºC in a box furnace. NaCl powder with a 0.5 – 1mm diameter Au bead were then tightly packed into 3 mm diameter Pt capsules with the bead positioned at the top of the capsule. Capsules were stored overnight at 110ºC in a drying oven and welded shut the following day. Standard 19.05 mm and 12.70 mm diameter solid pressure assemblies were identical to those used for experiments described in Section 2.1.3.

All experiments were cold pressurized to ~ 0.03 GPa above the desired pressure which was then maintained manually while ramping the temperature at 50°C/min to 20°C below the desired run temperature. The pressure was then allowed to relax to the desired run value. Pressure was controlled manually while ramping 1°C/min to the final run temperature. Upon reaching this temperature, pressure was controlled manually for 25

min before quenching by cutting the furnace power. Run conditions are summarized in Table B3.2. Samples were opened by polishing on dry SiC grit paper.

3.3 Results

3.3.1 Solubility of Water in Albite Melt

Results are summarized in Table B3.1. The run-product consisted of vesicular albitic glass indicating water saturation. The difference from 100 technique yields 9.8 wt% H_2O dissolved in the albite glass, which equates to 0.413 GPa using Equation B3.1. This is ~0.1 GPa lower than the nominal experimental pressure and therefore, a +20% pressure correction was applied to experiments done at 0.5 GPa.

3.3.2 Melting point of NaCl

Results are summarized in Table B3.1 and portrayed in Figure B3.2. In supersolidus experiments, the Au bead remains at the top of the capsule, which occurred at 1020°C in both the 19.05 mm and 12.70 mm diameter assemblies. In subsolidus experiments, melted NaCl appears white (Figure B3.2) and the Au bead fell to the base of melted NaCl. The melted zone is equivalent to the length of the hotspot determined in Section B1. This occurs at 1030°C in both the 19.05 mm and 12.70 mm diameter assemblies. Results bracket the melting point of NaCl at 1025°C, consistent with the predicted value at run conditions established from experimental data by Bohlen (1984) (Figure B3.1). Therefore, nominal pressure around 1 GPa represents the true pressure experienced by the sample and no pressure correction is required for either assembly type.

4.0 References

ASTM International. 2017. E230/E230M Standard Specification for Temperature-Electromotive Force (emf) Tables for Standardized Thermocouples. ASTM Standards. **14.03**:1-168.

Baker, D.R. 2004. Piston-cylinder calibration at 400 to 500 MPa: A comparison of using water solubility in albite melt and NaCl melting. American Mineralogist, **89**: 1553–1556.

Behrens, H., Meyer, M., Holtz, F., Benne, D., and Nowak, M. 2001. The effect of alkali ionic radius, temperature, and pressure on the solubility of water in MAlSi3O8 melts (M=Li, Na, K, Rb). Chemical Geology, **174**: 275–289.

Bohlen, S. 1984. Equilibria for precise pressure calibration and a frictionless furnace assembly for the piston-cylinder apparatus. Neues Jahrbuch für Mineralogie Monatshefte, **9**: 404–412.

Luth, R.W. 1993. Measurement and control of intensive parameters in Experiments at High Pressure in Solid-media Apparatus. Mineralogical Association of Canada, short course handbook on Experiments at High Pressure and Applications to the Earth's Mantle, 15-31.

Mirwald, P.W., Getting, I.C., Kennedy, G.C., and Angeles, L. 1975. Low-Friction Cell for Piston-Cylinder High-Pressure Apparatus. Journal of Geophysical Research, **80**: 1519–1525.

Watson, E., Wark, D., Price, J., and Van Orman, J. 2002. Mapping the thermal structure of solid-media pressure assemblies. Contributions to Mineralogy and Petrology, **142**: 640–652.

Table B1.1. Run conditions for thermal mapping experiments.

Sample	Assembly Diameter (mm)	T (°C)	P(GPa)	Duration (h)
Sp_2	19.05	1400	1.03	3
Sp_3	12.70	1500	1.03	4

Table B2.1. Summary of results from thermocouple EMF measurements including the Type C thermocouple ASTM E-230 standard EMF values and the calibration that accompanies Type C thermocouple spool used in piston-cylinder experiments. The Δ represents the difference between the measured EMF and the Eurotherm output temperature.

T (°C)	E-230 EMF (mV)	Spool Calibration EMF (mV)	Measured EMF (mV)	Δ (°C)
800	14.494	14.506	14.472	-1.7
900	16.398	16.394	16.385	-0.5
1000	18.26	18.232	18.254	1.1
1100	20.071	20.031	20.07	2.2
1200	21.825	21.782	21.817	2.0
1300	23.52	23.482	23.514	1.9
1400	25.155	25.132	25.150	1.2

Table B3.1. Summary of run conditions, run-product composition, and resultant pressure correction for water in albite experiment.

Sample	Assembly Diameter (mm)	Nominal T (°C)	Nominal P (GPa)	t (h)	Na_2O	Al_2O_3	SiO_2	Total	Calculated P (GPa)	Resultant Pressure Correction (%)
Alb_SM	-	-	-	-	12.46	19.79	68.17	100.43	-	
					0.22	*0.28*	*0.56*	*0.53*		
Alb_4	19.05	1000	0.515	2	10.81	17.64	61.76	90.20	0.413	20
			0.015		*0.26*	*0.16*	*0.30*	*0.42*	*0.022*	

Table B3.2. Summary of run conditions and resultant pressure correction determined by the melting point of NaCl.

Sample	Assembly Diameter (mm)	Nominal T (°C)	Nominal P(GPa)	t (h)	Melted	Resultant Pressure Correction (%)
Pcal-S3	19.05	1020	1.101	0.42	×	0
Pcal-S10	19.05	1030	1.101	0.42	✓	
Pcal-S8	12.7	1020	1.101	0.42	×	0
Pcal-S9	12.7	1030	1.101	0.42	✓	

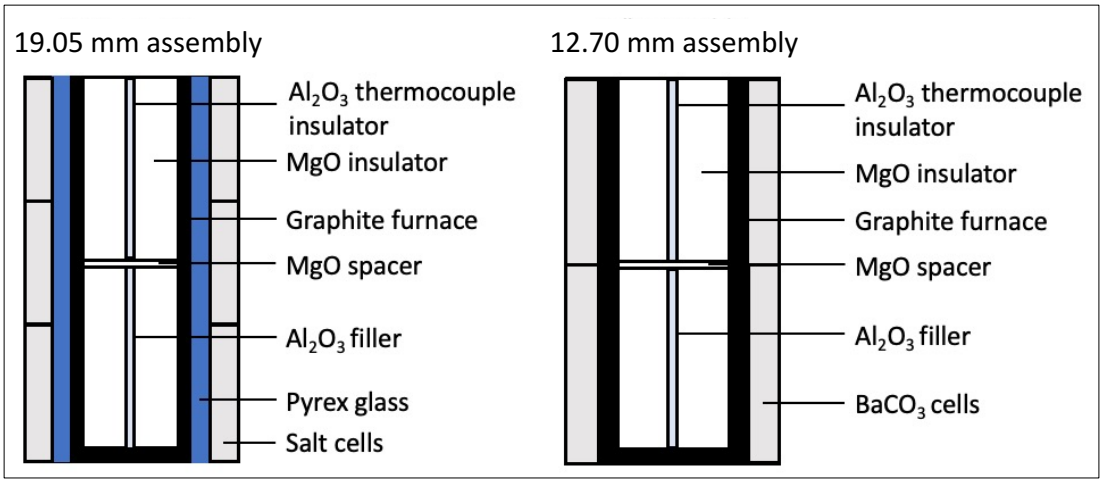

Figure B1.1. Schematic of 19.05 mm and 12.70 mm diameter solid pressure assemblies used in thermal mapping experiments. Not to scale.

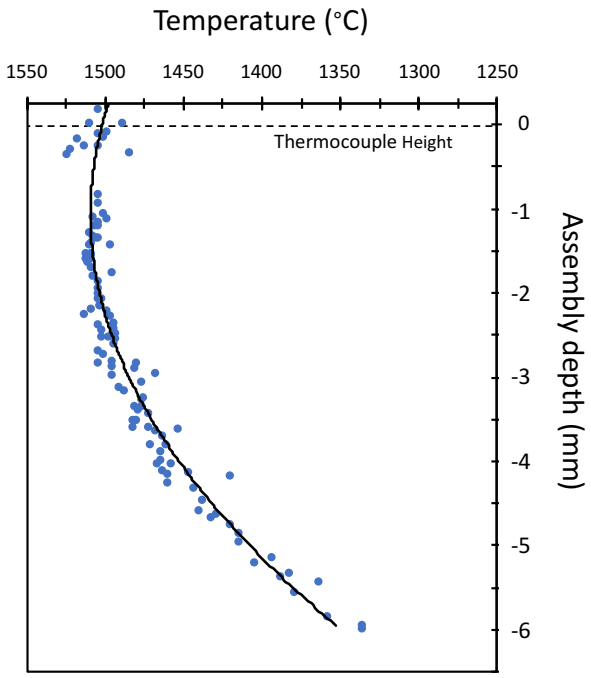

Figure B1.2. Longitudinal temperature profile for the 12.70 mm solid pressure assembly.

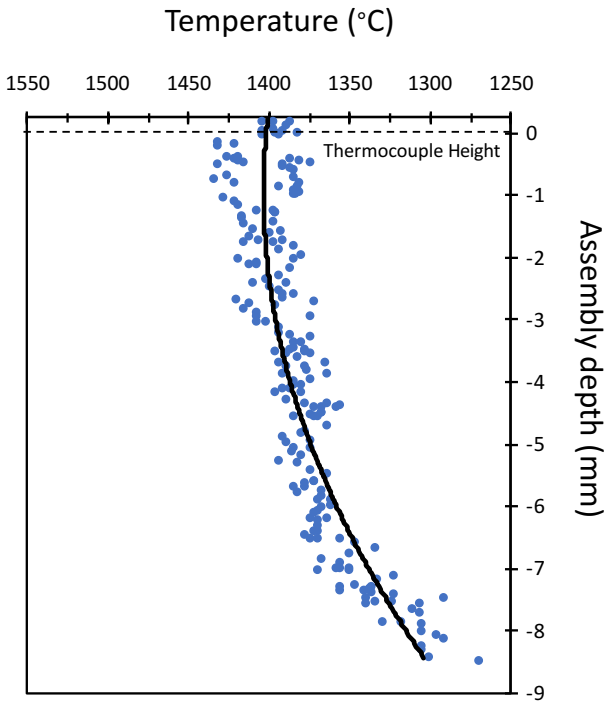

Figure B1.2. Longitudinal temperature profile for the 19.05 mm solid pressure assembly.

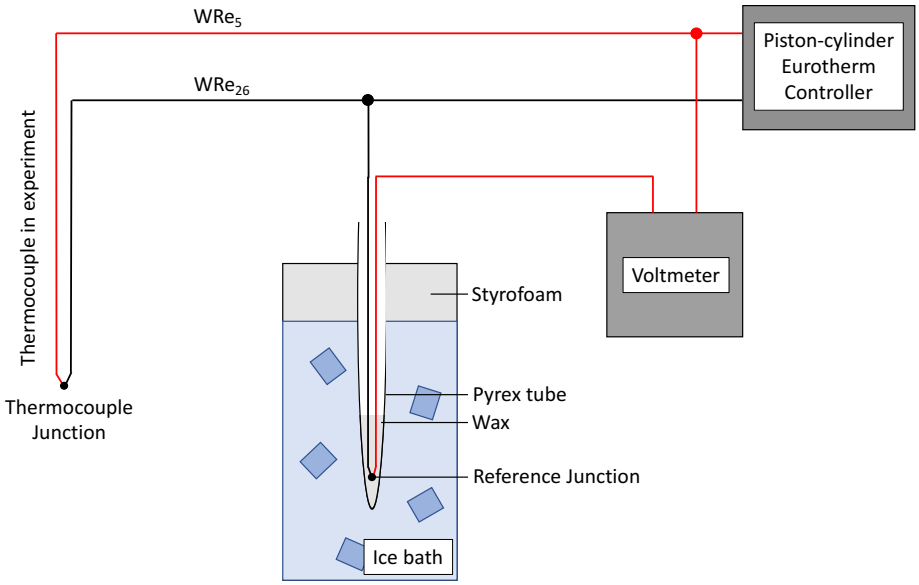

Figure B2.1. Schematic of the experimental configuration designed to test the accuracy of the Eurotherm temperature output. Not to scale.

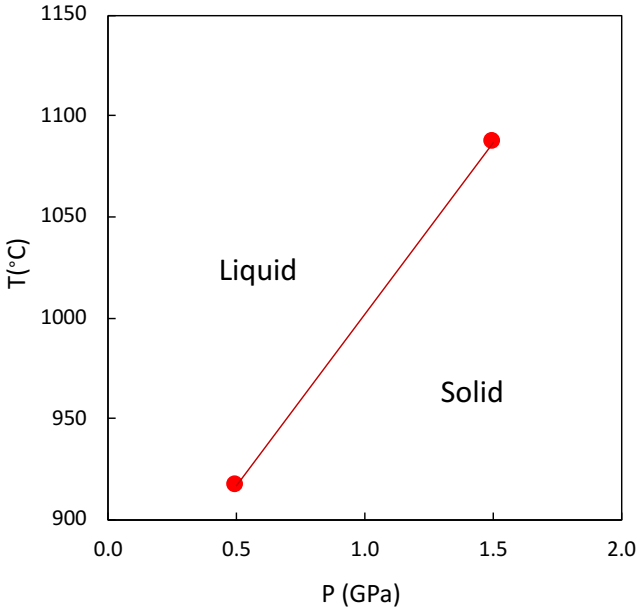

Figure B3.1. Melting point of NaCl as a function of pressure from gas pressure vessel experiments by Bohlen (1984). The linear regression is defined as T(°C) = 170•P(GPa) + 832.5 (r^2=1).

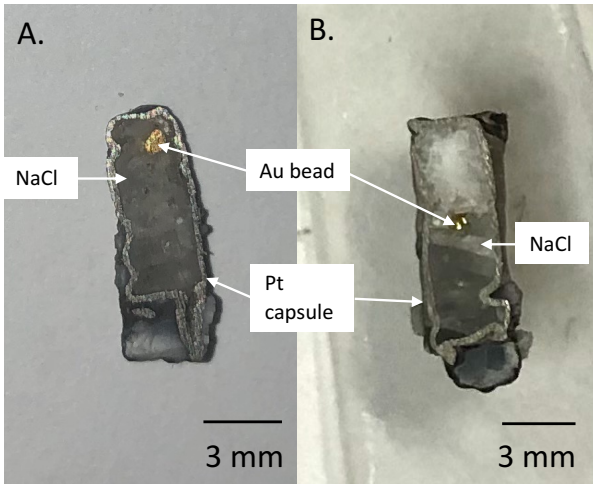

Figure B3.2. Example of NaCl melting point experiment results. A) No melting observed with gold bead remaining at the top of the capsule at 1020°C. B) Melting observed in which the gold bead fell to the middle of the capsule at 1030°C. The white NaCl reflects the melted region.

APPENDIX C:
Test of Thermodynamic Models for the Fe-FeO Equilibrium

1.0 Introduction

Iron-Ir capsules were used to buffer fO_2 for CCCS experiments conducted in the piston-cylinder apparatus. This noble metal alloy is ideal for run conditions of this study because Fe-Ir is the only stable Ir alloy from 650°C to 1400°C (Woodland and O'Neill 1997) and the composition of the alloy is dependent on fO_2. The fO_2 defined by the Fe-Ir equilibrium can be calculated using activity-compositional relations, however, there are different thermodynamic models available to do this.

Herein, different thermodynamic models were tested by equilibrating Fe-bearing melts with Ir wires at a fixed fO_2 in a gas mixing furnace. Resultant fO_2 values calculated from the Fe-Ir alloy were compared to imposed fO_2 during the experiment, measured by the Y-doped zirconia sensor. The best combination was found to be the activity coefficient for Fe metal (γFe) determined by Borisov and Palme (2000) and the activity coefficient for FeO in the silicate melt (γFeO) determined by Holzheid *et al*. (1997), which reproduces the imposed fO_2 within 0.14 ± 0.08 log units. As a result, this combination was used to calculate Fe-Ir capsule compositions for piston-cylinder experiments.

2.0 Thermodynamic Basis

The Fe-Ir redox is defined by the reaction:

$$Fe^{metal} + \frac{1}{2}O_2 = FeO^{sil}\,, \qquad \text{(C1)}$$

in which the Fe^{metal} is the Fe in the Fe-Ir alloy and FeO^{sil} is the FeO content in the silicate glass. The equilibrium constant (K_{eq}) of this reaction is expressed as:

$$K_{eq} = \frac{a_{FeO}}{a_{Fe}\, {fO_2}^{1/2}}, \tag{C2}$$

in which a_{FeO} is the activity of the FeO in the silicate glass and a_{Fe} is the activity of Fe in the Fe-Ir alloy. The change in standard state Gibbs free energy at 1 bar (0.1 MPa) and T, $\Delta G^{\circ}{}_{1,T}$ in J/mol, is:

$$\Delta G^{\circ}{}_{1,T} = -RT \ln K_{eq}, \tag{C3}$$

in which R is the gas constant in J/mol·K and T is the temperature in K. And, by substitution, $\log fO_2$ can be expressed as:

$$\log fO_2 = \frac{2}{\ln 10}\left[\frac{\Delta G^{\circ}{}_{1,T}}{\mathrm{RT}} + \ln(a_{FeO}) - \ln(a_{Fe})\right]. \tag{C4}$$

The $\Delta G^{\circ}{}_{1,T}$ for the Fe-FeO system can be calculated at a given temperature (T) using the equation compiled by Holzheid *et al.* (1997):

$$\Delta G^{\circ}{}_{1,T}(FeO_l) = -244118 + 115.559 \cdot T - 8.474 \cdot T \cdot \ln T\,. \tag{C5}$$

The activity of FeO in the silicate glass and Fe in the Fe-Ir alloy can be calculated using:

$$a_i = \gamma_i X_i\,, \tag{C6}$$

in which a is the activity of component *i,* FeO or Fe*,* γ is the activity coefficient of component *i* and *X* is the mole fraction of component *i*.

Two different models were tested for γ_{FeO}. One calculated using the polynomial expression derived by O'Neill and Eggins (2002):

$$\ln \gamma_{FeO} = \sum_{j=l}^{4} \sum_{k=l}^{j} a_{jk} X_j X_k\,, \tag{C7}$$

in which X is the mole fraction and a is the coefficient of component j and k, defined in Table C1.

The other γ_{FeO} is a constant value of 1.7 ± 0.22 determined by Holzheid *et al.* (1997) for silicate glass between 1300-1600°C, which is independent of FeO content up to 20 wt % MgO.

Two different models were tested for γ_{Fe}, in the Fe-Ir alloy. One calculated with the expression compiled by Borisov and Palme (2000) which uses interaction parameters derived at 1200°C:

$$RT \ln \gamma_{Fe} = {X_{Ir}}^2 \left[-45581 + 2X_{Fe}(-65590 + 45581)\right], \quad \text{(C8)}$$

and the other complied by Woodland and O'Neill (1997) for temperatures between 650°C and 1400°C:

$$RT \ln \gamma_{Fe} = {X_{Ir}}^2 \left[-57305 - 5491\ (3X_{Fe} - X_{Ir})\right], \quad \text{(C9)}$$

in which X_{Fe} is the mole fraction of Fe in the alloy and X_{Ir} is the mole fraction of Ir in the alloy.

3.0 Methods

Starting material ranged from basaltic to komatiitic in composition with varying FeO contents. Experiments were done in a 0.1 MPa vertical tube gas mixing furnace in the Dalhousie Experimental Geochemistry Laboratory. Oxygen fugacity was fixed close to the FMQ buffer and regulated by mixing proportions of CO_2 and CO gas. Before and after the experiment, fO_2 was measured using a Y-doped zirconia sensor and a Type S (Pt-$PtRh_{10}$) thermocouple was used to measure temperature inside the furnace.

For samples Lat_1, BCR 1, BCR 2, and B1_1, starting material and two pure Ir wires were densely packed into an olivine crucible and placed in a fused silica sample holder. For samples JB 1 b, JB 5 a, and JB 5 b, starting materials were mounted on pre-saturated

Fe-Ir wire loops. The sample holder or wires were were suspended on a hook fashioned at the end of a high purity silica rod. Experiments were executed by first withdrawing the silica rod to the top of the furnace tube, then sealing the furnace and commencing gas flow. The sample was then lowered into the predetermined hotspot and remained there for the experiment duration of 48-96 h. Experiments were terminated by opening the bottom of the furnace and lowering the silica rod through the bottom and into a beaker of water. Experimental run conditions are summarized in Table C2.

Run-products were mounted in 25 mm diameter epoxy pucks, then polished and carbon coated for EPMA analysis in the Robert M. MacKay Electron Microprobe Laboratory at Dalhousie University. Silicate glasses were analyzed using a 15 kV accelerating voltage, a 10 nA beam current and a 10 μm defocused beam. A count time of 20 s was used for all elements except for Cr, which was 40 s. Standards for the silicate glass analyses included the basalt USGS standard reference material, BHVO-1 (Si, Ca, Al, Fe, Mg, Na), rutile (Ti), chromite (Cr), sanidine (K), pyrolusite (Mn), and apatite (P).

After analyzing the glass, HF was used to dissolve the run-product and expose the Fe-Ir wire. Wires were mounted in epoxy pucks, then polished and carbon coated for EPMA analysis. The Fe-Ir alloy compositions were analyzed using a 20 kV accelerating voltage, a 50 nA beam current and a 1 μm beam size. Count times were 30 s for Fe and 10 s for Ir. Standards for the Fe-Ir alloy analyses were pure Fe metal and pure Ir metal.

4.0 Results

The major element compositions of the run-product glass and Fe-Ir alloy compositions are summarized in Table C2 and Table C3, respectively. The proportions of

FeO and Fe_2O_3 in the melt were calculated from FeO_T, as measured by the EPMA, using the calibration of Kress and Carmichael (1991) with the log fO_2 value recorded during the experiment by the Y-doped zirconia sensor.

As expected, at fixed fO_2, the equilibrium Fe content in the alloy is generally higher for a melt composition with a higher FeO content. Table C4 summarizes the log fO_2 values calculated from Equation C4 with the following combinations for γFeO and γFe:

(1) γFeO: O'Neill and Eggins (2002) & γFe: Borisov and Palme (2000),

(2) γFeO: O'Neill and Eggins (2002) & γFe: Woodland and O'Neill (1997),

(3) γFeO: Holzheid *et al.* (1997) & γFe: Borisov and Palme (2000),

(4) γFeO: Holzheid *et al.* (1997) & γFe: Woodland and O'Neill (1997),

using FeO in the run-product melt phase and the Fe-Ir alloy composition. Combination (1) and (2) yield values that are consistently more reduced with an average deviation of 0.54 log units from the value measured by the Y-doped zirconia sensor for combination (1) and 0.25 long units for combination (2). Results from combination (4) are consistently more oxidized, with an average deviation of 0.25 log units from the measured value. Combination (3) is very close to and brackets the imposed fO_2 value in which calculations result in an average deviation of 0.14 log units with a maximum deviation of 0.23 log units.

5.0 Conclusion

Iron-bearing basaltic to komatiitic melts were equilibrated with an Ir wire at a fixed fO_2 in a gas mixing furnace. Using different thermodynamic models for γFe in the alloy and γFeO silicate melt, the fO_2 recorded by the resultant Fe-Ir alloy wire was calculated. A combination of γFeO from Holzheid *et al*. (1997) and γFe from Borisov and Palme

(2000) was found to reproduce the imposed fO_2, as measured by the Y-doped zirconia sensor, the best. Therefore, these two thermodynamic models were used to calculate the Fe-Ir equilibrium for capsule compositions used in piston-cylinder experiments.

6.0 References

Borisov, A., and Palme, H. 2000. Solubilities of noble metals in Fe-containing silicate melts as derived from experiments in Fe-free systems. American Mineralogist, **85**: 1665–1673.

Holzheid, A., Palme, H, and Chakraborty, S. 1997. The activities of NiO, CoO, and FeO in silicate melts. Chemical Geology, **139**: 21-38.

Kress, V.C., and Carmichael, I.S.E. 1991. The compressibility of silicate liquids containing Fe2O3 and the effect of composition, temperature, oxygen fugacity and pressure on their redox states. Contributions to Mineralogy and Petrology, **108**: 82–92.

O'Neill, H.S.C., and Eggins, S.M. 2002. The effect of melt composition on trace element partitioning: An experimental investigation of the activity coefficients of FeO, NiO, CoO, MoO2 and MoO3 in silicate melts. Chemical Geology, **186**: 151–181.

Woodland, A.B., and O'Neill, H. 1997. Thermodynamic data for Fe-bearing phases obtained using noble metal alloys as redox sensors. Geochimica et Cosmochimica Acta, **61**: 4359–4366.

Table C1. Coefficients for the polynomial expression derived by O'Neill and Eggins (2002) at 1400°C.

	X_{Ca}	X_{Mg}	X_{Al}	X_{Si}
Fe ($\chi_v^2 = 17.7$)				
X_{Ca}	6.62	16.30	3.74	− 8.50
X_{Mg}		6.09	− 3.21	− 7.34
X_{Al}			− 2.61	6.08
X_{Si}				1.16

Table C2. Summary of experimental run conditions and major element chemistry in wt % of run-product silicate glass with one standard deviation in italics.

Sample	T (°C)	P (GPa)	log fO_2	t (h)	SiO_2	TiO_2	Al_2O_3	CaO	MgO	FeO_T	FeO^1	$Fe_2O_3^1$	MnO	Na_2O	K_2O	P_2O_5	Cr_2O_3	Total
JB_8a	1400	0.0001	-6.34	48	43.08	0.51	10.21	10.05	17.28	17.30	15.09	2.45	0.20	0.13	0.17	0.02	0.23	99.43
					0.53	*0.03*	*0.11*	*0.11*	*0.09*	*0.50*			*0.02*	*0.02*	*0.02*	*0.02*	*0.00*	
JB_8c	1400	0.0001	-6.34	48	45.92	0.58	10.80	10.55	18.30	12.65	10.95	1.89	0.21	0.19	0.26	0.02	0.26	99.93
					0.50	*0.06*	*0.10*	*0.14*	*0.21*	*0.29*			*0.02*	*0.01*	*0.02*	*0.03*	*0.00*	
JB_11a	1397	0.0001	-6.35	48	51.10	0.43	10.32	7.46	18.98	10.23	8.89	1.49	0.16	0.85	0.45	0.01	0.30	100.44
					0.15	*0.03*	*0.08*	*0.09*	*0.11*	*0.15*			*0.03*	*0.03*	*0.02*	*0.04*	*0.00*	
Lat_1	1397	0.0001	-6.26	96	50.60	0.08	12.38	7.70	18.96	9.82	8.51	1.45	0.06	0.78	0.08	0.02	0.07	100.69
					0.23	*0.03*	*0.07*	*0.08*	*0.10*	*0.10*			*0.02*	*0.03*	*0.01*	*0.03*	*0.00*	
BCR 1	1397	0.0001	-6.26	96	51.54	1.62	9.89	5.32	17.29	11.06	9.54	1.69	0.19	1.85	1.14	0.17	0.00	100.24
					0.42	*0.05*	*0.12*	*0.08*	*0.08*	*0.11*			*0.02*	*0.04*	*0.03*	*0.04*	*0.00*	
B1_1	1398	0.0001	-6.18	96	53.31	0.26	10.23	5.96	17.82	9.99	8.57	1.58	0.18	1.76	0.78	0.00	0.15	100.60
					0.21	*0.03*	*0.05*	*0.07*	*0.07*	*0.08*			*0.02*	*0.03*	*0.02*	*0.00*	*0.00*	
BCR 2	1398	0.0001	-6.18	96	51.33	1.60	9.78	5.08	17.30	11.27	9.68	1.76	0.17	1.87	1.15	0.00	0.01	99.74
					0.21	*0.05*	*0.08*	*0.05*	*0.09*	*0.07*			*0.02*	*0.02*	*0.02*	*0.00*	*0.00*	

Footnotes: 1. Calculated from FeO_T using the calibration of Kress and Carmichael (1991) with the experimental fO_2 value recorded by the Y-doped zirconia sensor.

Table C3. Summary of major element chemistry (wt %) of Fe-Ir alloy wires with one standard deviation in italics.

Sample	T (°C)	P (GPa)	log fO_2	t (h)	Fe	Ir	Total
JB_8a	1400	0.0001	-6.34	48	2.47	97.47	99.94
					0.21	*0.39*	
JB_8c	1400	0.0001	-6.34	48	2.26	97.67	99.94
					0.23	*0.54*	
JB_11a	1397	0.0001	-6.35	48	1.41	98.46	99.87
					0.25	*0.84*	
Lat_1	1397	0.0001	-6.26	96	1.45	98.17	99.62
					0.32	*0.49*	
BCR 1	1397	0.0001	-6.26	96	1.26	97.18	98.43
					0.18	*0.67*	
B1_1	1398	0.0001	-6.18	96	1.63	97.94	99.57
					0.23	*0.62*	
BCR 2	1398	0.0001	-6.18	96	1.80	97.23	99.03
					0.08	*0.28*	

Table C4. Calculated log fO_2 from Fe-Ir wires using four different calibrations. Delta represents the difference between calculated log fO_2 and the log fO_2 recorded by the Y-doped zirconia sensor. The calibration with the best results is bolded.

					1		2		3		4	
					γFeO: O'Neill and Eggins (2002)		γFeO: O'Neill and Eggins (2002)		**γFeO: Holzheid et al. (1997)**		γFeO: Holzheid et al. (1997)	
				Sensor	& γFe: Borisov and Palme (2000)		& γFe: Woodland and O'Neill (1997)		**& γFe: Borisov and Palme (2000)**		& γFe: Woodland and O'Neill (1997)	
Sample	T (°C)	P (GPa)	t (h)	log fO_2	calculated log fO_2	Δ	calculated log fO_2	Δ	calculated log fO_2	Δ	calculated log fO_2	Δ
JB_8a	1400	0.0001	48	-6.34	-6.72	-0.37	-6.46	-0.12	-6.31	0.03	-6.06	0.29
JB_8c	1400	0.0001	48	-6.34	-6.92	-0.58	-6.66	-0.31	-6.51	-0.17	-6.25	0.10
JB_11a	1397	0.0001	48	-6.35	-6.75	-0.40	-6.44	-0.09	-6.24	0.12	-5.93	0.42
Lat_1	1397	0.0001	96	-6.26	-6.79	-0.53	-6.48	-0.22	-6.30	-0.04	-6.00	0.26
BCR 1	1397	0.0001	96	-6.26	-6.62	-0.36	-6.31	-0.04	-6.06	0.20	-5.75	0.51
B1_1	1398	0.0001	96	-6.18	-6.97	-0.79	-6.67	-0.50	-6.41	-0.23	-6.12	0.06
BCR 2	1398	0.0001	96	-6.18	-6.96	-0.78	-6.67	-0.50	-6.40	-0.22	-6.11	0.06

APPENDIX D:
Compilation of External Standard Analyses

Table D1. Measured values for external standards compared to the GEOREM preferred values.

	EPMA (wt %)												LA-ICP-MS	
External Standard	K_2O	CaO	TiO_2	Cr_2O_3	Na_2O	MgO	Al_2O_3	FeO_T	MnO	SiO_2	P_2O_5	Total	External Standard	Cr (μg/g)
BHVO - GEOREM[1]	0.53	11.43	2.74	0.04	2.31	7.21	13.69	11.09	0.17	49.79	0.28	99.28	BHVO - GEOREM[1]	288
	0.00	*0.04*	*0.01*	*0.00*	*0.02*	*0.03*	*0.05*	*0.04*	*0.00*	*0.12*	*0.00*			*4*
BHVO - measured	0.52	11.38	2.69	0.04	2.25	7.23	13.81	10.99	0.17	50.04	0.25	99.36	BHVO - measured	292
n=113	*0.02*	*0.12*	*0.06*	*0.03*	*0.04*	*0.06*	*0.10*	*0.11*	*0.02*	*0.22*	*0.05*		*n=24*	*11*
BIR - GEOREM[1]	0.03	13.29	0.96	0.06	1.83	9.69	15.51	10.26	0.17	47.79	0.03	99.62	BIR - GEOREM[1]	393
	0.00	*0.06*	*0.06*	*0.00*	*0.02*	*0.05*	*0.07*	*0.05*	*0.00*	*0.16*	*0.00*			*4*
BIR - measured	0.04	13.26	0.92	0.05	1.81	9.70	15.73	10.18	0.17	48.05	0.03	99.91	BIR - measured	388
n=176	*0.01*	*0.12*	*0.05*	*0.03*	*0.04*	*0.08*	*0.16*	*0.11*	*0.03*	*0.24*	*0.04*		*n=30*	*16*

Italicized numbers indicate one standard deviation and n= number of analyses.
Footnotes: 1. Jochum *et al.* (2016).

References

Jochum, K.P., Weis, U., Schwager, B., Stoll, B., Wilson, S.A., Haug, G.H., Andreae, M.O., and Enzweiler, J. 2016. Reference Values Following ISO Guidelines for Frequently Requested Rock Reference Materials. Geostandards and Geoanalytical Research, **40**: 333–350.

APPENDIX E:
Backscatter Electron Images

a. **B1**: 1300°C & 0.1 MPa & ~FMQ

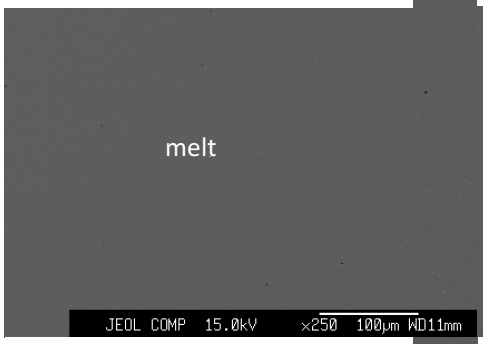

b. **Lat**: 1300°C & 0.1 MPa & ~FMQ

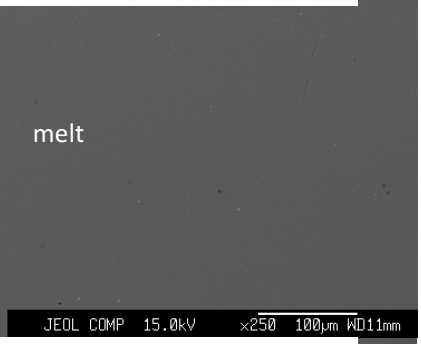

c. **B1**: 1280°C & 0.1 MPa & ~FMQ

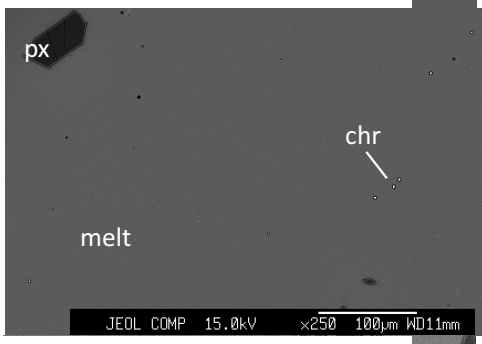

d. **Lat**: 1280°C & 0.1 MPa & ~FMQ

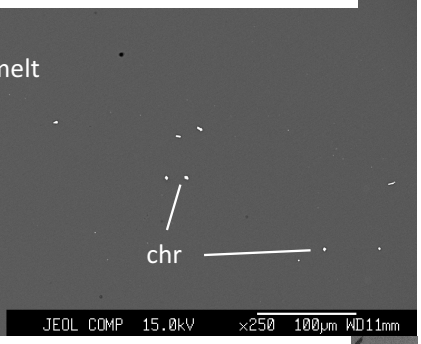

e. **B1**: 1230°C & 0.1 MPa & ~FMQ

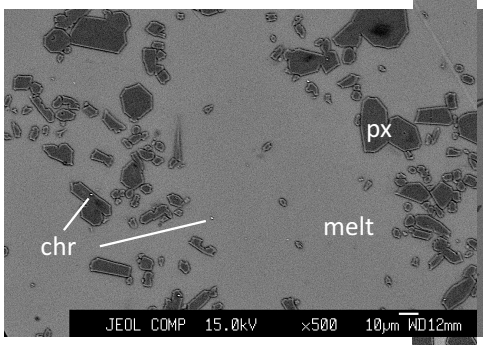

f. **Lat**: 1230°C & 0.1 MPa & ~FMQ

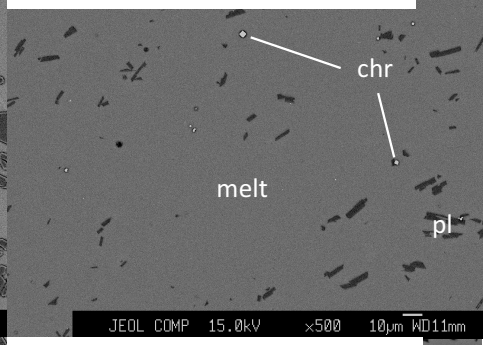

g. **B1**: 1230°C & 0.1 MPa & ~FMQ

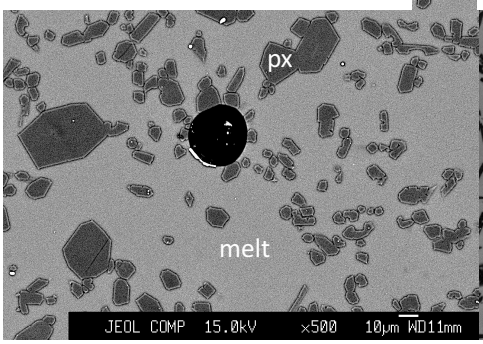

h. **Lat**: 1170°C & 0.1 MPa & ~FMQ

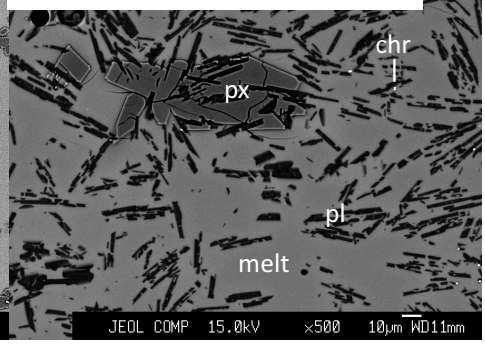

i. **B1$_d$**: 1230°C & 0.1 MPa & ~FMQ-0.40

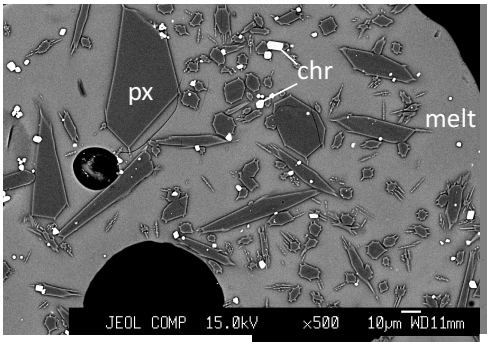

j. **B1**: 1400°C & 0.5 GPa & ~FMQ-2.15

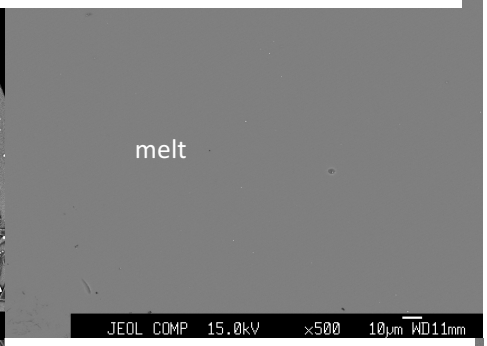

k. **B1**: 1370°C & 0.5 GPa & ~FMQ-2.10

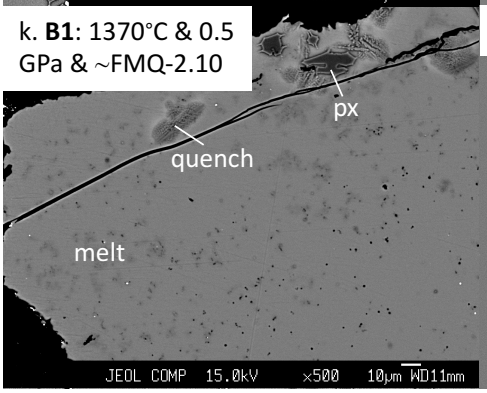

l. **Lat$_d$**: 1280°C & 0.5 GPa & ~FMQ-0.27

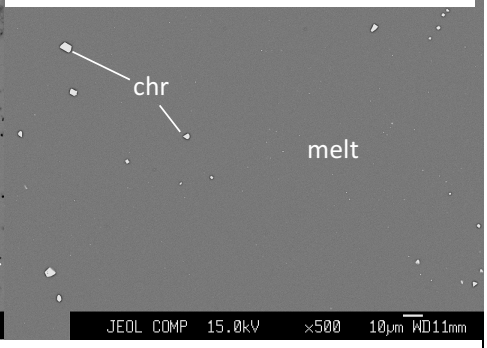

m. **B1$_d$**: 1280°C & 0.5 GPa & ~FMQ-0.27

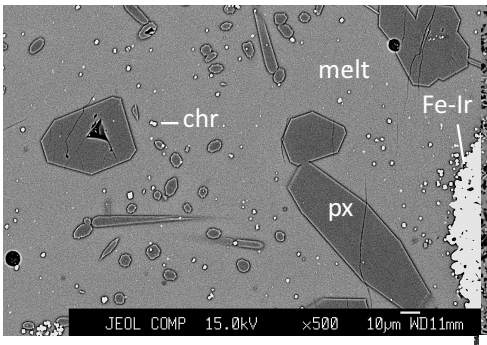

n. **Lat**: 1260°C & 0.5 GPa & ~FMQ-1.92

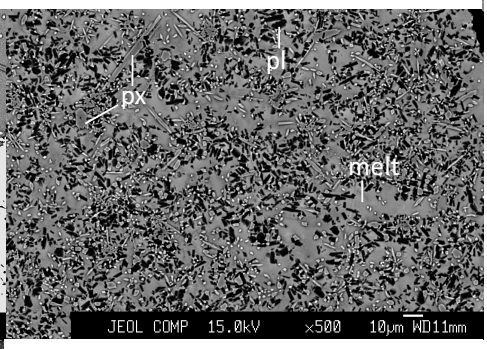

o. **B1$_d$**: 1230°C & 0.5 GPa & ~FMQ-0.27

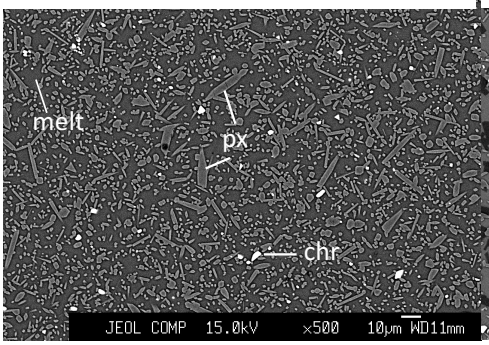

p. **Lat$_d$**: 1230°C & 0.5 GPa & ~FMQ-0.27

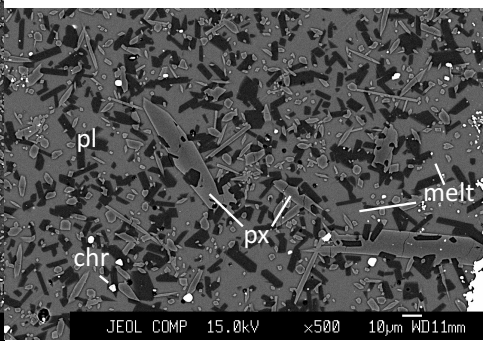

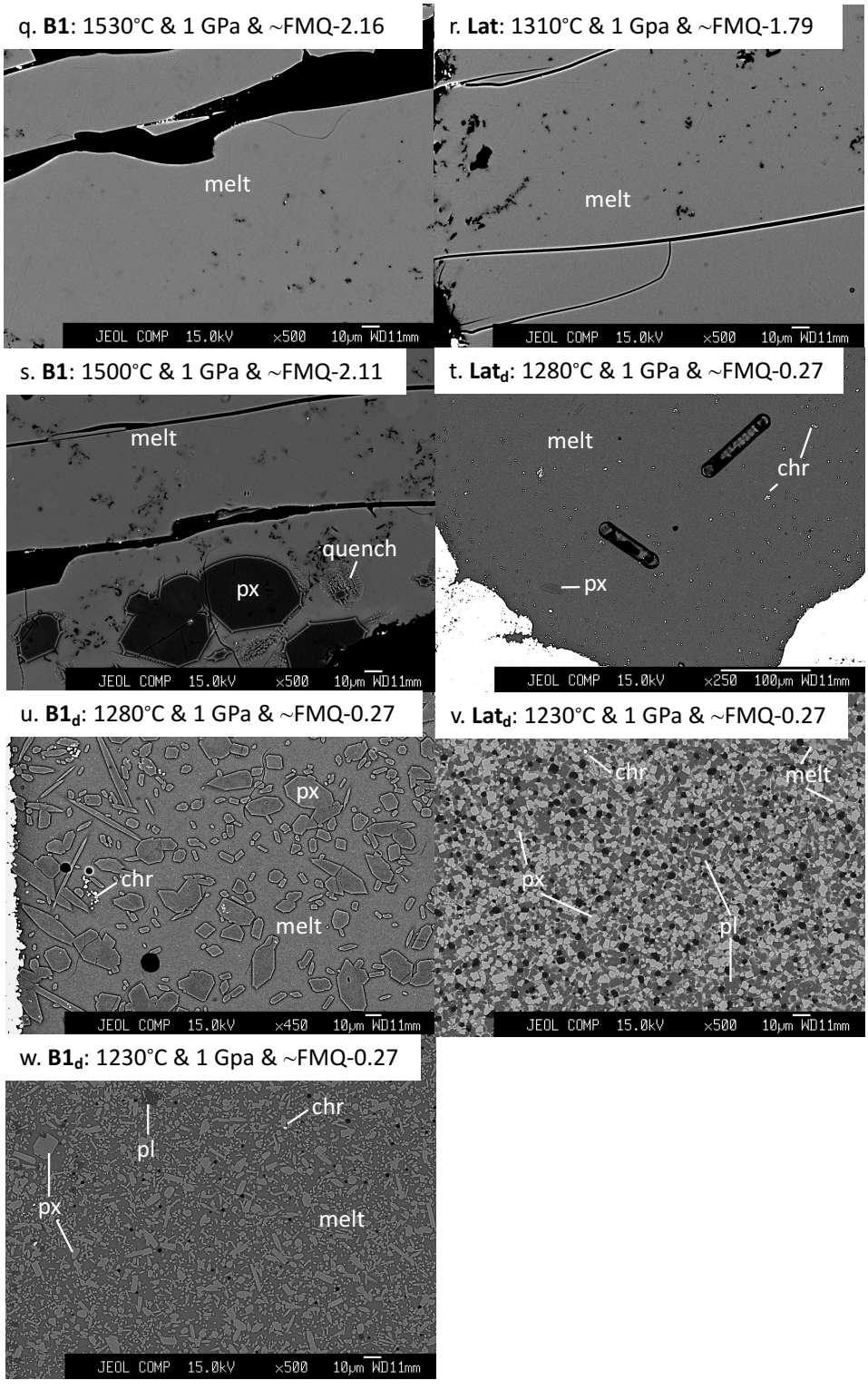

Figure E1. Backscattered electron images for representative experiments portraying phase equilibria, modal abundance, and textures. All images are at 500x magnification, except a., b., c., d., and s. which are at 250x and t. which is at 450x. Subscript $_d$ indicates chromite-doped starting materials. Abbreviations: px – pyroxene, pl – plagioclase, chr – chromite, Fe-Ir – Fe-Ir alloy capsule.

APPENDIX F:
AlphaMELTS Files

```
! Alphamelts Environmental Settings File

! for low-pressure use MELTS
ALPHAMELTS_VERSION        MELTS

! Use isobaric and batch crystallization
ALPHAMELTS_MODE          isobaric

! need to set tempearture path for isobaric mode, equivalent to:
! 'Final Temperature: 900' and 'Increment Temperature: 10.00'
! As initial Temperature: 1500 and Final Temperature: 900 we need a negative DELTAT
ALPHAMELTS_DELTAT    -10
ALPHAMELTS_MAXT      1500
ALPHAMELTS_MINT       900

! Use Celsius instead of Kelvin
ALPHAMELTS_CELSIUS_OUTPUT true

ALPHAMELTS_SAVE_ALL  true
ALPHAMELTS_SKIP_FAILURE true
```

Figure F1. Environmental settings file used for simulations in alphaMELTS 1.4.1. Temperature is in degrees Celsius.

```
Title: Melt composition X
Initial Composition: SiO2        X
Initial Composition: TiO2        X
Initial Composition: Al2O3       X
Initial Composition: Fe2O3       X
Initial Composition: Cr2O3       X
Initial Composition: FeO         X
Initial Composition: MgO         X
Initial Composition: CaO         X
Initial Composition: Na2O        X
Initial Composition: K2O         X
Initial Composition: H2O         X
Initial Temperature: 1500
Final Temperature: 900
Increment Temperature: 10
Initial Pressure: 1
Final Pressure: 1
Increment Pressure: 0
dp/dt: 0.00
log fo2 Path: FMQ
```

Figure F2. Example of MELTS file used for simulations in alphaMELTS 1.4.1 in which X represents the composition in wt %, temperature is in degrees Celsius and pressure is in bar. Pressure was varied in simulations from 1 bar to 10 000 bar.

APPENDIX G:
Experimental Plagioclase Compositions

Table G1. Summary of major element composition of run-product plagioclase.

Sample	T (°C)	P (GPa)	Δ FMQ	t (h)	K_2O	CaO	Na_2O	MgO	Al_2O_3	FeO_T	MnO	SiO_2	Total	An#[2]
Lat_1.9	1230	0.0001	0.04	48	0.12	9.721	1.593	5.766	17.33	8.95	0.005	55.4	99.03	0.76
n=10			*0.04*		0.005	0.093	0.07	0.086	0.118	0.151	0.009	0.353		
Lat_1.7	1200	0.0001	-0.03	48	0.05	14.80	1.73	1.29	28.76	2.09	0.00	51.40	100.12	0.82
n=20			*0.10*		*0.02*	*1.09*	*0.14*	*0.68*	*2.18*	*0.89*	*0.02*	*1.55*		
Lat_2.2[1]	1200	0.0001	-0.20	48	0.03	15.39	1.69	1.24	29.72	2.32	0.00	49.46	99.88	0.83
n=8			*0.01*		*0.02*	*1.31*	*0.13*	*0.89*	*2.80*	*1.04*	*0.01*	*1.87*		
Lat_1.8	1170	0.0001	0.00	29.5	0.09	13.87	2.20	1.42	27.07	2.35	0.00	52.51	99.50	0.77
n=17			*0.04*		*0.10*	*1.03*	*0.77*	*0.67*	*1.49*	*0.96*	*0.02*	*1.16*		
Lat_4.12	1260	0.51	-1.92	4	0.05	14.48	2.35	1.29	27.84	1.67	0.00	52.85	100.54	0.77
n=15		*0.02*			*0.01*	*0.60*	*0.12*	*0.66*	*1.52*	*0.79*	*0.02*	*0.85*		
Lat_3.5	1230	0.51	-0.24	12	0.06	13.98	2.63	0.44	28.95	0.85	0.00	52.62	99.53	0.74
n=18		*0.02*	*0.14*		*0.01*	*0.31*	*0.06*	*0.36*	*0.79*	*0.27*	*0.01*	*0.60*		
Lat_3.8	1230	1.02	0.04	12	0.10	13.40	3.05	0.59	27.70	1.02	0.00	54.75	100.60	0.70
n=15		*0.02*	*0.26*		*0.02*	*0.32*	*0.12*	*0.31*	*1.05*	*0.44*	*0.01*	*0.75*		
B1_3.8	1230	1.02	-0.22	12	0.44	11.16	3.98	0.93	25.24	0.91	0.02	57.76	100.45	0.59
n=8		*0.02*	*0.14*		*0.10*	*0.11*	*0.22*	*0.08*	*0.84*	*0.24*	*0.00*	*0.32*		

All oxides values in wt %, *n*= number of analyses and FeO_T indicates all Fe expressed as FeO. Italicized numbers indicate one standard deviation. Footnotes: 1. Melting experiments. 2. An # = Ca /(Ca+Na+K).